UNIVERSITÉ DU QUÉBEC EN ABITIBI-TÉMISCAMINGUE

ENGINEERING SCHOOL

JET PUMP COOLING FOR DEEP MINES

A THESIS SUBMITTED IN PARTIAL FULFILLMENT

OF THE REQUIREMENTS FOR

THE DEGREE OF MASTER OF ENGINEERING

BY

JAVIER RICO PAEZ

SEPTEMBER 2017

ACKNOWLEDGEMENTS

TABLE OF CONTENTS

LIST OF FIGURES

LIST OF TABLES

Résumé

Une des options possibles pour répondre au besoin de réfrigération dans les mines souterraines profondes est l'utilisation d'une turbine de détente ou d'un turbodétendeur, telle qu'elle est actuellement utilisée dans les systèmes classiques de réfrigération et de liquéfaction des gaz. Dans ces domaines, cette technologie est bien connue et exploite leur haute efficacité isentropique qui se traduit par une meilleure performance de refroidissement. L'électricité peut être générée comme un sous-produit de l'expansion de l'air comprimé dans ces systèmes. Cependant, ces machines nécessitent un entretien mécanique régulier, peuvent geler si elles ne sont pas correctement conçues, sont coûteuses et dans la sous-surface nécessitera de grandes fouilles. Au lieu de cela, ce travail considère le turbocompresseur remplacé par un simple, plus petit, pas de pièces mobiles et donc plus économique solution: l'éjecteur. Au lieu d'extraire le travail mécanique de l'arbre pendant le processus d'expansion et de refroidissement de l'air, un éjecteur peut entraîner un écoulement secondaire avec son jet d'air primaire à grande vitesse. Un projet d'éjecteur est proposé, comprenant une galerie souterraine de 4 mètres de diamètre et 32 mètres de long, avec une section initiale convergente, contenant un tuyau de 152,4 mm délivrant un jet d'air comprimé, envoyé à une gorge étroite et ensuite à un divergent, Section de récupération de pression. La conception est soutenue par des calculs thermodynamiques. À l'entrée, le débit d'air secondaire est supposé être à 39 ° C reflétant la température de l'air qui doit être refroidi. Le jet d'air comprend un débit massique de 22,36 kg / s à -71,32 ° C. Une élévation de pression statique de 1 kPa est maintenue de l'entrée à la sortie (à la sortie du diffuseur) où le débit massique de l'air est de 243,82 kg / s (y compris le débit d'air secondaire) à 29,02 ° C. Comme l'air comprenant le jet est plus sec que le flux d'air secondaire, à travers le processus de mélange, l'humidité de l'air est également réduite. En bref, le système se comporte comme un ventilateur auxiliaire qui refroidit et déshumidificateur.

Abstract

One option to address the need for refrigeration in deep underground mines is the use of an expansion turbine, or turbo-expander, as currently used in conventional refrigeration and gas liquefaction systems. In these other fields, this technology is well known and exploits their high isentropic efficiency which results in better cooling performance. Electricity can be generated as a by-product of expansion of compressed air in those systems. However, such machines require regular mechanical maintenance, can freeze up if not correctly designed, are expensive, and in the sub-surface would require large excavations. Instead, this work considers the turbo-expander replaced with a simple, smaller, no moving parts and hence more economical solution: the ejector. Instead of extracting mechanical shaft work during the air expansion and cooling process, an ejector can drive a secondary flow with its high speed primary air jet. A design for an ejector is put forward, comprising an underground gallery of 4 meters diameter and 32 meters long, with a convergent initial section, containing a 152,4 mm pipe delivering a compressed air jet, sent to a narrow throat and subsequently to a divergent, pressure recovering section. The design is supported by thermodynamic calculations. Inlet, secondary air flow is assumed to be at 39 °C reflecting the temperature of air that must be cooled. The air jet comprises a mass flow of 22.36 kg/s at -71.32 °C. A 1 kPa static pressure rise is maintained from the inlet to the outlet (at the diffuser exit) where the mass flow of the air is 243.82 kg/s (including the secondary air flow) at 29.02 °C. As the air comprising the jet is drier than the secondary air flow, through the mixing process, the humidity of the air is reduced too. In short, the system behaves like a booster fan that cools and dehumidifies.

CHAPTER 1

SFEE	Steady flow energy equation – (J/kg)
V_1	Velocity inlet, point 1 – (m/s)
V_2	Velocity outlet, point 2 – (m/s)
g	Gravitational constant – (m/s^2)
Z_1	Elevation, point 1 – (m)
Z_2	Elevation, point 2 – (m)
W_{12}	Mechanical work – (J/kg)
$\int VdP$	Flow work – (J/kg)
F_{12}	Frictional losses between 1 to 2 – (J/kg)
h_2	Enthalpy point 2 – (J/kg)
h_1	Enthalpy point 1 – (J/kg)
q_{12}	Heat transfer from 1 to 2 – (J/kg)
C_p	Heat capacity – (kJ/kg K)
T	Temperature – (K)
ΔZ	Increment of elevation – (m)
ΔT	Increment of Temperature – (K)
VTR	Virgin Rock Temperature – (°C)
WBGT	Wet Bulb Globe Temperature – (°C)
TLV	Threshold Limit Values – (°C)
HAC	Hydraulic Air Compressor
CFD	Computational Fluid Dynamics

CHAPTER 2

COP	Coefficient of performance – (%)
RBRC	Reverse Brayton refrigeration cycle
SFEE	Steady flow energy equation – (J/kg)
V_1	Velocity inlet, point 1 – (m/s)
V_2	Velocity outlet, point 2 – (m/s)
g	Gravitational constant – (m/s^2)
Z_1	Elevation, point 1 – (m)
Z_2	Elevation, point 2 – (m)
W_{12}	Mechanical work – (J)
$\int VdP$	Flow work – (J/kg)
F_{12}	Frictional losses between 1 to 2 – (J/kg)
h_2	Enthalpy point 2 – (J/kg)

h_1 Enthalpy point 1– (J/kg)

q_{12} Heat transfer from 1 to 2 – (J/kg)

$\eta_{isen\ compressor}$ Isentropic efficiency of the compressor

W_{12s} Isentropic compression work – (J)

h_{2s} Isentropic enthalpy point 2 – (J/kg)

$\eta_{isen\ turbine}$ Isentropic efficiency of the turbine

h_3 Enthalpy point 3 – (J/kg)

h_4 Enthalpy point 4 – (J/kg)

h_{4s} Isentropic enthalpy point 4 – (J/kg)

P Pressure of the gas – (Pa)

v Volume of the gas – (m^3/kg)

γ Isentropic coefficient

C Constant

R Gas constant – (J/mol K)

T Absolute temperature of the gas – (K)

T_2 Temperature point 2 – (K)

T_1 Temperature point 1 – (K)

P_2 Pressure point 2 – (Pa)

P_1 Pressure point 1 – (Pa)

r_p Compressor compression ratio

T_4 Temperature point 4 – (K)

T_3 Temperature point 3 – (K)

P_4 Pressure point 4 – (Pa)

P_3 Pressure point 3 – (Pa)

η_{cycle} Isentropic efficiency of the cycle – (%)

W_{34} Expansion or turbine work – (J)

W_{12} Compression or compressor work – (J)

q_{23} Gross heat input – (J/kg)

$\dot{Q}_{in}$ Rate of heat transfer – (J/s)

$\dot{W}_{cycle}$ Net work input – (J/s)

HAC   Hydraulic Air Compressor

MTTU   Modular thermal transfer unit

NHEA   Natural heat exchange area

Z Compressibility factor – (dimensionless)

P_R Reduced pressure – (dimensionless)

P_{cr} Critical pressure – (Pa)

T_R Reduced temperature – (dimensionless)

T_{cr} Critical temperature – (K)

μ_{JT} Joule-Thomson coefficient – (K/Pa)

$\left(\dfrac{\partial T}{\partial P}\right)_h$ Rate of change of temperature with respect to pressure a constant enthalpy.

CHAPTER 3

RTT	Reynolds Transport Theorem
$\frac{D}{Dt}$	Time rate of change
B	Extensive property (proportional to mass)
B	Amount of B per unit mass
ρ	Density – (kg/m^3)
V	Volume – (m^3)
$u_{rel}dA$	Volumetric flowrate through the surface – (m^3/s)
CS	Control surface
CV	Control volume
$\vec{n_1}$	Normal vector inlet
$\vec{n_2}$	Normal vector outlet
ρ_1	Density inlet – (kg/m^3)
V_1	Flow velocity inlet – (m/s)
A_1	Cross sectional area inlet – (m^2)
$\dot{m}_1$	Mass flow rate inlet – (kg/s)
ρ_2	Density outlet – (kg/m^3)
V_2	Flow velocity outlet – (m/s)
A_2	Cross sectional area outlet – (m^2)
$\dot{m}_2$	Mass flow rate outlet – (kg/s)
u_{XYZ}	Velocity of a little portion of the fluid in the system relative to an inertial reference framework XYZ
$\sum F_{on\ system}$	Total forces acting on the system – (N)
$F_{body\ on\ CV}$	Body force – (N)
$F_{surface\ on\ CV}$	Surface force – (N)
M_1	Linear momentum inlet – (kgm/s)
M_2	Linear momentum outlet – (kgm/s)
F_{P_1}	Pressure forces inlet – (N/m^2)
F_{P_2}	Pressure forces outlet – (N/m^2)
W	Weight – (N)
FP_W	Pressure forces on the wall – (N/m^2)
F_{Fw1}	Friction forces on the exterior wall – (N)
$E_{of\ system}$	Total energy of the system – (J)
$Q_{into\ system}$	Heat added to the system – (J)
$W_{on\ system}$	Work done on the system – (J)
e	Total energy (specific) – (J/kg)
u	Internal energy (specific) – (J/kg)
$\frac{1}{2}V^2$	Kinetic energy (specific) – (J/kg)

gz Potential energy (specific) – (J/kg)

$W_{on\,CV}$ Total work – (J)

$W_{pressure,on\,CV}$ Work pressure – (J)

$W_{shaft,on\,CV}$ Shaft work – (J)

$W_{other,on\,CV}$ Other work – (J)

η_p Isentropic efficiency of the primary flow

η_s Isentropic efficiency of the secondary flow

ϕ_p Losses of the primary flow

ϕ_m Losses of the secondary flow

CPM   Constant-pressure mixing

CAM   Constant-area mixing

η Isentropic efficiency – (%)

h_{inlet} Inlet enthalpy – (J/kg)

h_{outlet} Outlet enthalpy – (J/kg)

$h_{outlet,isentropic}$ Outlet enthalpy of the isentropic process – (J/kg)

η_m Efficiency of the motive nozzle

η_s Efficiency of the suction chamber

η_{mix} Efficiency of the mixing area

η_d Efficiency of the diffuser

η_e Efficiency of the eductor

η_C Efficiency of the compressor

η_T Efficiency of the turbine

$\dot{m}_s$ Mass flow rate of the secondary fluid or evaporator – (kg/s)

$\dot{m}_m$ Mass flow rate of the motive fluid or generator – (kg/s)

$h'_{s,isentropic}$ Isentropic suction nozzle enthalpy – (J/kg)

h_s Suction nozzle enthalpy – (J/kg)

h_m Motive nozzle enthalpy – (J/kg)

$h'_{m,isentropic}$ Isentropic motive nozzle enthalpy – (J/kg)

η_{TER} Efficiency of the Turbine-Compressor entrainment ratio

ER   Entrainment ratio in a real ejector

TER   Turbine-Compressor entrainment ratio

NXP   Motive nozzle exit position

Dm   Diameter of the mixing section – (m)

Dt   Diameter of the nozzle throat – (m)

Lm   Length of the mixing section – (m)

VBA   Visual basic for applications

u_{p-in} Internal energy primary inlet – (J/kg)

$\dot{m}_{p-in}$ Mass flow rate primary inlet – (kg/s)

$\frac{1}{2}V_{p-in}{}^2$ Kinetic energy primary inlet – (J/kg)

gz_p Potential energy primary – (J/kg)

$\dfrac{P_{p-in}}{\rho_{p-in}}$ Flow work primary inlet – (J/kg)

u_{p-out} Internal energy primary outlet – (J/kg)

$\dot{m}_{p-out}$ Mass flow rate primary outlet – (kg/s)

$\dfrac{1}{2}V_{p-out}{}^2$ Kinetic energy primary outlet – (J/kg)

$\dfrac{P_{p-out}}{\rho_{p-out}}$ Flow work primary outlet – (J/kg)

u_{s-in} Internal energy secondary inlet – (J/kg)

$\dot{m}_{s-in}$ Mass flow rate secondary inlet – (kg/s)

$\dfrac{1}{2}V_{s-in}{}^2$ Kinetic energy secondary inlet – (J/kg)

gz_s Potential energy secondary – (J/kg)

$\dfrac{P_{s-in}}{\rho_{s-in}}$ Flow work secondary inlet – (J/kg)

u_{s-out} Internal energy secondary outlet – (J/kg)

$\dot{m}_{s-out}$ Mass flow rate secondary outlet – (kg/s)

$\dfrac{1}{2}V_{s-out}{}^2$ Kinetic energy secondary outlet – (J/kg)

$\dfrac{P_{s-out}}{\rho_{s-out}}$ Flow work secondary outlet – (J/kg)

ρ_{p-in} Density primary inlet – (kg/m^3)

V_{p-in} Velocity flow primary inlet – (m/s)

A_{p-in} Cross sectional area primary inlet – (m^2)

ρ_{s-in} Density secondary inlet – (kg/m^3)

V_{s-in} Velocity flow secondary inlet – (m/s)

A_{s-in} Cross sectional area secondary inlet – (m^2)

ρ_{p-out} Density primary outlet – (kg/m^3)

V_{p-out} Velocity flow primary outlet – (m/s)

A_{p-out} Cross sectional area primary outlet – (m^2)

ρ_{s-out} Density secondary outlet – (kg/m^3)

V_{s-out} Velocity flow secondary outlet – (m/s)

A_{s-out} Cross sectional area secondary outlet – (m^2)

g Gravitational constant – (m/s^2)

P_{p-in} Pressure primary inlet – (Pa)

$A_{primary}$ Cross sectional area primary – (m^2)

P_{p-out} Pressure primary outlet – (Pa)

$Fr_{inletwall}$ Friction force inlet-wall

Fr_p Friction force primary – (N)

P_{s-in} Pressure secondary inlet – (Pa)

P_{s-out} Pressure secondary outlet – (Pa)

Fr_s Friction force secondary – (N)

q Rate of heat transfer – (J/s)

U Overall heat transfer coefficient – (J/m^{2}sK)

A Area available for heat transfer $-$ (m^2)

ΔT_m Variation in mean temperatures $-$ (K)

CHAPTER 4

V_1 Velocity inlet, point 1 $-$ (m/s)

V_2 Velocity outlet, point 2 $-$ (m/s)

g Gravitational constant $-$ (m/s^2)

Z_1 Elevation, point 1 $-$ (m)

Z_2 Elevation, point 2 $-$ (m)

W_{12} Mechanical work $-$ (J)

$\int V dP$ Flow work $-$ (J/kg)

F_{12} Frictional losses between 1 to 2 $-$ (J/kg)

h_2 Enthalpy point 2 $-$ (J/kg)

h_1 Enthalpy point 1 $-$ (J/kg)

q_{12} Heat transfer from 1 to 2 $-$ (J/kg)

P_c Critical pressure $-$ (Pa)

P_1 Nozzle inlet pressure $-$ (Pa)

γ Isentropic coefficient $-$ (dimensionless)

T_c Critical temperature $-$ (K)

T_1 Nozzle inlet temperature $-$ (K)

r_t Temperature ratio exit

T_2 Nozzle outlet temperature $-$ (K)

P_2 Nozzle outlet pressure $-$ (Pa)

C_D Coefficient of discharge $-$ (dimensionless)

$\dot{m}_{actual}$ Actual mass flow rate $-$ (kg/s)

$\dot{m}_{isentropic}$ Isentropic mass flow rate $-$ (kg/s)

V_Y Velocity in position Y $-$ (m/s)

h_1 Enthalpy position 1 $-$ (J/kg)

h_Y Enthalpy position Y $-$ (J/kg)

V_1 Velocity position 1 $-$ (m/s)

V_c Critical velocity at the throat $-$ (m/s)

h_c Critical enthalpy at the throat $-$ (J/kg)

A_c Critical velocity at the throat $-$ (m/s)

$\dot{m}_{isentropic}$ Isentropic mass flow rate $-$ (kg/s)

v_c Critical specific volume $-$ (m^3/ kg)

D_c Critical diameter $-$ (m)

η_{nozzle} Efficiency of the nozzle

C_p Heat capacity $-$ (kJ/kgK)

T_2 Temperature point 2 $-$ (K)

T_1 Temperature point 1 $-$ (K)

P_2	Pressure point 2 – (Pa)
P_1	Pressure point 1 – (Pa)
ρ	Density – (kg/m³)
A_e	Exit area of the nozzle – (m²)
A_t	Throat area of the nozzle – (m²)
P_b	Back pressure – (Pa)
P_c	Chamber pressure – (Pa)

CHAPTER 6

P_c	Critical pressure – (Pa)
P_1	Nozzle inlet pressure – (Pa)
γ	Isentropic coefficient – (dimensionless)
T_1	Nozzle inlet temperature – (K)
T_2	Nozzle outlet temperature – (K)
P_2	Nozzle outlet pressure – (Pa)
η_{nozzle}	Efficiency of the nozzle
h_1	Enthalpy inlet – (J/kg)
h_2	Enthalpy outlet – (J/kg)
h_{2s}	Isentropic enthalpy outlet – (J/kg)
P_{drop}	Fan drop pressure – (Pa)
Q	Volumetric flow rate – (m³/s)
Scfm	Standard cubic feet per minute – (ft³/min)

CHAPTER 1

GENERAL INTRODUCTION

1.1 Introduction

Mine ventilation is a critical element in underground mining. The air temperature changes from summer to winter or even in the same day. The perfect case scenario would be the mine planning responsible thinks first about this situation before defining production but in a mine there are another priorities. In order to supply fresh air to the place needed it is essential to plan ventilation taking into account design, safety, control and system optimization.

Some ventilation systems have been poorly design for 10 years reserves, despite the fact that a good design system keep workforce safety as well as contribute to the efficiency of the mine operation, due to the fact of quick payback. A ventilation deficient system is more expensive in the long term. For instance, raise bores and shafts are often designed constrained by production parameters instead of ventilation constraints. As the mine goes deeper and ages, the work load capacity and air velocity are reduced; the shock losses, heat load increase energy consumption and cost rise. HVAC costs for Kidd Mine are estimated to be 70 % of operating cost (Howes and Hortin, 2005).

Some ventilation systems initially supply enough air to the underground mine. During mine expansion production increases but the ventilation system may not be improved and the ventilation system becomes deficient requiring expensive retrofit options to be achieved. Once in production, capital to invest in mine ventilation tends

to be scarce since the mine's main goal is production. The increasing of fan pressure and quantity of air during the mine expansion affects ventilation costs. Fan electricity costs rise with the increase of total pressure of the fan. As the lengths of airways extend there is more resistance in the system therefore more fan pressure is needed. Fan electricity costs increase in proportion to the system resistance. In addition, leakage from ducting and through broken ground, as well as shock losses increases the total quantity of pressure required.

Due to the fact that the surface deposits are running out, the only solution is going deeper. Going deeper means getting hotter, because of the geothermal gradient, eventually they need to have active cooling, for instance, an ejector. The ejector was well known at the beginning of the twenty century as part of the steam jet-pump refrigeration system. Unfortunately due to the ejector low coefficient of performance was replaced mostly by vapour compression refrigeration systems using mechanical compressors, (Ablwaifa, 2006). However, these refrigeration systems represent a major addition to mine infrastructure which substantially elevate mining costs. As part of an industry wide drive to lower mining costs, there is always need for new thinking and the exploration of new concepts for mine cooling. In this work, a modern ejector system will be reconsidered as part of an unconventional refrigeration system, based on the reverse Brayton cycle that utilizes a Hydraulic Air Compressor (HAC). HACs are another example of a historically well-established technology which subsequently fell out, of use, but which also features as part of the mine refrigeration concept explored in this thesis because it has great potential to deliver compressed air much more cheaply to mines. Consequently, this too will be explained in detail in the thesis. Further advantages of the ejector refrigeration system concept of this work are that i) air is the refrigerant gas as well as the coolant gas, ii) heat exchange is direct, iii) an ejector is a small, no moving parts, no maintenance technology and iv) for the same rated cooling the ejector concept will be compact, requiring less underground space to be developed in comparison to the current incumbent vapor compression refrigeration systems.

1.2 Sources of heat in the sub-surface

In order to design a cooling system for underground mines, it is first necessary to develop some understanding of why the air becomes heated and its temperature becomes elevated. Important sources of heat are outlined in the following subsections.

1.2.1 Effect of auto-compression and geothermal gradient on ventilation air temperatures

In an underground mine the air descends through a so-called downcast shaft, increasing the temperature of dry air, as the potential energy is converted into pressure energy and adiabatic conditions are generally assumed to hold. Depending on the age of the shaft, and diurnal and seasonal temperature variations, adiabatic conditions may not apply so that heat transfer from the rock to the air can occur driven by the air temperature, the rock temperature, the air humidity and the wetness of the shaft. The rock temperature at a given depth depends upon the geothermal gradient.

The steady flow energy equation is frequently used to govern the downcast shaft process in (J/kg):

$$\frac{(V_1{}^2 - V_2{}^2)}{2} + g(Z_1 - Z_2) + W_{12} = \int VdP + F_{12} = h_2 - h_1 - q_{12} \tag{1}$$
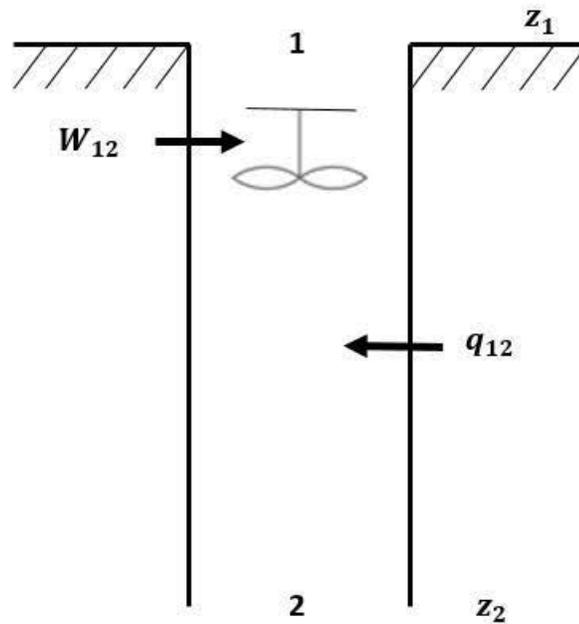
Figure 1: Downcast shaft

With constant cross-section of the shaft, and no input fan work, the top subscript 1 and the bottom subscript 2, of a downcast shaft (Figure 1), (1) becomes:

$$g(Z_1 - Z_2) = h_2 - h_1 - q_{12} \qquad \text{(J/kg of mass flow)} \qquad (2)$$

The enthalpy can be written as a function of temperature substituting $\Delta h = C_p \Delta T$

Assuming the air is an ideal gas. Then:

$$g(Z_1 - Z_2) = C_p(T_2 - T_1) - q_{12} \qquad (3)$$

$$g\Delta Z = C_p \Delta T - q_{12} \qquad (4)$$

$$g + \frac{q_{12}}{\Delta Z} = C_p \frac{\Delta T}{\Delta Z} \qquad (5)$$

If the assumed adiabatic conditions prevail and air with $C_p = 1005 \; kJ/kgK$ then (6) leads to an approximately 1 K /100 m increase in air temperature with a fall in elevation.

$$\frac{\Delta T}{\Delta Z}\bigg|_{AC} = \frac{g + \frac{q_{12}}{\Delta Z}}{C_p} \qquad (6)$$

If the rock temperature around the shaft is lower than the air temperature then q_{12} is negative (the air is cooled by the rock) and the air temperature lapse rate becomes < 1 K / 100 m. Water evaporating into air increases the enthalpy of the air, leading to the same trend. When the rock has a higher temperature than the air, heat enters the air from the rock and the air temperature lapse rate > 1 K / 100 m. What happens to the air temperature in the shaft thus depends on the temperature of the rock.

The geothermal gradient can vary between 3 K / 100 m to 4 K / 100 m in mining regions with relatively 'hot rocks' such as Cornwall, UK; to 1 K / 100 m in some mining districts of Canada and South Africa. (Millar et al., 2014)

The actual 'virgin rock temperature' (VTR) at any depth in a particular mining locale not only depends on the geothermal gradient, but also on the temperature of the rock at surface, which is climate determined. For South Africa, although its geothermal gradient is one of the lowest, the average surface temperature is relatively high and the gold mines now exploit ore at great depth, so the VRTs at these horizons are high. The VRT depends on the thermal conductivity and heat capacity of the rock, and the state of geothermal heat flux.

For a mine with a geothermal gradient of 1 K / 100 m, if the surface air temperature is lower than the surface VRT, as the air descends, the air will be continuously warmed by the surrounding rock (Figure 2).
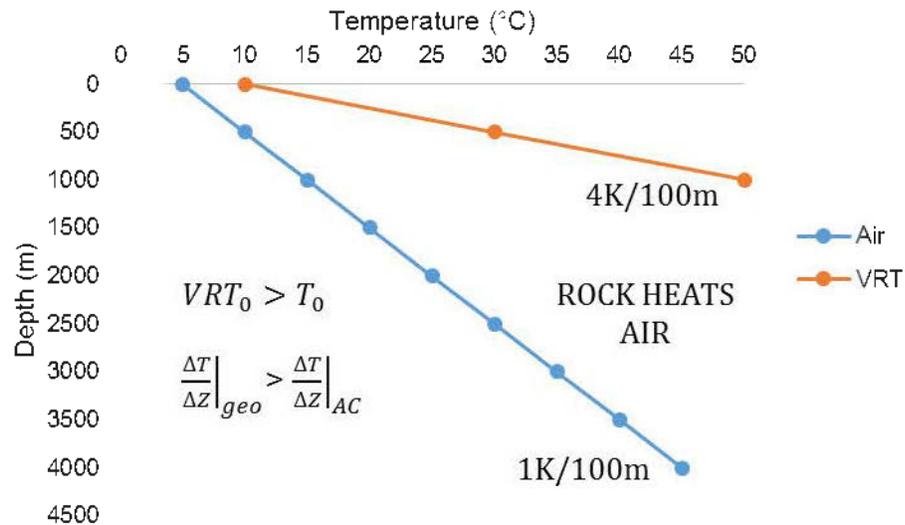
Figure 2: Cornwall winter daytime where surface air temperature is lower than the surface VRT

In Figure 3, the surface air temperature is lower than the surface VRT but the increase of air temperature due to the autocompression is higher than the geothermal flux, due to decrease in surface temperature during nighttime.
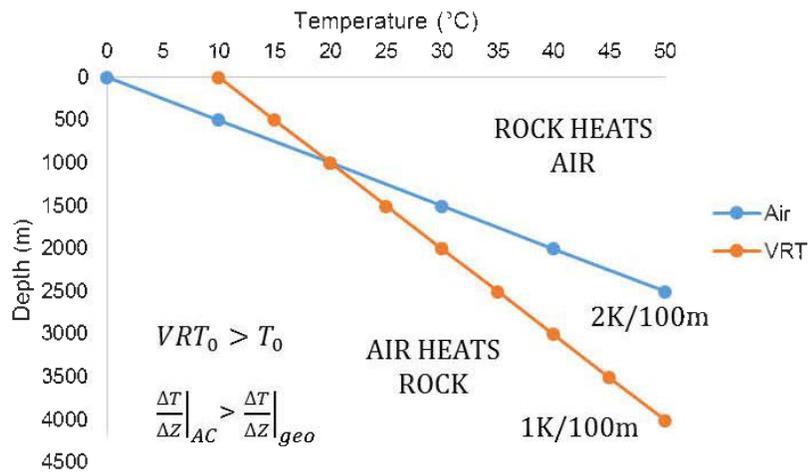
Figure 3: Canada winter nighttime where both effects occur.

If the surface air temperature is higher than the surface VRT, the ventilation air will be continuously cooled by the surrounding rock (Figure 4).
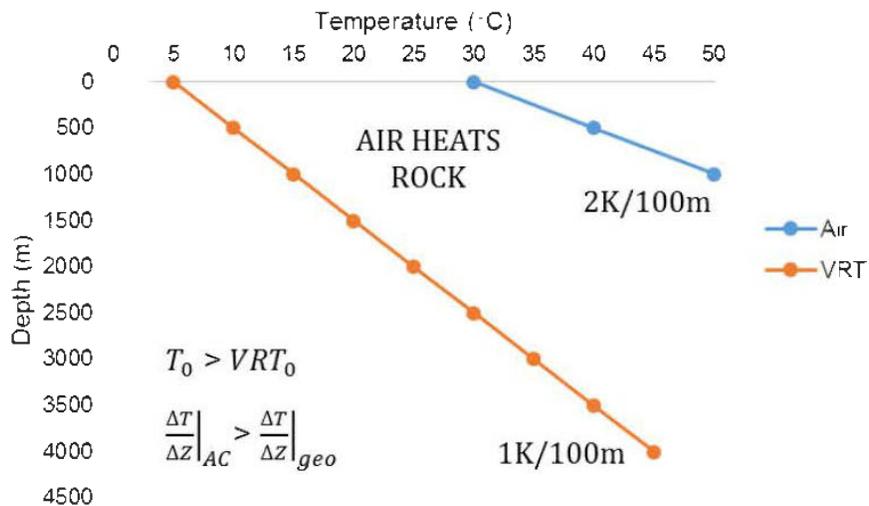
Figure 4: Canada summer daytime where surface air temperature is higher than the surface VRT
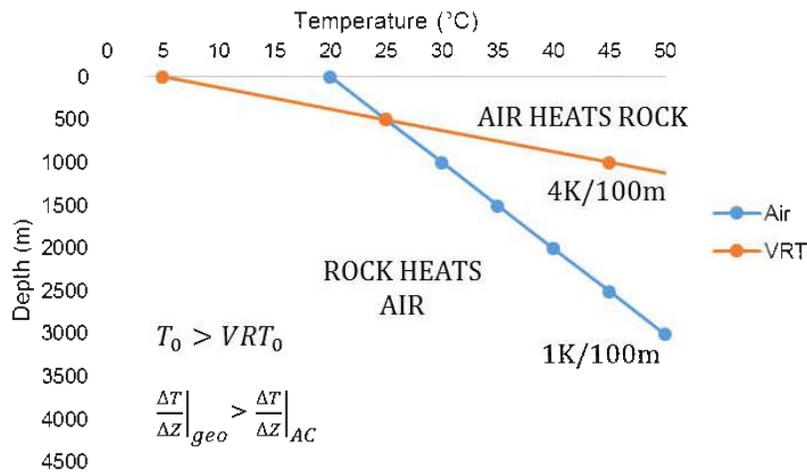
Figure 5: Cornwall summer nighttime where both effect occur.

In Figure 5, the surface air temperature is higher than the surface VRT but the increase of air temperature due to the autocompression is lower than the geothermal flux, due to decrease in surface temperature during nighttime. To understand the situation for particular shafts, computer simulations of ventilation air flows need to be carried out. The presence of water on tunnel surfaces can add heat to the air through latent heat mass transfers.

1.2.2   Latent heating/cooling and sensible heating/cooling

Whatever the condition of the air is at the air entry to mine workings, it is further modified by heat and mass transfers within the workings. The condition of air within and at the exit of the workings depends on those and also depends on conditions of dryness or wetness of the rock surfaces in the workings.

The wetness fraction over an entire surface of a tunnel can be back-calculated from measurements of the air flow properties at each end of the tunnel and the temperature distribution along the tunnel surface. The latter depends on the evaporation rate, which is driven by the psychometric properties of the bulk air and the bulk air velocity.

On Figure 6, it is possible to see how the magnitude of latent heat transfers depend on the wetness fraction and with depth.
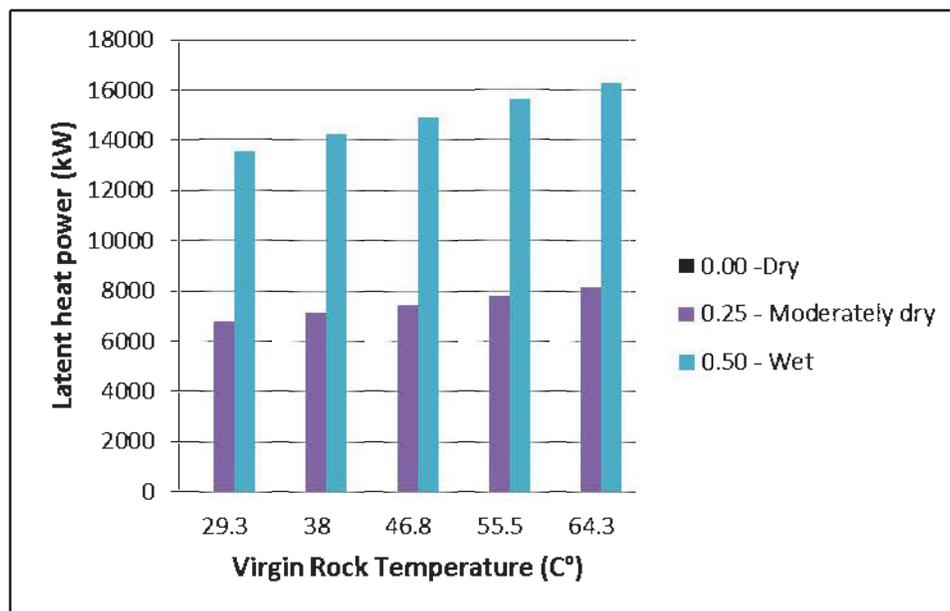
Figure 6: Impact of wetness fraction in latent heating power for varying working level depths (VRTs).

Figure 7, shows the magnitude of sensible heat transfers which depends on the wetness fraction and with depth. Total heating (positive +), cooling (negative -) is the sum of sensible and latent components.
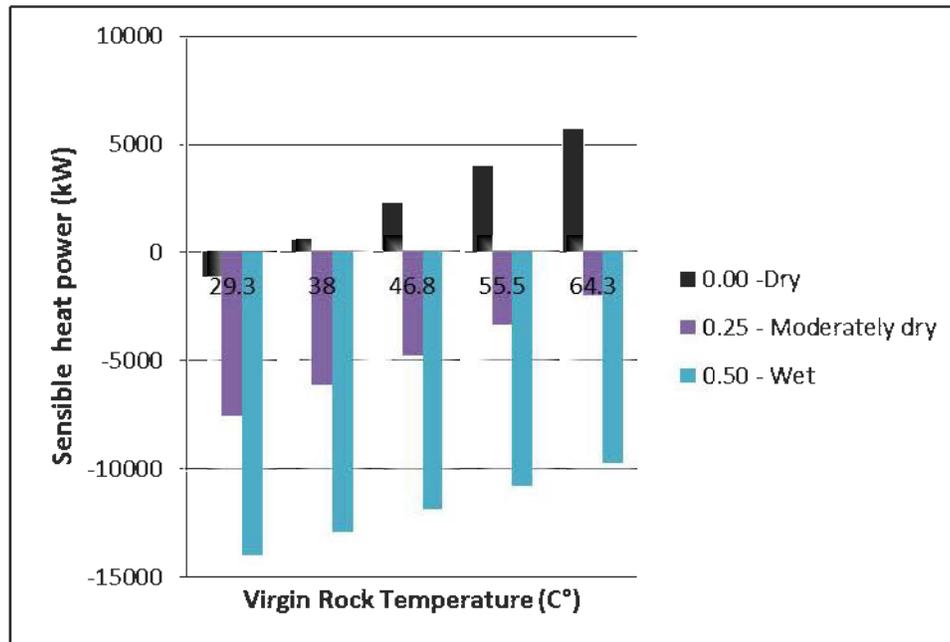
Figure 7: Impact of wetness fraction in sensible heating power for varying working level depths (VRTs).

For existing airways, the estimation of the wetness fraction is done by visual inspection or thermographic mapping. For planned, unconstructed, airways the estimation is done from previous experience with similar depths and geological settings. Humidity of the air is a dominant factor in assessing whether active cooling systems are acquired because workers are principally cooled through evaporative heat transfer of sweat (McPherson, 1993). Greater moisture content in the air reduces the effectiveness of the air to cool workers.

1.2.3 Broken rock underground

Another factor to consider for the mine ventilation is the broken rock underground. Schafrick (2014) using computational fluid dynamics and experimentation, reported a value of 0.238 kg/m^3 for the Atkinson friction factor applicable to bulked broken rock. From his determination, the heat loads from surfaces into the mine ventilation system can be identified. In order to do this, it is necessary to know four parameters, the average rate of broken rock produced (kg/s), the specific heat capacity of the broken rock (kJ/ kg°C), the temperature at which the rock exits the underground workings and the virgin rock temperature (VRT) of the surrounding rock. If the broken rock is wetted to reduce the dust, the rate of heating of the air by the broken rock is appreciably increased.

1.2.4 Other sources of heat in mine workings

It is important to highlight four other sources of heat. First, it is the auxiliary electrical equipment (e.g. ventilation system fans). A typical auxiliary fan may be rated at 112 kW (O'Connor, 2008), and at the end of the transit of air through an auxiliary ventilation system, all of this electrical power ends up as heat. Second, it is the static and mobile equipment: pumps, 50 kW (Oosthuizen, 2012); bolters, 24 kW (O'Connor, 2008); drill jumbos, 7 kW (O'Connor, 2008); lighting, 369kW for 7000 bulbs (Millar et al., 2014); and diesel, the amount of which varies according to the mine production (Grenier et al., 2000). Third, water sources, such as sprays, springs, drainage channels, water pools and wet material. Finally, during stope filling the cement heat of hydration 250 kJ/kg (Langan et al., 2002), and the oxidation of sulphide ore minerals, Pentlandite (Cemič and Kleppa, 1987), Chalcopyrite (Johnson and Steele, 1981) and Pyrrhotite

(Özdeniz and Kelebek, 2013) may increase the total heat load, that frequently can be forgotten.

1.2.5 Thresholds on underground air temperatures

The air temperature underground affects the work performance. The wet bulb globe temperature, WBGT, is use to define the limiting temperatures at which the worker can work continuously according to his/her task or rate of work. For indoors where the solar radiation is negligible,

$$WBGT = 0.7 \, T_w + 0.3 \, T_d \qquad (7)$$

Where T_w is the wet bulb temperature and T_d is the dry bulb temperature. In underground mines the dry bulb temperature can be used as the globe thermometer temperature as there is negligible solar radiation

Ontario recommends mining companies to use the WBGT, recommended by the American Conference of Governmental and Industrial Hygienists (ACGIH) and required by legislation in other jurisdiction (ACGIH, 2013). Mining companies used this guidance to express the acceptable threshold limit values (TLV) for WBGT. The action limit is applied for those workers that are not used to hot conditions.

Table 1: ACGIH threshold limit values for WBGT

ACGIH Screening Criteria for Heat Stress Exposure (WBGT values in °C)				
Allocation of Work in a Work / Rest Cycle	TLV (Action Limit)			
	Light	Moderate	Heavy	Very Heavy
75-100 %	31 (28)	28 (25)	na	na
50-75 %	31 (28.5)	29 (26)	27.5 (24)	na
25-50 %	32 (29.5)	30 (27)	29 (25.5)	28 (24.5)
0-25 %	32.5 (30)	31.5 (29)	30.5 (28)	30 (27)

1.2.6 Need for cooling

Sources of heating in underground mines have been presented in this section. The total heating power for Canadian mines can be in between 10 to 24 MW. This range represents the increases in heat load as depth increases. It has been shown that active cooling through refrigeration is required when the surface VRT is high and also when the depth increases. Conventional refrigeration systems cannot be used in some situations, even if they are desired, and this may be due to high cost, insufficient heat reject capacity, insufficient water or insufficient power. In such cases alternative cooling methods must be used, and there are many successfully deployed examples such as ice-stopes (Howes and Hortin, 2005), modular thermal transfer unit (MTTU) (Allen et al., 2012), lake cooling (Newman and Herbert, 2009) or seasonal thermal energy storage (Rutherford, 1958).

1.3 Aim of this work

The sources of heat additions in the sub-surface are of large magnitude (MW-scale) and involve both latent and sensible heat transfers. The threshold environmental conditions that are applicable are clear and embedded in mining regulations. Solutions for MW-scale active cooling are thus required as mines exploit deeper orebodies and these need to be provided at low cost, so that mine viability is not compromised. Candidate solutions will have low capital costs, will be simple in construction, will have high reliability so that maintenance and repair labour costs are low, and will have a long service life.
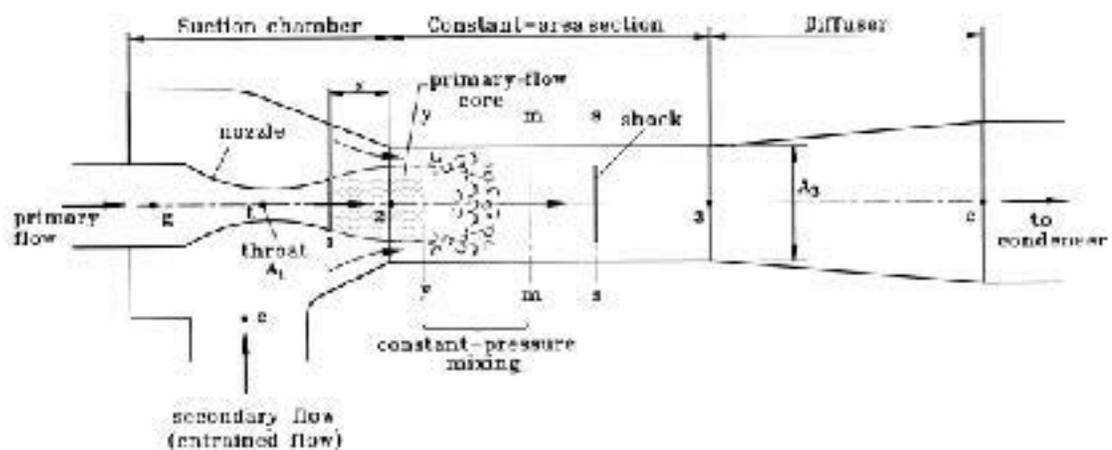
Figure 8: Schematic diagram of ejector performance (Huang et al, 1999)

Figure 8 shows a schematic of an ejector, comprising an internal convergent divergent nozzle inside a larger convergent divergent nozzle. This will be reviewed in detail subsequently, however at this stage it is important to note that i) the expanded gas leaving the internal convergent divergent nozzle can be engineered to be much cooler than the supplied primary flow and ii) the system in the diagram has no moving parts, and iii) the secondary flow is drawn into the ejector by the high speed primary flow. The cold primary flow mixes with the inducted secondary flow, so that the former cools the latter and a refrigerating effect is thus applied to the latter.

The compact general arrangement and no-moving-parts character of this cooling system certainly makes it interesting to consider for mine-scale refrigeration. In this context, the primary flow may be considered to be a stream of cheaply produced compressed air and the secondary flow may be considered to be the bulk mine ventilation air requiring cooling.

The primary flow will thus cool the mine ventilation air and add to the latter's mass flow for further benefit, but the key questions are:

1) Although ejectors are well established technologies at relatively small scale, can the working principle be scaled up to mine scales (of say, 4 to 5 meter diameter for the secondary air flow)?

2) Can this be done at a lower cost than the incumbent vapour compression refrigeration technology?

The answers to these questions principally lie in understanding the theory of air ejector performance and confirming this experimentally to enhance confidence in the proposal as a credible concept. Next a reliable, large scale and cheap source of compressed air is required to drive the ejector. In this thesis, the focus is on the optimal design of the ejector; designs for HACs to deliver on this objective are the concerns of others (Millar et al., 2016) and for the purposes of this work, this air is simply assumed to be available. Thereafter, conceptual designs for mine scale ejector refrigeration systems can be articulated so that the capital and operating costs associated with the concept can be reliably estimated. Economic performance metrics can then be established and compared with the incumbent to assess whether or not it is worthwhile to continue to pursue the concept to execution.

At the outset of investigations, the working hypothesis of the thesis was that it was possible to establish a MW-scaled rated ejector mine refrigeration concept. The thesis effort was directed towards design effort, modelling and experimental work that tried to prove this hypothesis.

1.4 Research methodology

The following methodology is used to respond the research questions. In order to appropriately respond the research questions, in each subheadings is identified with the work done in that chapter.

- Chapter 2 will report the literature review undertaken, focusing on refrigeration systems, to explain the functions of the hydraulic air compressor and the ejector in the proposed refrigeration cycle.

- Chapter 3 firstly reviews the literature on ejectors specifically with the objective of identifying how they be optimally designed for specific, defined, duties.

- Chapter 4 discusses the method that may be used to design the motive nozzle of an ejector for its primary flow.

- Chapter 5 will report an outline description of the Computational Fluid Dynamics (CFD) model and explains its connection with chapter 3. Then a literature review on previous CFD ejector studies is presented. Next, the two simulations designed: one for mine scale and other for laboratory test will be presented. Finally, the analysis of results to understand the behaviour and the design suggested for better performance is explained.

- Chapter 6 highlights the laboratory test in order to verify the CFD model. In this chapter, the fabrication of the model is explained with the test conditions and instrumentation used for this purpose. Then the results of the physically experiments are presented.

- Chapter 7 explains the different results and findings. This chapter presents discussions relating to the ejector design, CFD results, experiment findings and implications for cooling sub-surface.

- Chapter 8 summarizes the achievements of this work and offer different approaches for further studies. In this chapter conclusions are presented relating to the research questions posed in chapter 1 and the additional findings. These conclusions are referenced to the current development status of the ejector and a summary of recommended further work is introduced.

CHAPTER 2

REVIEW OF THE THEORY AND CONTEXT OF REVERSE BRAYTON REFRIGERATION CYCLE

This chapter presents an overview of previous works related to the technology under study and discusses the techniques used to accomplish the proposed analysis.

The conditions in an underground mine depend mainly upon the air properties, rock properties, airway properties, virgin rock temperature and humidity of the rock. According to De Souza, (2015), the mine ventilation system accounts for 25-40% of the operation costs and for 40-50% of energy consumption. Thus choosing the right system for removing heat from deep mines is vital, especially for mines where the value of the mineral product is low or declining.

2.1 Vapor compression refrigeration systems

As mines get deeper, and the various heat loads on the ventilation air increase, so there is a need to consider heat removal systems. One of the first methods of refrigerating underground mines was by sending blocks of ice to the sub-surface. This was the method of choice until the industrial revolution where the mechanical vapour compression refrigeration cycle was adopted at the beginning of 20th century (McPherson, 1993). The first plant for mine underground refrigeration went into operation in 1920, producing 80000 cfm, 37.75 m^3/s of dry air, at the Morro Velho

mine, Nova Lima, Minas Gerais, Brazil (Davies, 1922). Unfortunately this kind of system had a low coefficient of performance (COP) around 60%.

$$COP = \frac{Refrigeration\ effect}{Net\ work\ input} \qquad (8)$$

The vapor compression system is the most conventional refrigeration system in at the present time. The vapor compression system consists of four elements: evaporator, compressor, condenser and expansion valve. Refrigeration effect is delivered at the evaporator because it behaves as a heat exchanger causing a wet vapour to become saturated vapour by vaporizing the liquid component in drawing heat from the evaporator surroundings. The refrigerant is then pressurized at the compressor which also increases the refrigerant temperature. The elevated vapour temperature (in comparison to the condensor's surroundings) causes heat to leave the refrigerant and it condenses to a liquid state. Finally, the pressure is reduced in an expansion valve through throttling and the refrigerant flashes to a wet vapour at the evaporator pressure, allowing the cycle to restart. The best approach to calculate the COP is to assume an ideal process and allow for process irreversibilities with an isentropic efficiency for the compressor and frictional pressure drops for the pipework losses. These irreversibilities decrease the COP and refrigeration capacity

During the 1970s, surface refrigeration plants were extensively installed in deep South African mines. These modern units have relatively high COPs of around 4, due to relatively low atmospheric air reject temperatures. However, according to Sheer et al., (1986) when careful analysis of the coefficient of performance (COP) of the refrigerator systems was undertaken, effective COPs were found to reduce by 25% to 3, as the mining depth increased from 3000m to 4000m depth. Refrigeration costs were increased unacceptably.

For these surface plants, the issue became that while the refrigeration effect available at the plant remained high, the effective refrigeration effect available where

it was required at depth was much lower. However the refrigeration effect was delivered at depth, the inevitable fact was that on its way to the subsurface, whatever medium was involved, heated up. Consequently, a concept of 'positional efficiency' was developed, and vapor compression systems began to be installed underground.

Underground vapor compression refrigeration systems still need to reject condenser heat. On surface cooling towers can be readily constructed to achieve this. Warm condenser cooling water is sprinkled downward against an updraft of atmospheric air, then cooled water is returned to the condenser. Underground, cooling towers need to be constructed in voids excavated in rock, appreciably increasing their cost. Also, the temperatures of updrafting air underground are appreciably higher than the temperatures of updrafting air on surface, mainly due to autocompression and geothermal heat transfer. To provide the same cooling effect to the condensers, more updrafting air needs to be supplied to the cooling tower than an identically rated system on surface. Underground the condenser temperature has to be maintained higher to maintain the same temperature difference between refrigerant in the condenser and the condenser coolant. Operating a condenser a higher temperature means that the compressor in the cycle needs to work harder because the condenser pressure is correspondingly higher, dictated by the refrigerant properties.

Supplying more updrafting air quickly becomes sub-economic because the air power varies with cube of the volume flow rate, so the normal course of action is to run the condenser at a higher pressure. As a direct consequence the COP falls. In general, a vapor compressor refrigeration plant that will operate with a COP of 4 on surface, will operate with a COP of 3 underground. So a trade-off exists of energies between a surface compression refrigeration plants with a high COP but low positional efficiency, and an underground vapor compression plant that has high positional efficiency but lower COP. Consequently, an ongoing drive for innovation in mine refrigeration still exists, because vapor compression refrigeration options begin to

become very expensive as depth increases. Without such innovation, mine refrigeration systems can only be afforded by mines producing the most valuable commodities (such as gold and gems)
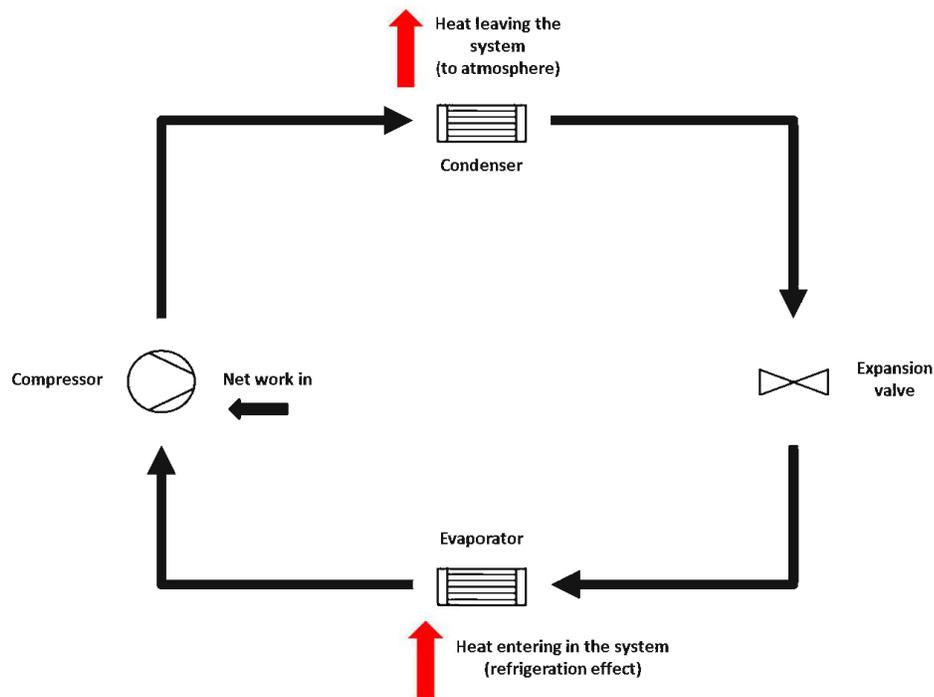
Figure 9: Vapor compressor refrigeration cycle

2.2 Brayton Power and Refrigeration Cycles

Power and refrigeration systems are governed by the thermodynamic cycles. The former are systems that produce power output, the latter are used for refrigeration and require power. These thermodynamic cycles are also divided into vapor or gas cycles depending on whether or not there is a change in phase of the working fluid. They can also be classified as open or closed cycles, where open means the working

fluid is continuously renewed instead of the same fluid being recirculated. Vapor compression systems are limited by the evaporator temperatures. Sometimes there is such a great need for 'coldness' that much lower temperatures than these are needed. In such cases, the refrigerant adopted may have to change to one that does not change phase. When this occurs, the refrigeration cycle changes too, from a vapor compression system to a reverse Brayton cycle.
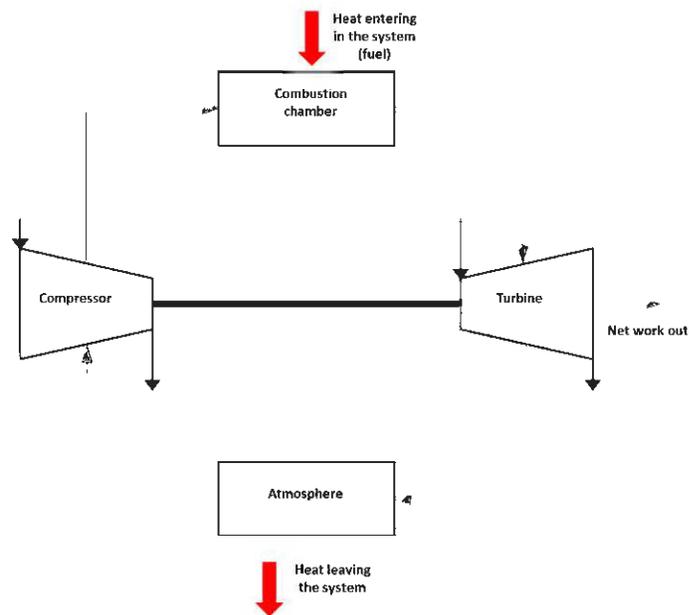
Figure 10: Equipment for an open Brayton cycle power plant
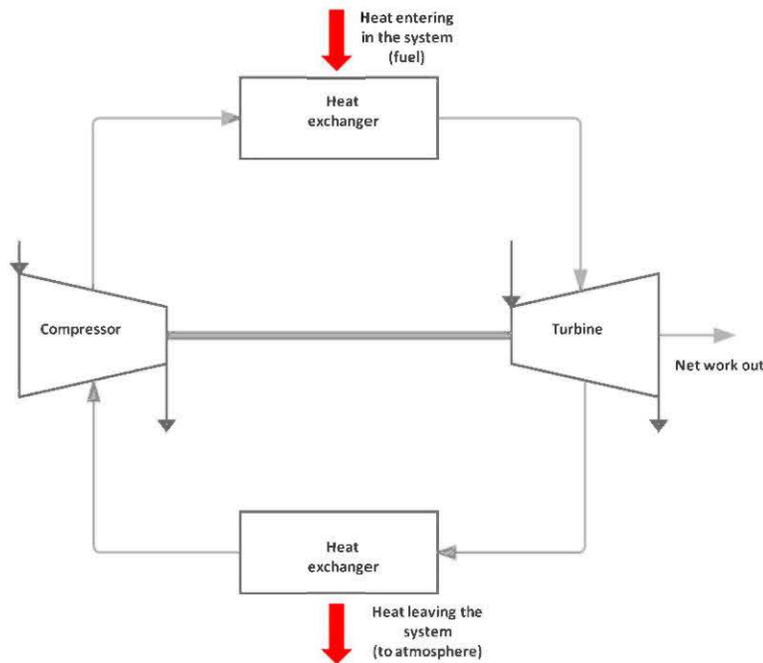
Figure 11: Equipment for a closed Brayton cycle power plant

A Brayton cycle for refrigeration is best explained by first considering a Brayton cycle for power production.

In the Brayton power cycle, work input to the compressor increases the pressure of the circulating gas which is considered the 'system'. Then, at a relatively high temperature, heat is added to the gas in the form of combustion heat, raising system enthalpy. The high enthalpy gas is passed to the turbine in which the gas expands, depressurizes and cools. The high enthalpy of the inlet gas is converted to turbine shaft work and low enthalpy outlet gas. Low pressure, lower temperature gas leaves the turbine and then undergoes an isobaric cooling process either i) indirectly, in a heat exchanger, so that heat leaves the system and passes to the surroundings in the closed cycle (Figure 11) or ii) directly, by mixing and intermingling with the surrounding atmosphere in an open cycle configuration (Figure 10).

In the reverse Brayton refrigeration cycle (RBRC), after compression, heat leaves the system, passing to the surrounding atmosphere in a heat exchanger that behaves as an aftercooler. The aftercooler process is approximately isobaric at highest temperature in the cycle. The gas then passes to a turbine, depressurizes, delivers work and cools to the lowest temperature in the cycle, and thereafter enters a second heat exchanger where it undergoes an isobaric heating process, drawing in heat and providing the refrigeration effect.

The physical configuration of RBRC and Brayton power cycle plant components is identical, and the sense of the flow through these identical components is identical too. The essential difference between the power and refrigeration cycles is the sense of the heat transfers at the heat exchangers, and the temperatures at which these two transfers occur. For the power cycle, the net work leaving the system is positive (Figure 11), for the refrigeration cycle the net work entering the system is positive (Figure 12).
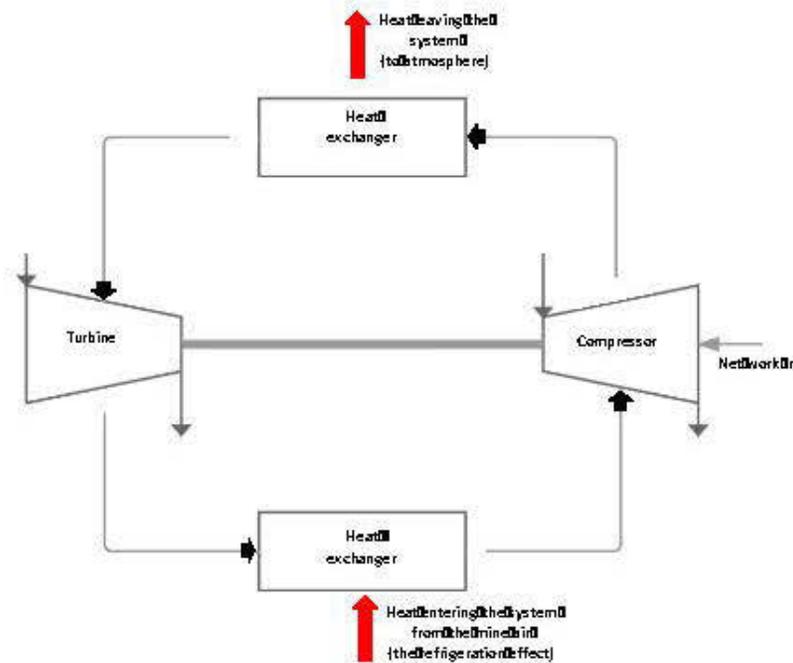
Figure 12: Equipment for a closed Brayton cycle refrigeration plant

An initial analysis of the cycle can be done by assuming that all the processes are ideal and reversible. In reality, this is not the case, and irreversibility needs to be accounted for. Irreversibilities in the Brayton cycle can be depicted on a thermodynamic cycle as blue process lines superimposed on the red process lines representing the ideal gas cycle, as in Figure 13.
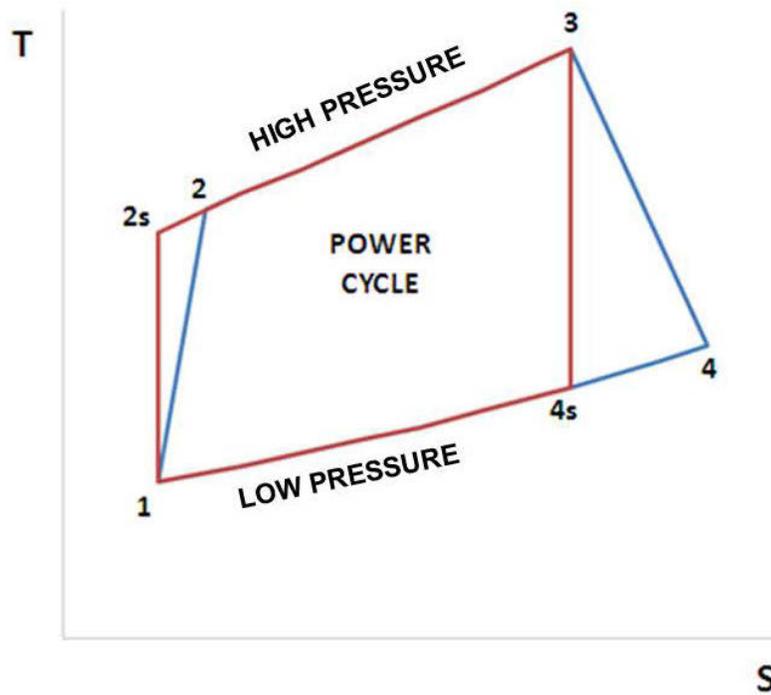
Figure 13: Ideal and non-ideal Brayton power cycle

The reversible or ideal cycle comprises four processes:

- 1-2s Isentropic compression in the compressor
- 2s-3 Constant-pressure (isobaric) heat added (fuel heat added in a combustion)
- 3-4s Isentropic expansion in the turbine
- 4s-1 Isobaric heat removal

The irreversible or real cycle:

- 1-2 Actual compression in the compressor, deviating from the ideal compression by an amount controlled by the compressor isentropic efficiency.
- 2-3 Constant-pressure heat added

- 3-4 Actual expansion in the turbine
- 4-1 Constant-pressure heat removal

Due to frictional losses and other irreversibilities inside the compressor and the turbine, there is a system entropy increase 1-2 and 3-4. There are also frictional losses inside the heat exchangers that will reduce pressure for processes 2-3 and 4-1 normally assumed isobaric. In comparison to pressure changes in of the compressor and turbine they are negligible, and support an assumption of constant-pressure in these processes. The main difference between ideal and actual cycles is that there is greater actual work input to the compressor and less actual work output in the turbine, substantially reducing cycle efficiency. In order to account for the deviation from the ideal process isentropic efficiencies are introduced, defined by the application of the steady flow energy equation (SFEE) for the real and ideal process, compressor and turbine processes.

$$\frac{(V_1{}^2 - V_2{}^2)}{2} + g(Z_1 - Z_2) + W_{12} = \int VdP + F_{12} = h_2 - h_1 - q_{12} \qquad (9)$$

For the compression process:

$$\eta_{isen\,comp} = \frac{W_{12s}}{W_{12}} = \frac{h_{2s} - h_1 - q_{12s} - \frac{(V_1{}^2 - V_{2s}{}^2)}{2} - g(Z_1 - Z_{2s})}{h_2 - h_1 - q_{12} - \frac{(V_1{}^2 - V_2{}^2)}{2} - g(Z_1 - Z_2)} \qquad (10)$$

With approximately similar velocities, V little variation in elevation Z and no heat transfer $q_{12}=0$:

$$\eta_{isen\,comp} = \frac{h_{2s} - h_1}{h_2 - h_1} \qquad (11)$$

where h_i = specific enthalpy (kJ/kg) of cycle state point i.

Similarly, for the expansion process:

$$\eta_{isen\ turbine} = \frac{h_3 - h_4}{h_3 - h_{4s}} \tag{12}$$

For the reversible adiabatic isentropic processes of compression in the compressor and expansion in the turbine:

$$Pv^\gamma = C \tag{13}$$

where γ is the isentropic coefficient of an ideal gas defined with a constant ratio of specific heat. The ideal gas equation of state

$$Pv = RT \tag{14}$$

is also assumed to hold. For the ideal gas, the pressures and temperatures for the two processes with the same isentropic coefficient are, thus:

For the compressor:

$$\frac{T_2}{T_1} = \left(\frac{P_2}{P_1}\right)^{\frac{\gamma-1}{\gamma}} = r_p^{\frac{\gamma-1}{\gamma}} \tag{15}$$

where r_p is the compressor compression ratio, and

For the turbine:

$$\frac{T_4}{T_3} = \left(\frac{P_4}{P_3}\right)^{\frac{\gamma-1}{\gamma}} \tag{16}$$

and the efficiency of the power cycle as a whole is defined:

$$\eta_{cycle} = \frac{Net\ work\ output}{Gross\ heat\ input} = \frac{W_{34} - W_{12}}{q_{23}} \tag{17}$$

The equipment required for refrigeration cycle and power cycle are the same; the key differences are the sense of the cooling or heating effect and net work. Power and refrigeration cycles together, and their irreversibilities are represented in Figure 13.
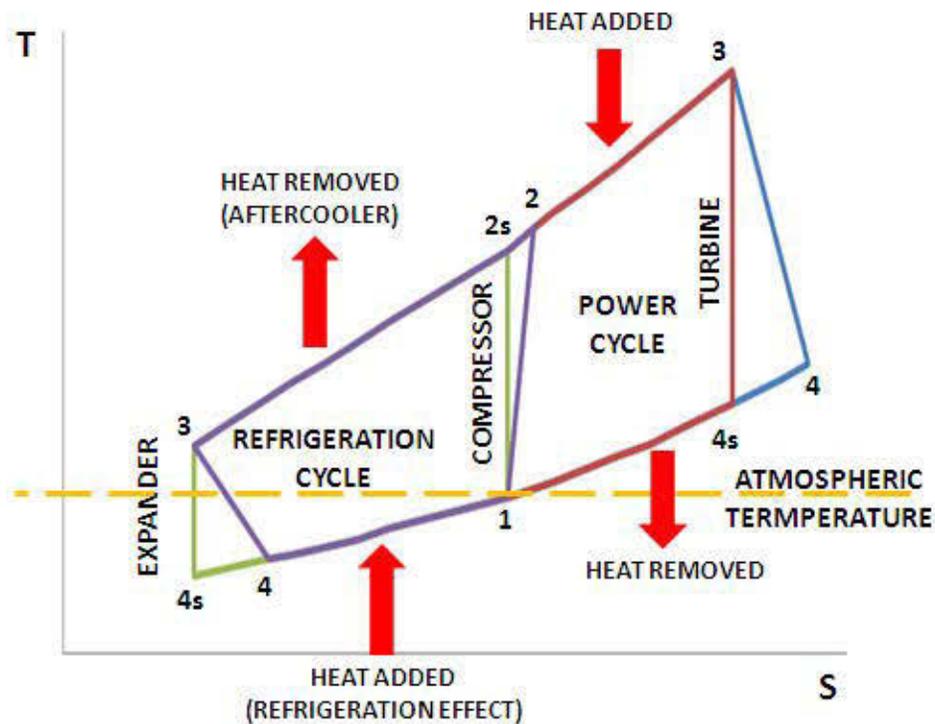
Figure 14: Brayton Refrigeration and Power cycle

In refrigeration cycles the COP or coefficient of performance is used to quantify this performance which has a direct impact on the cost. That is, the cooling effect divided by the net work input.

$$COP = \frac{\dot{Q}_{in}}{\dot{W}_{cycle}} = \frac{\dot{m}(h_1 - h_4)}{\dot{W}_{compressor} - \dot{W}_{turbine}} = \frac{(h_1 - h_4)}{(h_2 - h_1) - (h_3 - h_4)} \qquad (18)$$

Higher COPs mean low operating cost because the net work input is lower for the same refrigeration effect. For instance, if the COP of the refrigeration system is equal to 3, it will consume 1 kWh of work to remove 3 kWh of heat; if the COP is 2, 1.5 kWh of work is required to remove 3 kWh of heat. Therefore, with the same energy source and operating conditions, a higher COP system will consume less energy than one with a lower COP, saving costs.

Understanding the thermodynamic cycle leads to performance measures, such the cycle efficiency for the power cycle and the COP for the refrigeration cycle, that enable the operating cost to be estimated and the techno-economic performance to be quantified.

2.3 Applying RBRC to cooling for deep mines

The RBRC has been considered an unconventional cooling system for mining applications. In 1988 Del Castillo , proposed a RBRC ventilation system for deep mines, as presented in Figure 15, but so far such an idea has not been implemented in practice.
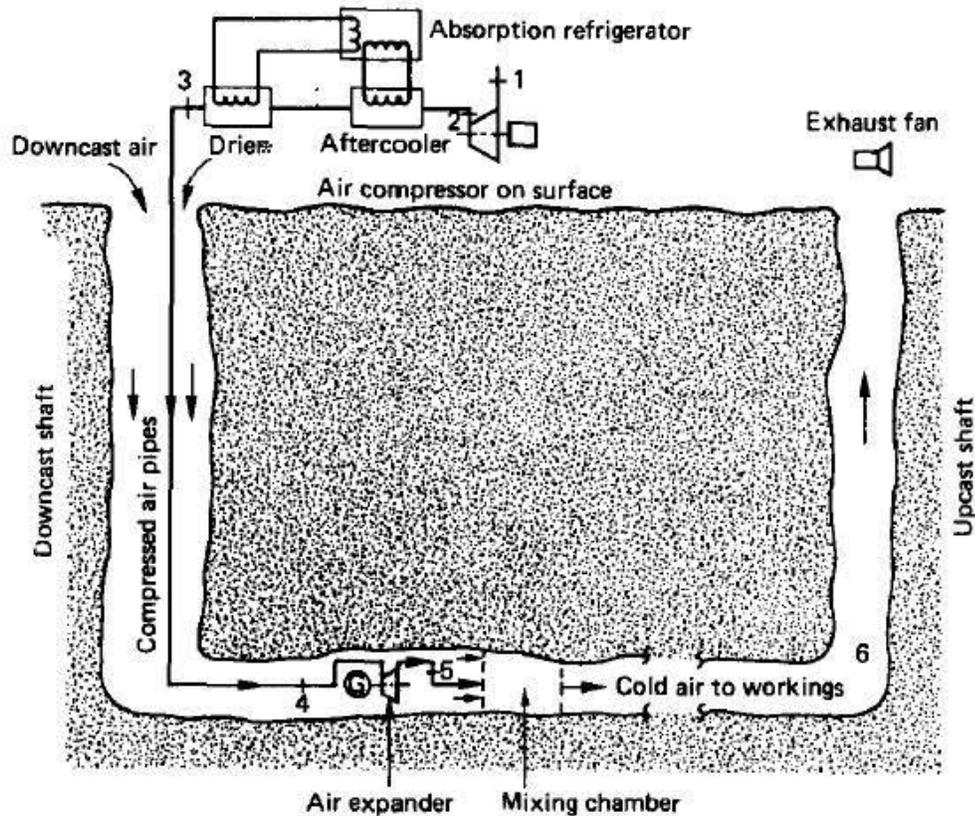
Figure 15: Schematic diagram RBRC from Del Castillo (1988)

The atmospheric air goes through the compressor (1-2), then through the aftercooler (2-2*), and finally the drier (2*-3), on the surface before it is sent underground in a compressed air range via the downcast shaft. The compressed air undergoes a compression process while it descends, in the same way that ventilation air in the shaft suffers autocompression, and this leads to state 4. Next the compressed air expands through a turbine (air expander) and cools to 5 simultaneously producing work at the turbine shaft. In Del Castillo's concept, the turbine work is used to produce electricity. The cold expander exhaust air and the gallery air mix and the air is sent to the workings where the refrigeration effect is consumed. This means, the isobaric heating of the system is direct, and the cycle is open. After being used, this heated air

together with the cooled ventilation air passes back to the surface and the atmosphere via the upcast shaft. As it passes up the shaft, this return air will depressurize and cool, possibly adiabatically depending on the geothermal gradient, as explained for autocompression of the intake ventilation air, and, if there is moisture in the air at the bottom of the upcast shaft, the air may be taken through its dew point, producing fog or rain, in the upcast shaft

The process just explained can be represented on a schematic thermodynamic T-S diagram; this is illustrated below in Figure 16.

- 1-2: Adiabatic compression in the compressor.
- 2-3: Compressed air is cooled to approximately atmospheric temperature in 3. In this case, the air is cooled and dried in an aftercooler.
- 3-4: Compression through downcast shaft, inside the compressed air range, increasing the temperature and pressure. In the process 3-4, the pipeline friction increases the entropy, but whether the state of the compressed air ends up at 4 or 4A depends on the sense of heat transfer across the pipeline wall, that is, the temperature difference between ventilation air and compressed air as they descend.
- 4-5 Expansion in the turbine
- 5-6 Mixing with gallery air and delivery of the cooling effect to the gallery air using direct contact mixing with the turboexpanded air.
- 6-1 Discharge to the surface via upcast shaft.
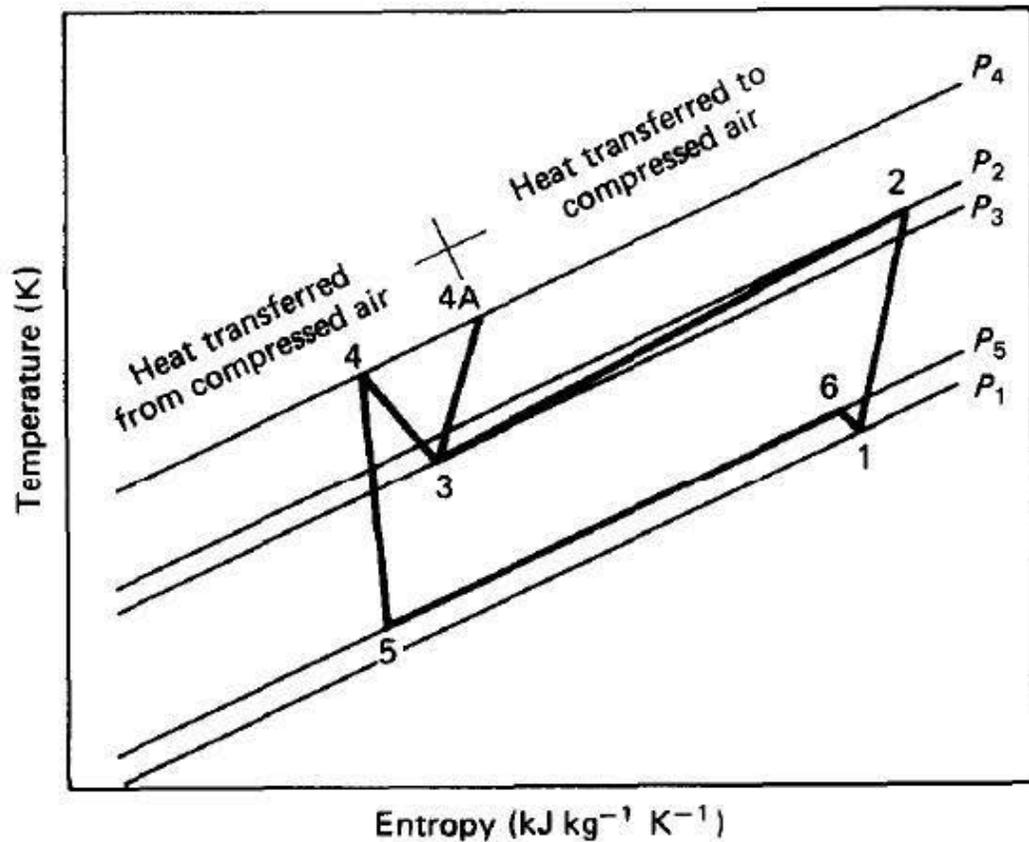
Figure 16: Schematic T-S diagram for the cooling air, in Del Castillo (1988) air cycle system

The performance of the system depends on the pressure ratio of the compressor. For instance, if a low compressed air pressure ratio applies, the mass flow of compressed air should increase to meet the cooling demand which means more electricity is needed. The COP in this case will be higher for low compression ratios and the costs are inversely proportional to the COP. In order to establish the minimum cost of refrigeration effect, the optimum pressure ratio must be determined.

A key part of the context of the work of this thesis is that a hydraulic air compressor (HAC) replaces the conventional compressor in Del Castillo's system. In order to

understand the benefits of use of a HAC, a comparison between a RBRC with a conventional and hydraulic air compressor is made in Figure 17. The HAC offers an isothermal minimum work compression process, whereas a conventional compressor does not.
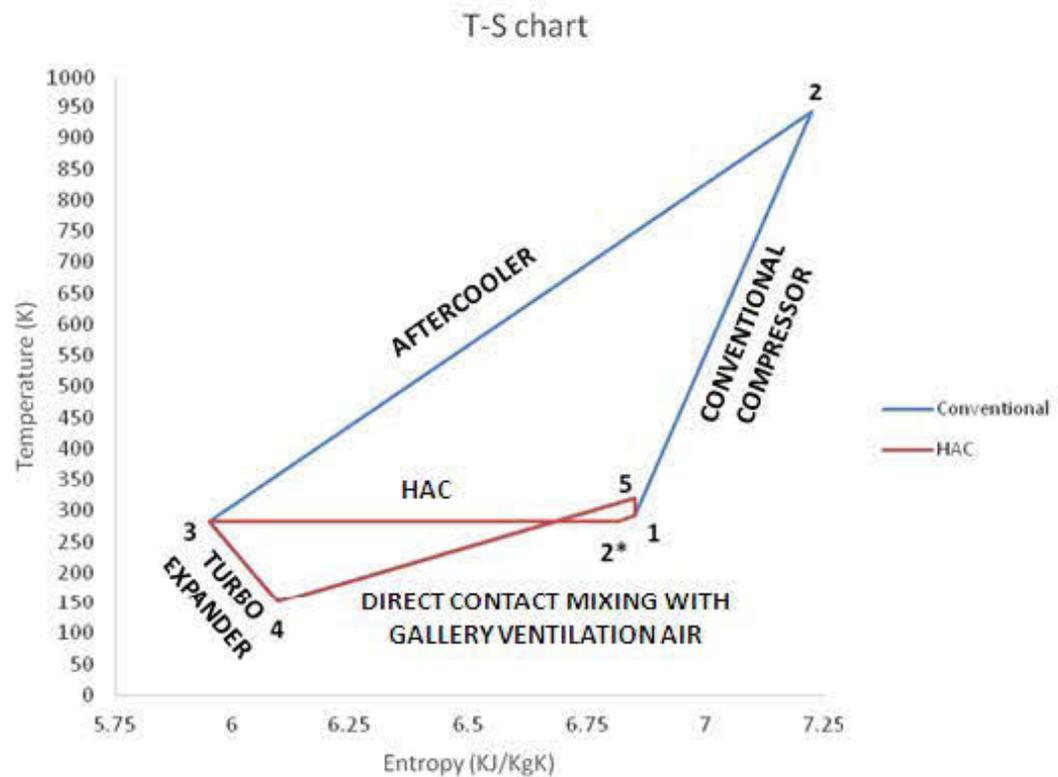
Figure 17: RBRC with conventional compressor with aftercooler (blue) and HAC (red)

Conventional:

- 1-2 Irreversible adiabatic compression in the compressor.
- 2-3 Constant-pressure cool down to ambient temperature (after cooling).
- 3-4 Actual expansion in the air expander.
- 4-5 Mixing with mine air and warming of cycle air.
- 5-1 Pressure reduction to atmosphere in upcast shaft.

HAC

- 1-2* Drop in temperature (by mixing with cooler water in the HAC).
- 2*-3 Compression at constant temperature (minimum work).
- 3-4 Irreversible expansion in the air expander.
- 4-5 Mixing with mine air and warming of cycle air.
- 5-1 Pressure reduction to atmosphere in upcast shaft.

The COP of both systems is given by

$$COP = \frac{\dot{m}(h_1 - h_5)}{\dot{W}_{compressor} - \dot{W}_{turbine}} \tag{19}$$

but by introducing the HAC into Del Castillo's RBRC concept for mine cooling, due to the isothermal compression process offered by the HAC, less work input is required in the compressor process of the cycle, and this means that the COP

increases. The proposal herein is thus a significant advance on Del Castillo's concept, and merits a brief review of HAC operation at this juncture in the thesis.

2.4 Hydraulic Air Compressor

A Hydraulic Air Compressor (HAC) is an historical technology which was forgotten even if , approximately 21 installations around the world were using this technology according to (Schulze, 1954). A HAC is a device which is able to use the potential energy of water to compress air. The system is schematically illustrated in Figure 18.
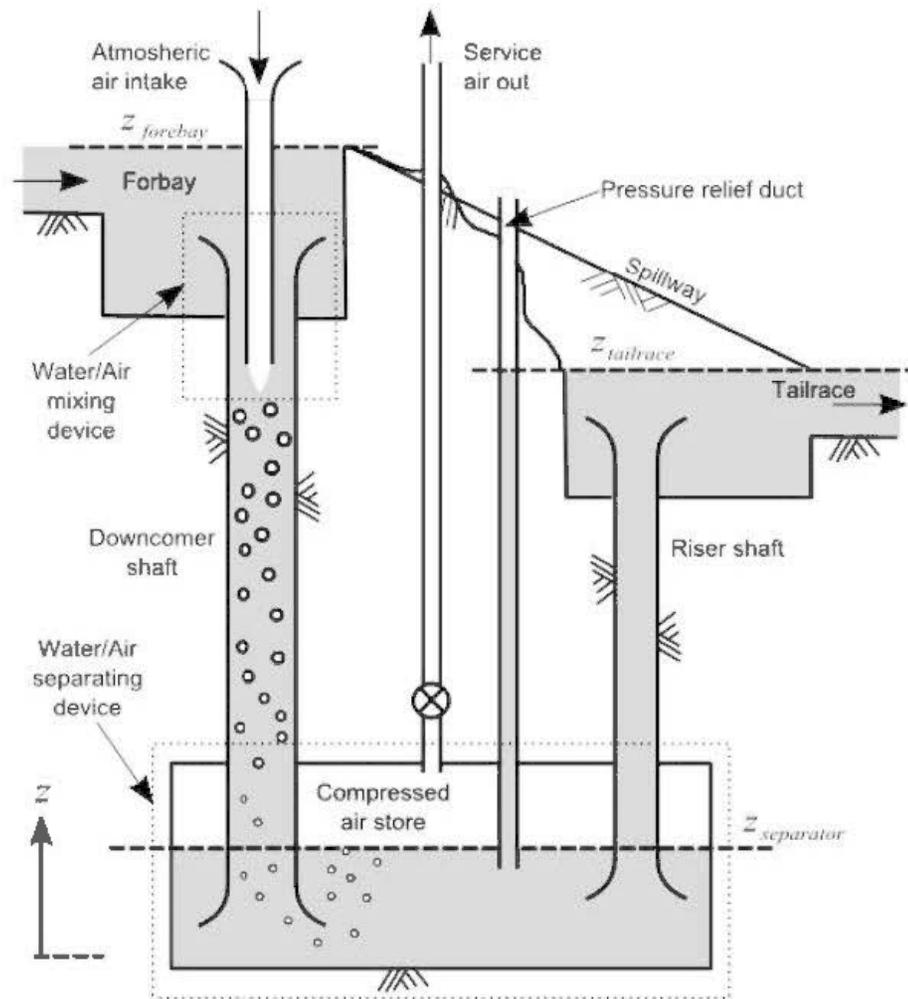
Figure 18: HAC Schematic (Millar, 2014)

Water, from a watercourse such as a river, behaves as the motive fluid in an ejector structure that drags the atmospheric air down into the shaft. The potential energy of the water is converted into pressure energy, which is transmitted to the air bubbles and to compress the gas within them. A separation device separates both fluids at the bottom of the shaft. In the separator, the velocities are reduced because the cross sectional area of the separation device is large in comparison to that of the downcomer shaft. In the separator, the low velocities introduce insufficient drag on the bubbles to overcome buoyancy so the bubbles rise and coalesce in a compressed air plenum. The

compressed air is sent for service through the service air out pipe. The water free of bubbles, passes to a so-called riser shaft and depressurizes as it ascends. It returns to atmospheric pressure as it rejoins the water course at the tailrace.

The first application of a HAC was in 1896 in a cotton mill at Magog, Quebec, Canada (Taylor, 1913)

Figure 19: HAC in Ragged Chutes (Taylor, 1913)

The most recent installation was done by Taylor (1913), at Ragged Chutes, Cobalt, Ontario, Canada. It is the largest of the 21 installations around the world, but only 17 cases are fully confirmed according to Table 2 (Millar, 2014), based on Langborne, 1979.

Table 2: HAC installations (Langborne, 1979)

No.	Year	Location	Available head		Water flowrate		Air flow @ atm p.		Delivery pressure		Eff.
			(m)	(ft)	(m^3/s)	(ft^3/min)	(m^3/s)	(ft^3/min)	(kPa)(g)	(psig)	(%)
1	1896	Dominion Cotton Mills, Magog, Quebec, Canada	6.58	21.6	2.92	6183	0.67	1419	359	52	55
2	1898	Ainsworth, British Columbia, Canada	32.77	107.5	1.98	4200	2.41	5100	600	87	53
3	1898	Dillingen Ironworks, Dillingen, Sear, Germany	1.80	5.9	0.77	1627	0.144	296	124	18	79
4	1901	Cascade Range, Washington State, USA	13.72	45	1.42	3000	0.76	1620	586	85	
5	1902	Norwich, Conn., USA							559	81	
6	?	Peru									
7	1903	Glanzenberg Mine, Nr Siegen, Germany I	40.00	131	0.0142	30	0.0191	40.5	811	117	74
8	1903	Glanzenberg Mine, Nr Siegen, Germany II	50.00	164	0.0147	31	0.0245	51.9	709	103	70
9	1903	Glanzenberg Mine, Nr Siegen, Germany III	17.00	55.8	0.0142	30	0.0082	17.4	709	103	70.2
10	1904	Trent Canal Lift Lock, Peterborough, Ontario, Canada	2.74	9			0.14	300	193	28	
11	1905	Holzappel, Germany	117.04	384	0.018	38	0.072	152	627	91	66
12	**1906**	**Victoria Mine, Ontonagon County, Michigan, USA**	**21.60**	**71**	**21.20**	**45000**	**16.50**	**35000**	**807**	**117**	**82**
13	1907	Royal Mine Inspection Plant, Clausthal, Germany	99.30	325	0.053	113	0.17	353	510	74	77
14	1908?	Zeche Victor Rauxel Mine, Dortmund, Germany	82.00	269	0.07	141	0.17	350	607	88	73
15	1909	Royal Mine Inspection Plant, Grund, Germany	36.00	118	0.157	333	0.193	408	607	88	88
16	**1909**	**Ragged Chutes, Nr Cobalt, Ontario, Canada**	**16.50**	**54**	**22.70**	**48000**	**18.88**	**40000**	**827**	**120**	**83**
17	1915	Persberg, Sweden	29.57	97	0.003	5			689	100	45-57
18	1924?	Cumberland, England									
19	1925	Falun, Sweden	47.85	157	0.18	381	0.60	1271	758	110	46-52
20	1929	Saragossa, Spain	1.83	6	2.83	6000			103	15	
21	1929	Nigeria, Tin mine									

The Ragged Chutes installation had the following characteristics:

Table 3: Ragged Chutes Installation

Place	Parameter	m	ft
Two downcomer shaft	diameter	2.6	8.5
	length	107	351
Separation chamber	wide	6.1	20
	high	7.9	26
Riser shaft	diameter	6.7	22
	length	91	298

With this configuration the Ragged chutes facility was able to deliver a pressure of 120 psig (822 kPa gauge) and 22.3 kg/s (40 kcfm or 18.9 m^3/s) of free air, using 5500 hp or 4.1 MW of hydropower, according to Schulze, (1954).
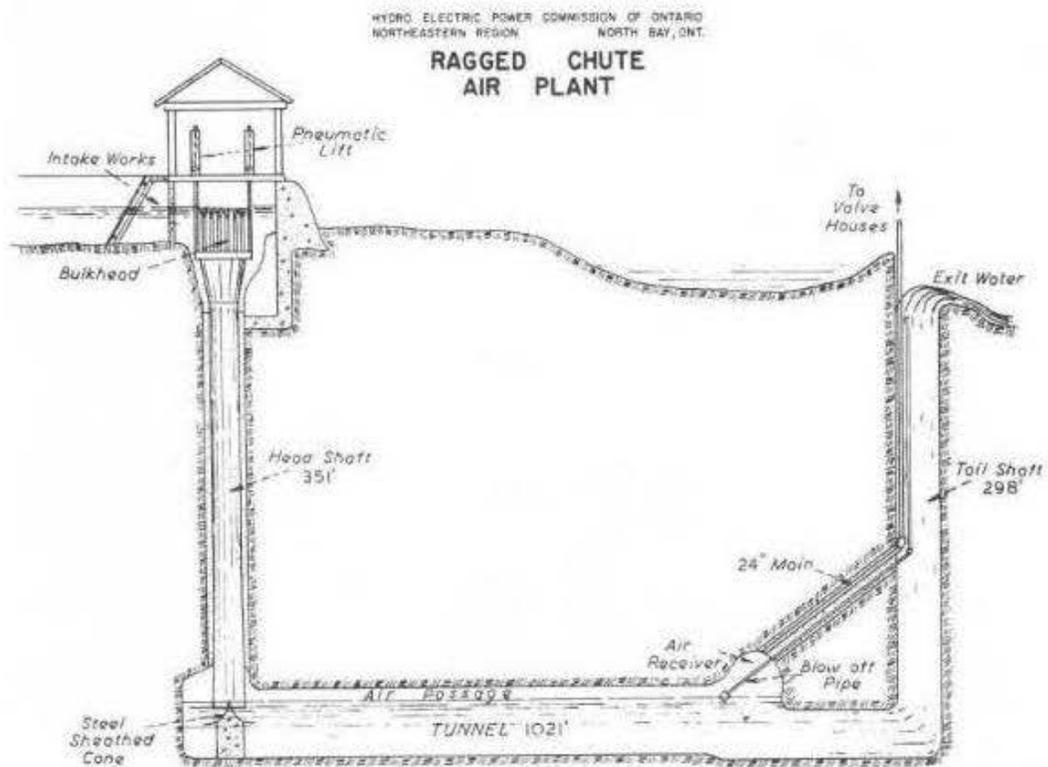
Figure 20: Ragged chutes from Auclair (1957)

Two important aspects of the HAC operation are the air drier effect and the constant temperature. The air drier effect arises as a consequence of the fact that the saturation vapor pressure of humid air reduces as the total pressure increases. In a HAC, while it may be expected that the air is always saturated (relative humidity 100%), the increase in pressure during air descent will cause the air to reach its dew point so that airborne humidity condenses. Condensate water will simply coalesce with the primary water flow of the HAC downcomer. The HAC air-water separator thus simultaneously acts as an air drier in the sense that liquid water is removed from the air. For a conventional compressor, an air drier is required as a separate component, as shown on Del Castillo's system. Use of a HAC as the compressor in a RBCR system thus leads to a simpler system, and more reliable concept than that of Del Castillo, a second significant advance.

Due to the heat dissipation from air bubbles into the water, the expected increase in temperature of a gas as it is compressed during a compression is not evident in a HAC; the process is almost isothermal. The water acts as a heat sink because the mass flow of water is ~1000 times greater than that of the air, in typical operating conditions Table 3.

The isothermal compression process of the HAC requires lower specific work to compress gas in comparison to the adiabatic processes considered earlier for conventional compressors. In the latter, a desire to approximate an isothermal compression process is the reason why intercooling and aftercooling heat exchangers are commonly adopted in multistage mechanical compressors. In a HAC, there are, in effect, an infinite number of compression stages, and an infinite number of intercoolers.

Auclair, (1957) in his report confirmed that, the ability of the system to deliver the air drier and the advantage of less work than an adiabatic process, which is typical of conventional compressors, were the HAC's main attractions. This behavior was reviewed by Bidini et al., (1999) and later by Millar (2014). Since the temperature increase is

small, a new description of the process in the HAC downcomer was studied by Pavese et al., (2016) and called the 'Nearly Isothermal Process'.

The main challenge to widespread adoption of HAC technology has been the requirements for a water course close to a compressed air demand centre. Following the design of the Peterborough Lift Lock HAC, Young et al. (2015) report on a conceptual design of a modern-day HAC, with a circulating water flow that does not require a natural water course. This overcomes the constraint reducing the more widespread applicability of HACs

2.5 Applying HAC to cooling for deep mines

In Figure 21, the schematic in color illustrates an alternative RBRC adopting a HAC in an underground mine cooling. 1) The water flowing through the venturi injector behaves as a motive fluid which inducts atmospheric air down into the downcomer shaft. The potential energy of the water is converted into pressure energy transmitted to the air bubbles, compressing them. 2) A gas-water separation cyclone, or gravity separator, separates the two fluids at the bottom of the HAC downcomer, producing a pressurized air stream at 3). 4) The cool, dry compressed air is sent to receiver vessel via a service pipe, where the compressed air is stored. The water plus a small amount of dissolved air returns to atmospheric pressure at the upcast collar. Any exsolved air is vented. A circulation pump lifts water to the cooling tower sprinklers where the compression heat is rejected to atmosphere. Water in the sump of the cooling tower flows to the venturi section and inducts more air for compression.

Meanwhile the fresh ventilation air is drawn in to the downcast shaft where it may be heated as it descends, due to geothermal heating and its temperature may also

increase due to autocompression. Compressed air from the receiver passes to the turbo expander and could provide cooling as in Del Castillo's concept.
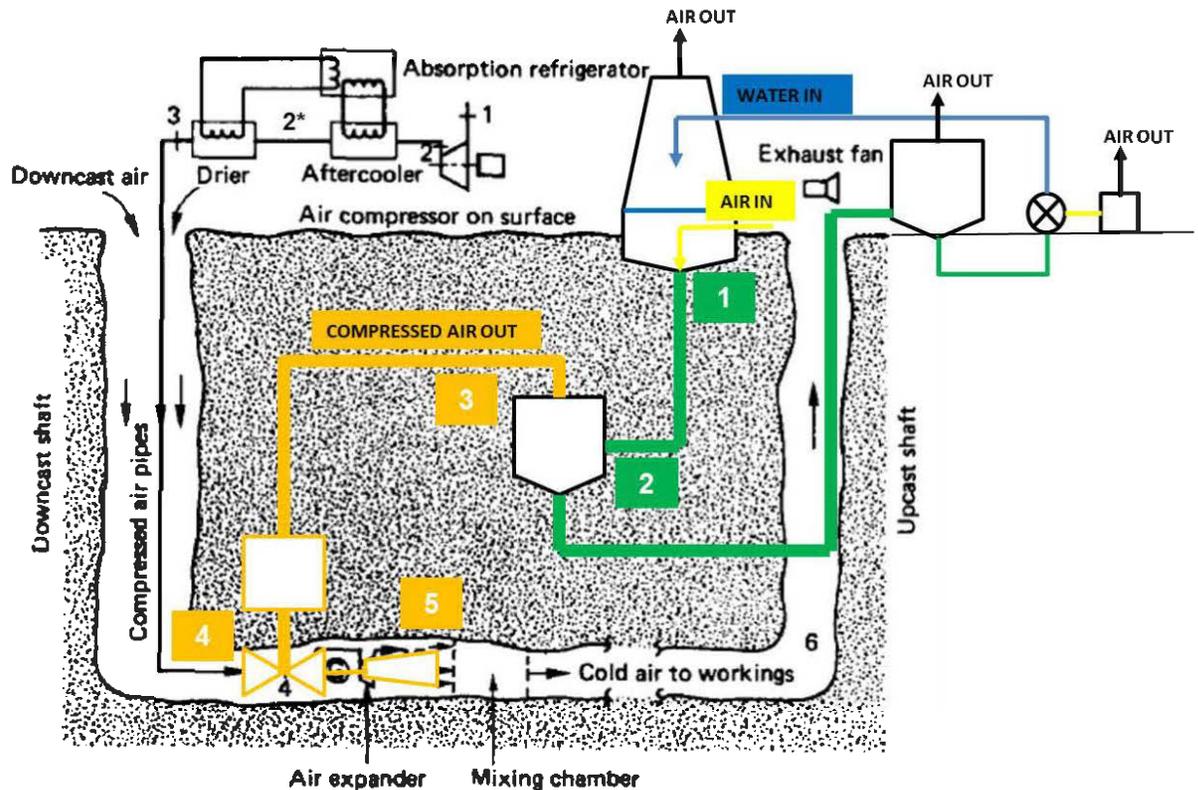
Figure 21: Modified Schematic diagram from Del Castillo (1988) including the HAC

2.6 Why does gas get cold when it is expanded?

This is an important question because it explains how the refrigeration effect is created in the turbo-expander of Del Castillo's RBRC or in the internal CD nozzle of the concept being discussed herein. The answer to the above question varies, because not all gases cool during expansion processes. Actually, a gas only gets cold during

expansion if it is the right gas. The temperature effect on gas expansion is explained by the Joule-Thompson effect and a review of this topic is presented in this section.

2.6.1 Compressibility factor and ideality of gas

Gases are governed by state equations relating the temperature, pressure and specific volume. In the case of an ideal gas,

$$Pv = RT \qquad (20)$$

where R is the specific gas constant in J/kgK, P the pressure in Pa, T the temperature in K and v is the specific volume (m^3/kg). For an ideal gas, the internal energy u, the enthalpy h vary with T ,and entropy s vary with P and T ; and the specific heat capacity depends on the temperature, $C_p(T)$. A perfect gas can be considered a particular case of an ideal gas; the difference being that for a perfect gas the specific heat capacity is not a function of temperature but is constant.

For many engineering applications, the accuracy of adopting an ideal gas approximation is reasonable. However, deviations from ideal such as the Joule-Thompson effect, critical points or condensation areas, require more general conditions and need to be analyzed with a correction called the compressibility factor z.

$$Pv = zRT \qquad (21)$$

The obvious case is when $z=1$, and so the equation above reduced to the ideal gas equation. For real gases, the behavior of the gas will depend on how close z is from 1.

The behaviour of the gases is similar when their pressures and temperatures are normalized respect to their critical values,

$$P_R = \frac{P}{P_{cr}} \tag{22}$$

$$T_R = \frac{T}{T_{cr}} \tag{23}$$

where P_R and T_R are called the 'reduced' pressure and temperature, and P_{cr} and T_{cr} are the critical pressure and temperature respectively. This normalizing is called the *corresponding states principle* (Van der Waals, 1873). The values of Z obtained by experimentation can be plotted in a $P_R - T_R$ chart to establish a generalized compressibility chart as in Figure 22.
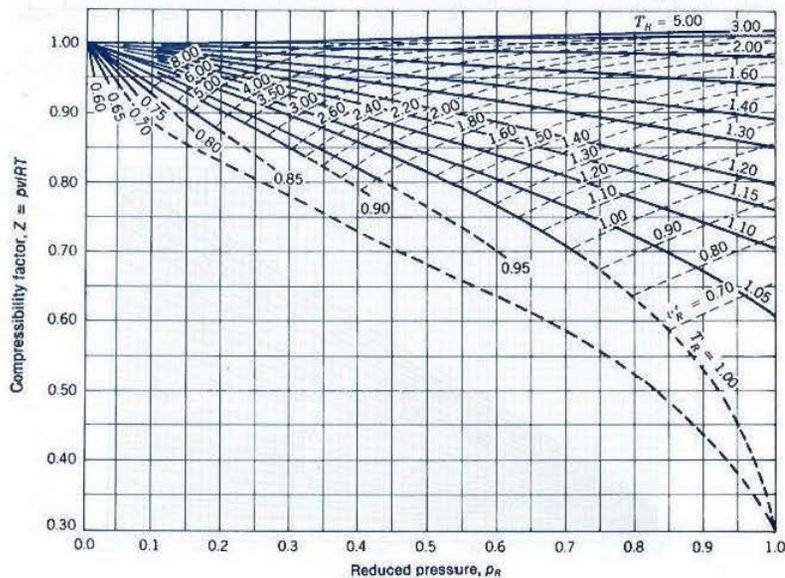
Figure 22: Generalized compressibility chart low pressure range (Obert, 1960)

According to the chart, gases act as ideal gases independently of the temperature when the pressures are low relative to the gas critical pressure($P_R \ll 1$). Secondly, ideal-gas behavior dominates at high reduced temperatures ($T_R > 2$) independently of the pressure, except when $P_R \gg 1$. Thirdly, close to the critical point there is a large deviation from ideal behavior.

In order to identify whether non ideal behavior of gas was a necessary concern in the context of compressibility, the compressibility factor was determined for extreme cases. The results of these specific investigations indicate whether or not that further work, including CFD simulations, can be performed assuming the ideal gas behavior only. With the boundary values and the NIST-REFPROP libraries (NIST, 2005), the compressibility factor z was obtained, as presented in Table 4.

Table 4: Compressibility factor Z, verification for air

Parameter	Inlet	Nozzle	Mixing	Oulet	Unit
Temperature	303.15	173.15	303.15	173.15	K
Gauge Pressure	0	0	0	0	Pa
Atmospheric pressure	140000	140000	14500	1000	Pa
Absolute Pressure	140000	140000	125000	141000	Pa
Compressibility Factor	0.99964	0.99460	0.99892	0.99963	
	0.99460	0.99964	0.99958	0.99878	

Table 4 shows the compressibility factor z is close to unity for all cases, which together defined the state domain for air for this work. The compressibility factor value is calculated with the minimum-maximum pressure and temperature. As the values for z are all close to unity, the assumption of an ideal gas is sound when necessary to apply it in this work. Notwithstanding, for much of the work reported, the libraries of REFPROP 9.1, (NIST, 2005) are used to establish values of gas state variables through the equation of state, which, by default, includes compressibility effects.

2.6.2   Joule-Thompson Effect

The so-called Joule-Thomson Effect is manifest as a change in temperature either positive or negative of a compressed gas as it suffers a rapid change in pressure, with no external work done. Such situations occur when gas passes through a nozzle (as considered in this work), a constricted throat or similar obstruction. Considering a control volume for such a throttling device, assuming there is neither any mechanical work, nor heat transfer to the surroundings (because the transit through the control volumes is so fast) and the change in potential and kinetic energy is negligible in the process, then the enthalpy is constant and the process depends upon the pressure. In order to quantify the change in temperature to be expected during the process it is necessary to find the so-called inversion temperature which depends on the pressure of the gas before expansion, for real gases.

If the temperature of a gas is above, the inversion temperature, the gas temperature increases for an expansion, if it is below, the gas temperature lowers for an expansion, since the pressure change is always negative for a gas expansion. To characterise this behaviour, the so-called Joule-Thompson coefficient can be defined according to the following equation:

$$\mu_{JT} = \left(\frac{\partial T}{\partial P} \right)_h \tag{24}$$
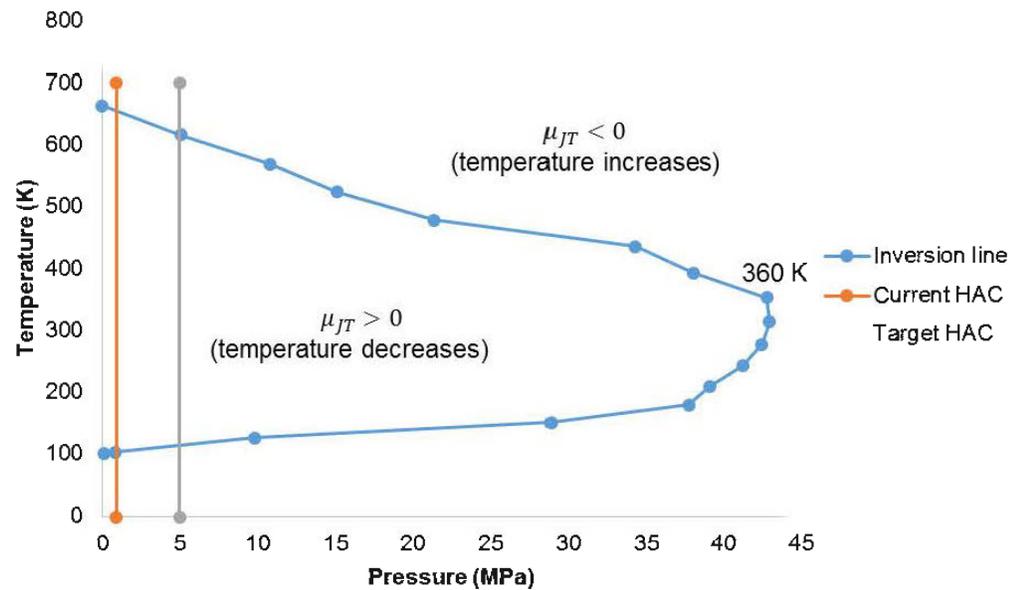
Figure 23: Joule-Thompson coefficient

Figure 23 shows the inversion line for air computed using REFPROP 9.1. The inversion line was defined on a T-P diagram as a locus of points forming an isenthalp. The pressure and temperature application ranges of this study are under 10 MPa and less than 350 K. From Figure 23, for this work, it can be concluded that any sudden change in pressure will produce a decrease of the temperature of the air.

2.7 Turbo-expander

A turboexpander is a rotating device that has the purpose of obtaining mechanical work from a gas as the gas expands. The use or not of an expansion turbine in a RBRC system for mine cooling depends upon two principal factors, its capital cost and its

efficiency. The turboexpander is a technology well known to have a high isentropic efficiency for on-design operating conditions. This performance is expressed in terms of velocity ratio, where U is the blade velocity at the impeller outside diameter, and C is the isentropic velocity which depends on the isentropic enthalpy stage. According to GE, 2008, the isentropic efficiency is between 70-90% with a guaranteed point of 87%, reproduced in Figure 24.
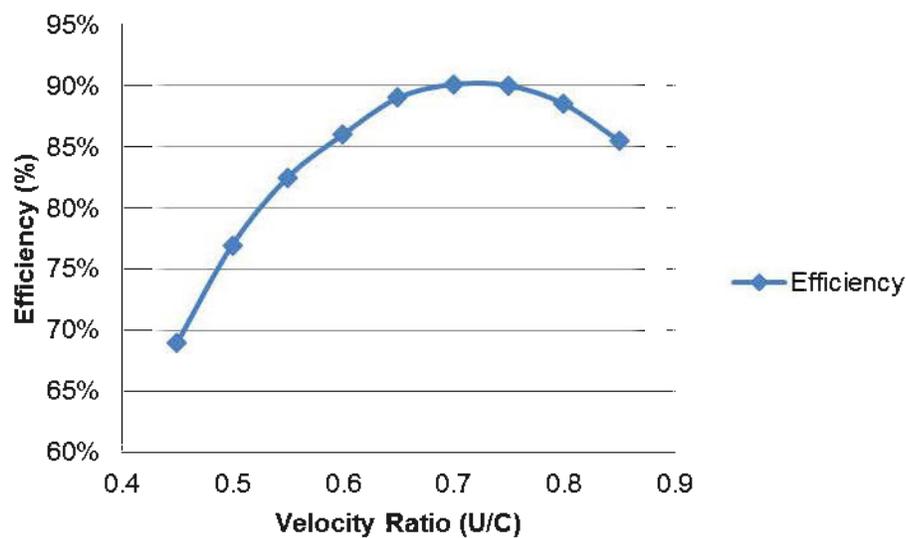
Figure 24: GE expander efficiency performance

Atlas Copco, (2012) also manufactures such equipment, and for a model XYZ 5274 the maximum isentropic efficiency is 89% at design point.
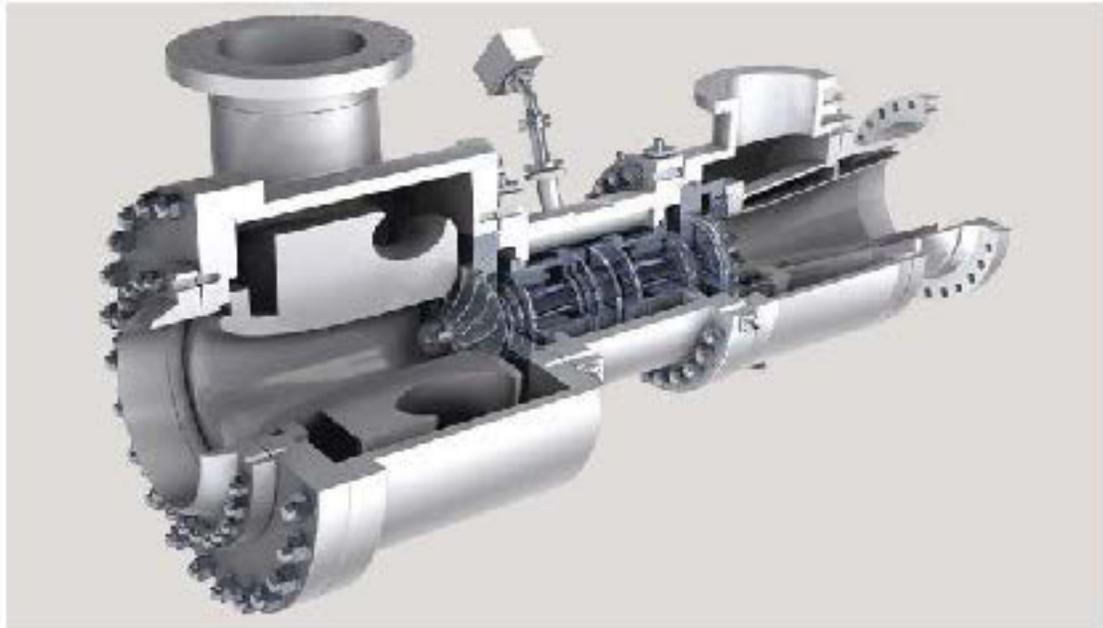
Figure 25 : Cutaway rendering of a turbo-expander (GE, 2014)

In Del Castillo's concept of cooling for deep mines using compressed air, the turbo-expander would be installed at depth in the sub-surface which may present a challenging working environment for such a machine, potentially requiring careful maintenance. Sheer et al. (1986) also suggested the use of a RBRC for mine cooling. Their main concern was the possibility of ice formation in the expansion turbine due to the very low temperatures and likelihood of high humidity. Later, Del Castillo (1988) specifically included an air drier to address this potential problem.

The main issue he identified was how much moisture a conventional turbo-expander could tolerate, which is defined by the operating and environmental conditions. In a sub-surface mine a typical relative humidity of 74% would not be unusual in ventilation air. It may be possible that this could freeze close to the turbo-expander outlet where the ventilation air meets the cool dry expanded air deliver by the expander. This was recognised as a possible safety challenge, due to the possibility of

the expander outlet becoming blocked. In the context of mine operations, if the turbo-expander is the main source of cooling, a non-planned shutdown caused by the freezing of ventilation air humidity, will stop the operation for health and safety reasons. This risk could be mitigated by using a desiccant at the ventilation air inlet; but is likely to be economically unrealistic for ventilation air mass flow rates. Modification of the turbo-expander, a complex item of machinery, would be necessary to avoid this and would represent appreciable cost too, due to its complexity and size (6m long, 3m width and 3m height). As will be explained in the next chapter, in these refrigeration systems the turbo-expander may be replaced for a simple, smaller, no maintenance, economical solution: an ejector. This represents a fourth major innovation of Del Castillo's cooling concept.

2.8 Summary

As mining depth increases, and condenser reject temperatures become higher, vapor compression refrigeration systems become expensive to operate, and alternatives need to be investigated. Del Castillo (1988) proposed the adoption of reverse Brayton refrigeration cycle as a possible alternative and suggested that it would outperform vapor compression refrigeration options as mining depths descend to 3,500 meters (presumably in South African mining operations). Brayton power and refrigeration cycles have been explained, and the distinctions between them in their performance analysis and design have been reviewed.

Importantly, in contrast with De Castillo's work, this work proposes the use of a minimum specific work input air compressor, a HAC that involves an isothermal compression process. HACs have been installed in the past, of a scale relevant to the MW-scale refrigeration system that is the design objective of this work. A second

distinction is dropping the use of a turbo-expander, a sophisticated item of equipment that is potentially ill-suited to underground mining environments, and adoption of the no-moving-parts, simple, compact ejector instead. Either option will render the enthalpy of the compressed air supplied underground to refrigeration effect of the mine air through direct contact mixing. The Joule-Thompson effect dictates that for air, which is the refrigerant and coolant of concern, low temperatures will result during expansion, over the range of temperatures and pressures anticipated.

It is important to recognize that although fundamental improvements to Del Castillo's RBRC concept are proposed herein, the thermodynamic cycle governing performance remains the RBRC. The improvements should be expected to lead to lower costs, and consequently the motivation for consideration of the RBRC framework for mine air refrigeration is clear, to establish whether it is now suitable for air refrigeration at mining depths shallower than 3,500m

CHAPTER **3**

REVIEW OF EJECTOR DESIGN AND PERFORMANCE

3.1 Introduction

A key proposal of this work will the replacement of a turbo-expander with an ejector as the expansion device in the RBRC. The ejector has the potential to be a simpler, smaller, lower maintenance and potentially more economical solution and a third key variation step on the RBRC concept set out by Del Castillo. Demonstrating and quantifying the efficacy and cost effectiveness of this proposal, is the main topic of subsequent material in this thesis. By way of demonstrating motivation, this chapter firstly articulates the design concept considered in this thesis, then the basic derivation of the equations governing the flow in these systems is set out. Next a fundamental thermodynamic functional comparison between a turbo-expander and a nozzle is presented to demonstrate the theoretical viability of the concept, and then a detailed review of ejector design and performance is presented.

Introducing a machine like a cryogenic turboexpander at the sub-surface of a mine, could produce significance maintenance issues. It is known to be a reliable machine but has many components and some of these are specialized. The experience dealing with this sort of system with humid air presents a potential icing issue (Del Castillo, 1988). Perhaps this is the reason why this type of refrigeration system hasn't been exploited in the mining industry until this point.

The vision of this work for the expansion device in Del Castillo's system is an ejector. This is a duct where high speed, expanded and cooled, compressed air is 'fired' into a narrow throat that inducts ventilation due to a venturi effect. When the two airstreams mix, the ventilation air is cooled. The ejector is a convergent-divergent (CD)

nozzle inside another CD nozzle (Figure 26). The internal nozzle converts high pressure, high enthalpy compressed air into low pressure, high speed and very cool air. As the internal nozzle expands the air, this is the reason why it gets cold. When it is directed into the throat of the larger CD nozzle, since the air has high speed a low pressure zone develops due to the venturi effect and the ventilation air is inducted into the system. Mixed air passes to a diffuser section, which is a divergent duct, which causes the mixed air to pressurize
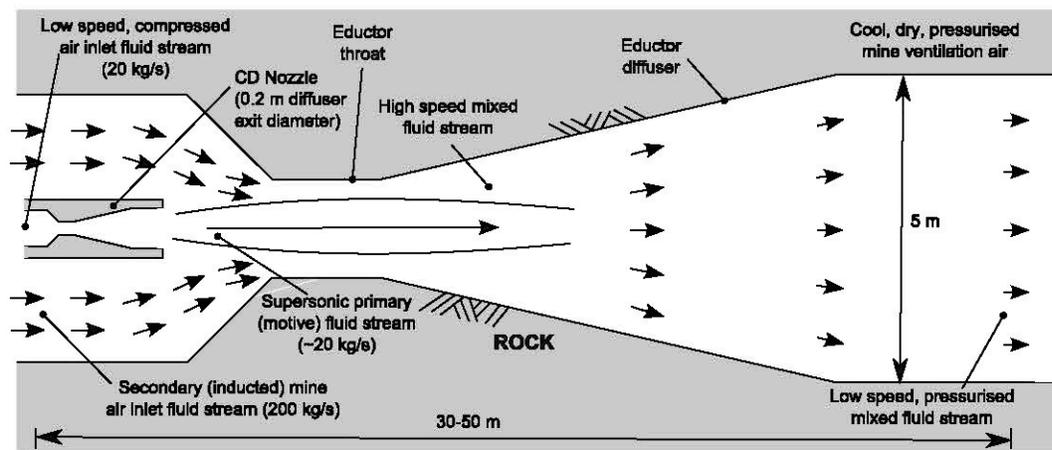
Figure 26: CD nozzle inside CD nozzle (Millar et al., 2016)

Overall, there is a pressure rise between the inlet for the ventilation air, and the outlet. For the reasons stated earlier, the mine air would be cooled and dehumidified in the eductor, and a pressure rise in the direction of the flow means that furthermore: the ejector may behave like a fan.

Many of the literature sources, e.g. (Zhu et al., 2009) (Chen et al., 2014) (Wu et al., 2014), define the performance of an ejector in terms of the *mass flow ratio or the entrainment ratio:* the ratio between the secondary and primary mass flow rates. 1D compressible flow theory, based on principles of mass, momentum and energy

conservation coupled with an ideal gas equation of state can be used to predict the performance of ejectors with reasonable accuracy.

From the point of view of the RBRC scheme, an ejector would be required to i) expand the compressed air to provide a high speed cool, dry air stream forming the ejector's driving, primary flow, and ii) cause the high speed expanded air stream and the ventilation air to mix thoroughly, so that the latter is cooled down, providing refrigeration effect. The principal elements of an ejector are:

- The primary or motive nozzle, which is normally a convergent-divergent nozzle. The primary is created by accelerating and expanding high pressure, low velocity air through the nozzle throat to supersonic speeds and to the nozzle back pressure.

- The suction chamber, where the high velocity primary at the motive nozzle exit issues, develops a Bernoulli-like low pressure zone and thereby entrains the secondary fluid (the mine ventilation air) to the mixing chamber.

- The mixing chamber; at the beginning of the chamber both fluids start to mix at constant pressure. At really high speeds with a high pressure zone a so-called shock train may occurs at the end of this area increasing the pressure.

- The divergent diffuser, where kinetic energy of the mixed primary and secondary fluid streams is recovered to pressure energy.

Since the highest ejector efficiency is attained when operating under critical conditions, both primary and secondary flows are choked, and the entrainment ratio is constant. In this specific case, the secondary air flow may not be choked.
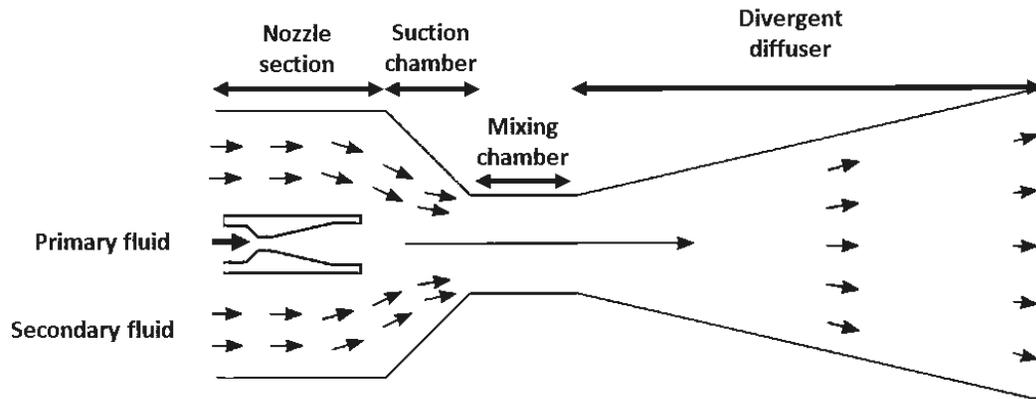
Figure 27: Schematic diagram of ejector, illustrating terminology adopted for different parts of the system.

Overall, the ejector has the appearance of convergent-divergent nozzle inside a convergent-divergent nozzle.

3.2 General governing equations

From the Langrangian perspective these laws are easy to apply, but not in practical applications, however there is a tool for that: the Reynolds Transport Theorem (RTT), which convert the Langrangian perspective, (system) to an Eulerian perspective (control volume). This RTT is described by the equation.

$$\frac{D}{Dt}\left[\int_{V_{sys}} \beta\rho dV\right] = \frac{d}{dt}\left[\int_{CV} \beta\rho dV\right] + \int_{CS} \beta(\rho u_{rel} dA) \tag{25}$$

Where $\frac{D}{Dt}$ is the time rate of change, a Lagrangian derivative following the system.
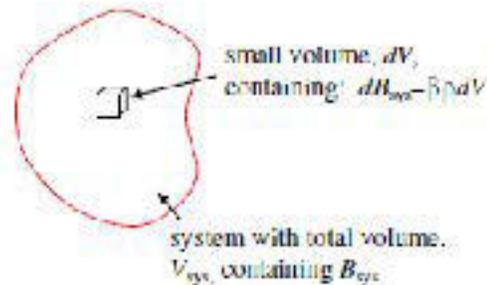
Figure 28: Control volume (Wassgren, 2010)

B is any extensive property (proportional to mass), β is amount of B per unit mass, ρ is density, V is volume, $u_{rel}dA$ is the volumetric flowrate through the control volume surface, CS and CV denotes the control surface and control volume.
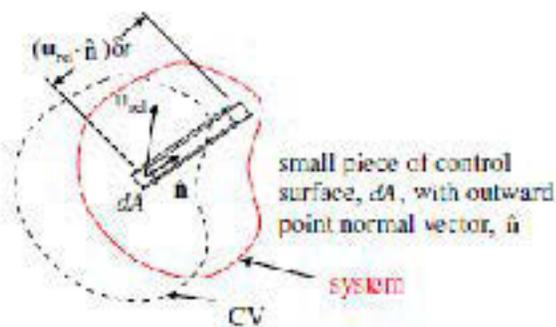
Figure 29: Small element of control surface of the control volume (Wassgren, 2010)

3.2.1 *Conservation of mass*

For the purpose of conservation mass in a system, the mass must remain constant, that is, with B being mass and with β being mass per unit mass (i.e. unity):

$$\frac{D}{Dt}\left[\int_{V_{sys}} \rho dV\right] = 0 \tag{26}$$

Applying this to the RTT, becomes:

$$\frac{d}{dt}\int_{CV} \rho dV + \int_{CS} (\rho u_{rel} dA) = 0 \tag{27}$$

Assuming the mass is constant in the CV, this reduces to:

$$\int_{CS} (\rho u_{rel} dA) = 0 \tag{28}$$

For the a volume with one inlet, labelled 1, and one outlet, labelled 2, with a single fluid, becomes:

$$\int_{CS_1} (\rho_1 V_1 \vec{n_1} \, dA) + \int_{CS_2} (\rho_2 V_2 \vec{n_2} \, dA) = 0 \tag{29}$$

After setting the signs of the outward normal vectors, becomes:

$$-\rho_1 V_1 A_1 + \rho_2 V_2 A_2 = 0 \tag{30}$$

and thus the conservation of mass is determine for control volume:

$$\dot{m}_1 = \rho_1 V_1 A_1 = \rho_2 V_2 A_2 = \dot{m}_2 \tag{31}$$

$\dot{m}_1$ and $\dot{m}_2$ are the mass flow rate.

3.2.2 Conservation of Linear momentum

Applying to the control volume to the second law of Newton, the sum of forces acting on the system is equal to the rate of change of the linear momentum of the system:

$$\frac{D}{Dt}\left[\int_{V_{sys}} u_{XYZ}\rho dV\right] = \sum F_{on\ system} \tag{32}$$

where u_{XYZ} is the velocity of an elemental portion of the fluid in the system relative to an inertial reference framework XYZ. $\sum F_{on\ system}$ are the total forces acting on the system comprising two types: those acting on the portion of the fluid called body forces, $F_{body\ on\ CV}$, and those acting at the surface of the control volume, called surface forces, $F_{surface\ on\ CV}$.

Using the RTT for a CV, the equation becomes,

$$\frac{d}{dt}\int_{CV} u_{XYZ}\rho dV + \int_{CS} u_{XYZ}(\rho u_{rel}dA) = F_{body\ on\ CV} + F_{surface\ on\ CV} \tag{33}$$
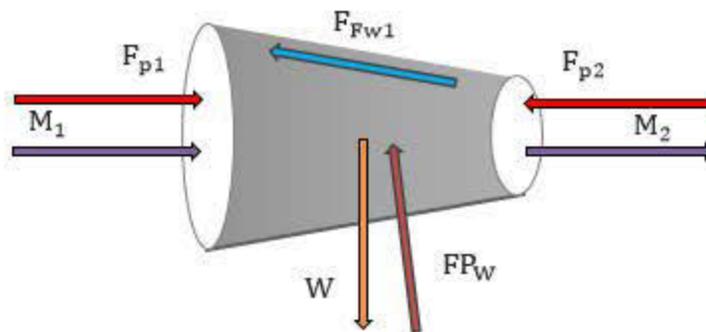
Figure 30: Vector Forces, Momentum and Weight

Knowing that the momentum vector has the same direction as the velocity vector and summing the forces acting on the control volume, the resulting expression is:

$$M_1 + M_2 = F_{P_1} + F_{P_2} + W + FP_W + F_{Fw1} \tag{34}$$

M_1, M_2 being the momenta, F_{P_1}, F_{P_2} being the pressure forces, W being the weigh, FP_W being the pressure force on the wall, F_{Fw1} being the friction force on the internal wall.

3.2.3 Conservation of energy

A requirement for conservation of energy in a system is a statement of the first law of thermodynamics: the heat added to the system plus the work done on the system is equal to the augmentation in total energy of the system.

$$E_{of\ system} = Q_{into\ system} + W_{on\ system} \tag{35}$$

For a CV,

$$\frac{D}{Dt}\left[\int_{V_{sys}} e\rho dV\right] = Q_{into\ system} + W_{on\ system} \tag{36}$$

Applying this to the RTT, the conservation of energy requirement becomes:

$$\frac{d}{dt}\int_{CV} e\rho dV + \int_{CS} e(\rho u_{rel} dA) = Q_{into} + W_{on} \tag{37}$$

where

$$e = u + \frac{1}{2}V^2 + gz \tag{38}$$

u is the internal energy, $\frac{1}{2}V^2$ kinetic energy, gz potential energy. The rate of work can be expanded as follows

$$W_{on} = W_{pressure,on} + W_{shaft,on} + W_{other,on} \tag{39}$$

Since the rate of pressure work can be expressed over the entire control volume,

$$W_{pressure,on} = \int_{CS} -p(u_{rel}dA) \tag{40}$$

the final expression is:

$$(h + \frac{1}{2}V^2 + gz)_1 = (h + \frac{1}{2}V^2 + gz)_2 \tag{41}$$

The three key equations governing flow in ducts developed in this section are presented together below. When applied to ejector systems, these equations can be applied to the primary and secondary flows simultaneously.

In an ejector, these equations can be written for primary and secondary flows.

$$\dot{m}_1 = \rho_1 V_1 A_1 = \rho_2 V_2 A_2 = \dot{m}_2 \tag{42}$$

$$M_1 + M_2 = F_{P_1} + F_{P_2} + W + FP_W + F_{Fw1} \tag{43}$$

$$(h + \frac{1}{2}V^2 + gz)_1 = (h + \frac{1}{2}V^2 + gz)_2 \tag{44}$$

For ejector analysis, these equations are applied with additional information on boundary and initial conditions, to produce estimates of so-called 'Output values'.

3.3 Review of the design and performance of ejectors

A complete analysis with the experimental verification is described by Huang et al., 1999.
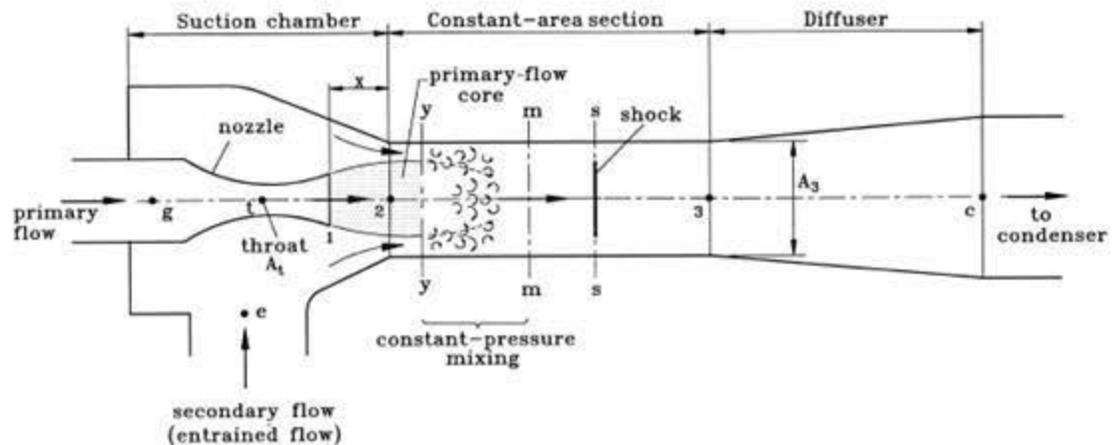
Figure 31: Schematic diagram of ejector performance (Huang et al., 1999)

An important simplification, appropriate in the current work, is an assumption of single phase flow (no phase change). The various mathematical formulations are usefully reviewed by He et al., (2009). Essentially all formulations for ejector performance reviewed by this author followed a similar theme adopting one or more of the conservation equations presented in the previous section, and applying particular constraints, as appropriate, to solve for performance variables. For example, Huang et al., (1999) applied the constraint that the pressures of both primary and secondary flows had to be the same between section X-X and section Y-Y (Figure 31) and that the mixing nozzle had a constant area throat section in between station 2 and station 3.

3.3.1   Thermodynamic model of ejector's design

Such ideas for the analysis of ejector performance were first set out by Keenan and Neumann, (1942) who established the necessary equations for the model. Later, two distinct theoretical methods to solve the momentum conservation equation were introduced by Keenan et al., (1950) which showed that the constant-pressure mixing (CPM) ejector gives greater performance than the constant-area mixing (CAM) ejector. From that point on the majority of mathematical models for ejectors used CPM.

3.3.2   CPM Model

The author has identified around fifteen studies concerning the single-phase flow in ejectors. The majority of them adopt the CPM because CPM is closer to the physical reality. After Keenan et al., (1950) further studies were done to analyze the mixing of fluids within ejectors. Munday and Bagster, (1977) assumed a throat at the end of the suction chamber which would entrain the fluid formed there. Later Eames et al., (1995), took into account the irreversibility through friction refining Keenan's model. Then Aly et al., (1999), drew upon two models: i) from Munday and Bagster, (1977) and ii) Eames et al., (1995) but did not take into account the choking of the secondary fluid. Subsequently, Huang et al., (1999) considered the choking effect using Eames et al., (1995) equations, Munday and Bagster's, (1977) theory, and gas dynamic relations for performance ejector in critical mode operation.

3.4 Expected performance

In addition to the proceeding, performance prediction still requires the isentropic efficiency which is defined as:

$$\eta_{ejector} = \frac{actual}{isentropic} = \frac{h_{inlet} - h_{outlet}}{h_{inlet} - h_{outlet,isentropic}} \qquad (45)$$

where h_{inlet} is the inlet enthalpy, h_{outlet} is the outlet enthalpy and $h_{outlet,isentropic}$ is the outlet enthalpy for an isentropic process. These enthalpies can be obtained for the nozzle, suction chamber, mixing area and diffuser.

In Keenan and Neumann (1942) their first approach the did not include a diffuser section and the mixing chamber was of a constant sectional area. Friction and heat losses and other irreversibilities were also excluded. In the subsequent approach, Keenan et al. (1950) using air as a working fluid, included a diffuser and a mixing chamber that provided constant-pressure mixing but not the friction and heat losses. In that study, the motive nozzle and suction nozzle had efficiency defined as 1.

Almost 50 years later, Eames et al. (1995), modified Keenan et al.'s (1950) analysis, to include the irreversibilities of the motive nozzle, the mixing chamber and the diffuser, obtaining isentropic efficiencies of 0.85, 0.95 and 0.85 respectively for each when steam was the motive and secondary fluid. In the same year Domanski (1995) using the refrigerant R-134a determined 0.85 as primary motive nozzle efficiency and 0.7 for diffuser efficiencies with a single-phase gas. After the Montreal Protocol for climate change, CFCs in all refrigeration systems were replaced. Sun (1996) uses ejectors in absorption refrigeration machines with Li-Br-H_2O and H_2O-NH_3 systems, obtaining 0.85 for nozzle and diffuser efficiencies. Sun and Eames (1996) achieved similar values with HCFC-123. El-Dessouky et al. (2002) undertook

a detailed review of steam ejectors; Between the seven authors reviewed, including Eames et al. (1995), the efficiencies vary from 0.7-1 for nozzles, 0.65-1 for diffusers and 0.8-0.95 for the mixing chamber. One year later, Alexis and Rogdakis (2003), reporting on a steam ejector refrigeration study, attained 0.7 in the motive nozzle and 0.8 in the suction nozzle and diffuser. Later yet, Varga et al. (2009) undertook a numerical assessment of steam ejector efficiencies using CFD, following previous studies, seven of them using water and 10 using refrigerants, and it was found that all the efficiencies depend upon the range of operating conditions applied in this work, except for the nozzle efficiency.

Liu and Groll (2013), in their study about ejector efficiencies in refrigeration cycles, considered CO_2 as the ejector fluid using eight prior cases, discovering that both nozzles efficiencies have some dependence on their nozzle throat diameters. The mixing efficiency depends on the motive nozzle position (i.e. the value of x in Figure 30) and suction nozzle conditions including room temperature, due to critical conditions being achieved inside the nozzle throat (e.g. choking). In Table 5, results of all studies considered in this work are tabulated, where η_m is the efficiency of the motive nozzle, η_s is the efficiency of the suction chamber, η_{mix} is the efficiency of the mixing area and η_d is the efficiency of the diffuser.

Table 5: Review of previous studies about ejector efficiencies

Reference	η_m	η_s	η_{mix}	η_d
(Keenan et al., 1950)	1	1		
(Tyagi and Murty, 1985)	0.9			0.9
(Eames et al., 1995)	0.85		0.95	0.85
(P. A. Domanski, 1995)	0.85-0.9	0.85-0.9		0.7
(Sun, 1996)	0.85	0.85		0.85
(Grazzini and Mariani, 1998)	0.9		1	0.85
(Aly et al., 1999)	0.9		0.95	0.9
(Huang and Chang, 1999)		0.85		
(Huang et al., 1999)	0.95	0.85	0.8-0.84	
(Sun, 1999)	0.85			0.85
(Rogdakis and Alexis, 2000)	0.8		0.8	0.8
(Cizungu et al., 2001)	0.95	0.95		0.85
(El-Dessouky et al., 2002)	1		1	1
(Alexis and Rogdakis, 2003)	0.7			0.8
(Elbel and Hrnjak, 2004)	0.9	0.9		0.9
(Selvaraju and Mani, 2004)	0.95	0.95		0.85
(Li and Groll, 2005)	0.9	0.9		0.8
(Yapici and Ersoy, 2005)	0.85	0.85		0.85
(Ksayer and Clodic, 2006)	0.85	0.85		0.75
(Yu et al., 2006)	0.85		0.95	0.85
(Deng et al., 2007)	0.7	0.7		0.8
(Godefroy et al., 2007)	0.8	0.95	0.935	0.8
(Ksayer, 2007)	0.95	1	0.9-0.98	1
(Yu and Li, 2007)	0.9		0.85	0.85
(Yu et al., 2007)	0.85		0.95	0.85
(Zhu et al., 2007)	0.95-0.9	0.85		
(Elbel and Hrnjak, 2008)	0.8	0.8		0.8
(Sarkar, 2008)	0.8	0.8		0.75
(Yu et al., 2008)	0.9		0.85	0.85
(Sun and Ma, 2011)	0.9	0.9		0.8
(Manjili and Yavari, 2012)	0.7	0.7	0.95	0.8
(Vereda et al., 2012)	0.85	0.85	0.9	0.8

The majority of the literature about ejector performance appears to focus on the efficiency of each ejector part: nozzles, mixing chamber and diffuser, and not on the overall ejector efficiency. One exception is Kohler et al. (2007) who define the efficiency of an ejector as a single component inside a cooling cycle, for the first time. The simplicity of his approach is that only external parameters are measured, based on the energy balance of the ejector and the efficiencies of compressor and turbine.

$$\eta_e = \eta_C \eta_T = \frac{\dot{m}_s}{\dot{m}_m} \frac{(h'_{s,isentropic} - h_s)}{(h_m - h'_{m,isentropic})} \tag{46}$$

where η_C is the efficiency of the compressor, η_T is the efficiency of the turbine, $\dot{m}_s$ is the mass of flow of the secondary fluid or evaporator, $\dot{m}_m$ is the mass of flow of the motive fluid or generator, $h'_{s,isentropic}$ is the isentropic suction nozzle enthalpy which depends on the inlet suction entropy and outlet pressure, $h'_{m,isentropic}$ is the isentropic motive nozzle enthalpy which depends on the inlet motive entropy and outlet pressure.

Another approach to the overall ejector efficiency is from Elbel and Hrnjak (2008) ,using a different derivation method based on expansion work rate recovered but the final result is the same as Kohler et al. (2007). The next approach to the overall ejector efficiency is from McGovern et al. (2012), where efficiencies are defined comparing reversible and real processes (Reversible entrainment ratio efficiency, Reversible discharge pressure efficiency, Turbine-compressor efficiency, Compression efficiency) and an exergetic efficiency as well. This work allows one to compare the efficiency of isentropic and adiabatic turbine-compressors coupled to an ejector, for the same exit pressure.

$$\eta_{TER} = \frac{ER}{TER} \qquad (47)$$

where ER is the entrainment ratio in a real ejector and TER is the Turbine-Compressor entrainment ratio.

3.5 Design geometry comparison

The goal of this section is maximize the performance of the ejector. In the last section, the expected performance according to the literature review was analysed. This showed that the performance may vary according the specific operating conditions and the geometry designed.

Following Huang et al., (1999), an excel document incorporating NIST, (2005) for state variable estimation was developed. There are several variables unknown; hence it is necessary to assume some values in order to determine the outlet temperature from the diffuser. The use of at least five independent variables is needed, such as, temperature and pressure of both fluids, and the critical pressure. Besides the assumption of the efficiency, in each flow, the mixing and the exit area of the nozzle is required as well. In addition to the outlet temperature of the diffuser, which is determined from the outlet pressure of the diffuser developed in the model, the primary flow, the entrained flow, the entrainment ratio, the cross sectional area of the constant-area section and the area ratio are outputs of the study.

3.5.1 Comparison in design

Keenan et al., (1950) are the first to point out the importance of keeping a distance between the motive nozzle exit and the mixing chamber inlet on overall ejector performance. Later, Eames et al., (1995), noticed the impact of the outlet pressure in the final cooling capacity of a fixed geometry ejector. Huang et al., (1999) demonstrated that the best performance for the ejector, for their operational conditions, was when the ratio between the distances of the exit of the motive nozzle to the inlet of the mixing chamber divided by the diameter of the mixing chamber were equal to 1.5. Ouzzane and Aidoun, (2003), also showed this length affects on the mixing process and how the diameter affects the exit pressure and entrainment ratios. Zhu et al., (2007), proposed a model to predict the ejector performance improving the 1D models design. Sriveerakul et al., (2007), used CFD to foresee the behavior of critical back pressure and entrainment ratio for the ejector design, improving its accuracy. Zhu et al., (2009), studied two parameters, the motive nozzle exit position (NXP) ranging over 1.7-3.4 times the length of the mixing chamber diameter inlet with the mixing angle ranging between 1.45-4.2°. Varga et al., (2009a) used CFD to discover an optimum value for the ratio of motive nozzle throat and mixing chamber cross section to improve the entrainment ratio. Varga et al., (2009b), found that the location of the motive nozzle exit affects the critical back pressure and entrainment ratio. Yang et al., (2012) evaluated the mixing process with different nozzle structures. Kumar and Ooi, (2014), showed only modest sensitivity of ejector performance on the ratio length-diameter of the mixing chamber. Wu et al., (2014), found that for a fixed length of the mixing chamber, there is an optimal convergence angle. Zhu and Jiang, (2014), showed that the entrainment ratio performance increases when the shock wave wavelength is reduced.

In summary of the above, Table 6 shows how several geometric constraints may affect the performance of an ejector, such as the position of the nozzle, the operation conditions, diameter and length of each component. As it can see on the table, the

optimum geometry depends on the operating conditions and specific function of the ejector The purpose of this table, it is to show how complicated is the design of an ejector, so that the existing literature can only be used as a guide for new applications. Other authors such as Aphornratana and Eames, (1997); Yadav and Patwardhan, (2008), worked on the ejector geometry design and performance.

Table 6: Design geometry comparison

Parameter	Symbol	ASHRAE	ESDU	Huang et al	Ouzzane et Aidoun	Zhu et Li	Varga et al	Zhu et al	Sriveerakul	Liu et Groll	Kumar et Ooi	Wu et al
Nozzle Diameter	Dn											
Mixing Diameter	Dm											
Extra Diameter	De											
Throat Diameter	Dt											
Suction Diameter	Ds											
Nozzle Length	NXP			NXP/Dm =1.5	0.5< NXP/Dm <1.5				NXP = 1.7-3.4*Dm	NXP = 1.5*Dm		
Throat Length	Lt											
Suction Length	Ls	6-10*Dt										
Mixing Length	Lm		2-4*Dm						1-6*Dm		Lm/Dm = 10	17< Lm/Dm <23
Diffuser Length	Ld	4-12*Dt										
Extra Length	Le											
Suction Angle	Alpha s	2-10°	0.3*Dt or 24°									
Diffuser Angle	Alpha d	5-12°	3-4° no >7°									
Area ratio						Dm/Dt = 2.2-2.9	(Dm/Dt)^2 = 13-27					

3.6 Comparison of thermodynamic conditions for a turbo-expander and ejector

In this work, the fundamental premise is that the turbo-expander set out in Del Castillo's concept may be replaced by an ejector, motivated, as previously explained, on the grounds of greater simplicity and lower cost. In Del Castillo's concept, the turbo-compressor expands and cools the compressed air. In this work, compressed air expansion and cooling are achieved by the motive nozzle of the ejector.
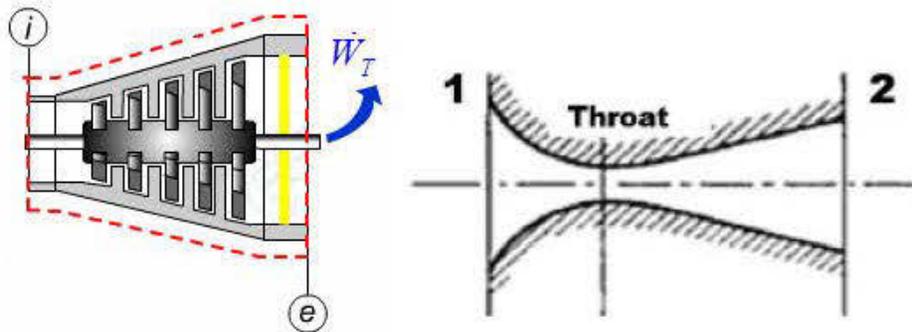
Figure 32: Turbo-expander (left) and Ejector (right) schematic.

Both of these competing options aim to do similar things: to expand compressed air and render it cold, so that when it mixes with ventilation air, a refrigerating effect is realized. In doing this, each system would operate over the same pressure difference. In the case of the turbo-expander, useful shaft work is recovered as the compressed air is let down. In the nozzle, instead the enthalpy drop is used to accelerate the speed of the air.

Starting with the steady flow energy equation:

$$\frac{(V_1{}^2 - V_2{}^2)}{2} + g(Z_1 - Z_2) + W_{12} = h_2 - h_1 - q_{12} \qquad (48)$$

and then assuming adiabatic, level conditions:

$$\frac{(V_1{}^2 - V_2{}^2)}{2} + W_{12} = h_2 - h_1 \qquad (49)$$

If the air is assumed a perfect gas with constant heat capacity, then:

$$\frac{(V_1{}^2 - V_2{}^2)}{2} + W_{12} = C_p(T_2 - T_1) \qquad (50)$$

To achieve a given cooling effect: $T_2 \ll T_1$, work in the process, W_{12} must be abstracted from the system, or, if no work is removed, the velocity of the air must accelerate so that $V_2 \gg V_1$. In an alternative interpretation, if air is to be cooled with a turbo-expander, the turbo-expander exit velocity must be minimized (through choice of a large cross sectional area for the flow at exit) and the efficiency of the turbo-expander must be maximized. If air is to be cooled with a nozzle, where no work is abstracted at all, the exit velocity of the air must be maximized.

For a given mass flow of air, $\dot{m}$, the useful mechanical work delivered by the turbo-expander is:

$$W_{12} = (h_2 - h_1) - \frac{(V_1{}^2 - V_2{}^2)}{2} \qquad (51)$$

For a turbine $w_{12} < 0$, so $h_2 < h_1$ and the greater the exit velocity, V_2, the lower the extracted power. Thus the exit cross sectional area is selected so that $V_2 \rightarrow 0$, that is, the exit area is larger than the inlet area to account for the reduction in air density due to the depressurization. There is a maximum, ideal, amount of work that can be extracted from the depressurizing air and this is:

$$W_{12,max} = (h_{2,isen} - h_1) - \frac{(V_1{}^2)}{2} \tag{52}$$

The extent to which the actual process deviates from this ideal is characterized by the isentropic efficiency:

$$\eta_{isen} = \frac{W_{12}}{W_{12,max}} = \frac{(h_2 - h_1) - \frac{(V_1{}^2 - V_2{}^2)}{2}}{(h_{2,isen} - h_1) - \frac{(V_1{}^2)}{2}} \tag{53}$$

which, for small inlet and outlet velocities, simplifies to:

$$\eta_{isen} = \frac{(h_2 - h_1)}{(h_{2,isen} - h_1)} = \frac{(T_2 - T_1)}{(T_{2,isen} - T_1)} \tag{54}$$

To illustrate the formulation, three cases of turbo-expander operating condition are considered (which are also illustrated in Figure 33.

Case 1: For the case of a 20 kg/s mass flow of air at 8 bar (abs) and 30°C entering a turbo-expander via a 0.5 m diameter pipe and adiabatically exhausting to 1.15 bar (abs), the lowest (isentropic) temperature at turbo-expander exit is: -100.9°C, when the velocity at input is 11.04 m/s and that at outlet is 10.90 m/s (for an outlet area 4 times that of the inlet). If the turbo-expander has an isentropic efficiency of 85%, then, for the same inlet conditions and geometry, the exit temperature expected is -81.5°C and the exit velocity is 12.14 m/s.

Case 2: It is interesting to note what happens in the below example, if the isentropic efficiency of the turbo-expander is set to zero, corresponding to the case where the turbo-expander delivers nil shaft work, equivalent to a 'no-load' condition on the generator to which the shaft may be connected. In this instance, the exit temperature of the air would be 28.4°C and the exit velocity would be 19.15 m/s.
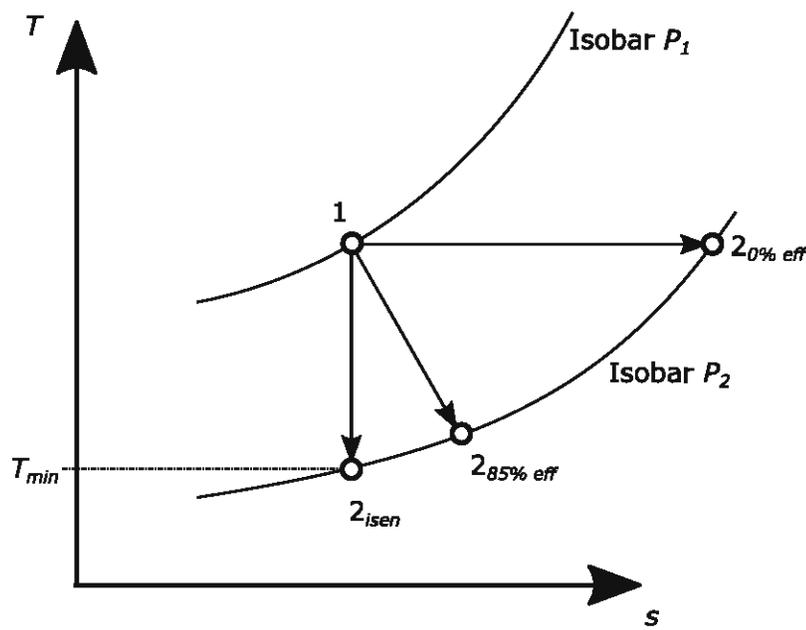
Figure 33: T-S diagram for ideal and irreversible turbo-expander processes

Case 3: To produce a lower temperature of air under the no-load condition, the air at the exit of the turbo-expander could be throttled with a valve by reducing the area of the exhaust port. Adjusting the exit flow area to 14.22% of the inlet area, the temperature at the exit would be -81.5°C and the exit velocity would be 341.49 m/s. In effect, under this condition, the throttled, no-load, turbo-expander behaves as a

convergent duct, or a nozzle, that has traded the work for exit air velocity, to bring about the same state of air at exit.

If, instead of a turbo-expander, a nozzle had been used to bring about the state of the air in Case 3, then the ideal process considered for the nozzle is also isentropic, and the extent of deviation of the actual process due to irreversibility is measured with an isentropic efficiency:

$$\eta_{isen,nozzle} = \frac{(h_2 - h_1)}{(h_{2,isen} - h_1)} = \frac{(T_2 - T_1)}{(T_{2,isen} - T_1)} \qquad (55)$$

that is identical in the manner it is assessed to the manner in which the turbo-expander isentropic efficiency is assessed. Thus it may be said that if Case 3 had been brought about by a nozzle, then the nozzle's isentropic efficiency was 85% and Figure 33 identically applies to a nozzle.

Looking back at Table 5 of Section 3.6, it can be seen that a value of 85% for the isentropic efficiency in the motive nozzle of an eductor, is not at all unreasonable. Consequently, it must be concluded that replacement of the turbo-expander with a nozzle in Del Castillo's concept will in no way diminish the low exit air temperatures that may be expected, providing nozzle irreversibilities can be minimized.

3.7 Discussion

In this chapter, the different equations, pertinent assumptions and isentropic relations have been presented to explain the flow inside the ejector. Performance of turbo-expanders and convergent-divergent nozzles are characterized by isentropic efficiencies that indicate the deviation that the actual processes in these devices assume in comparison to an isentropic ideal. In the turbo-expander, work must be abstracted from the flow to cause the outlet air to have substantially lower temperature. In the motive nozzle of an ejector/eductor, no work is abstracted, but the exit air velocity must be high, approaching or exceeding sonic velocity, to achieve similar temperature drops. There can be little doubt that the necessary cold air temperatures can be practically achieved with a properly designed motive nozzle of the ejector. The resulting high speed jet means that mechanical energy is retained within the velocity of the flow, rather than being extracted as is the case with the turbo-expander.

The review in this chapter has shown that a low pressure zone develops in front of and within the mixing throat of the ejector. The mixing process itself implies momentum transfer from the motive flow to the secondary flow, and the induced low pressure causes the secondary flow to be inducted into the ejector. The diffuser section of the ejector causes the mixed, cooled, flow to decelerate so that static pressure is recovered from dynamic pressure at the ejector exit. The pressure at exit can be higher than at the secondary inlet, meaning that for the latter system, the ejector behaves as a pump. In short, with the ejector system, it is not the case that no work is abstracted from the flow (as is the case with the turbo-expander). Rather, instead of being removed during the stage where cold temperatures are developed, the flow work imparted to the mixture from the motive flow in the mixing section is converted to pressure in the diffuser that can be used to overcome resistance in the mine workings. In a mine ventilation system, regenerated electricity is only really required indirectly to power electrically driven fans. But what is required is flow work of the mine air so that it can

overcome the mine frictional resistance, and it appears that the ejector unit delivers this.

In order to guide a search for optimum ejector performance, through literature review, a comparison in design of various ejectors designs and methods of performance characterization was undertaken and the results of this were presented in this Chapter. Straightforward comparison revealed complexity of ejector design and how several geometric constraints may affect the performance, example being: the position of the nozzle, the operating conditions, and the diameter and length of each component. Subsequent Chapters use the understanding gained and the design norms assembled and reported in this Chapter to guide computational fluid dynamics simulations of the ejector/eductor system for operating conditions and scales relevant to mine ventilation air cooling and flow promotion. However in the Chapter immediately following, a more detailed analysis of the ejector motive nozzle is presented first.

.

CHAPTER 4

DESIGN OF A MOTIVE NOZZLE

4.1 Introduction

A nozzle is a smooth passage with varying cross-sectional area where the velocity increases due to a drop in pressure. The usual applications of nozzle analysis are in rocket propulsion, gas and steam turbines and jet engines. Generally, there are two types of nozzle, those which are convergent only, and those which are convergent-divergent (Figure 34). In the former, it is only possible to achieve sonic velocity as a maximum, as the pressure at station 2 is diminished (the 'back pressure'), for steady pressure at station 1 (the 'delivery pressure').

In a convergent-divergent nozzle for similar conditions, when the flow is choked at the throat of the nozzle, it is possible for the flow accelerate further in the divergent section so that supersonic speeds can be achieved while the mass flow rate is constant.

In either case, when the flow is choked, the only way for greater mass flow to issue from the nozzle is if the delivery pressure is increased. Under such choking conditions, the mass flow of gas no longer depends on the downstream pressure at station 2 (Figure 34); information on any pressure disturbance cannot propagate fast enough upstream, and through the sonic velocity section, to have an effect on the flow.
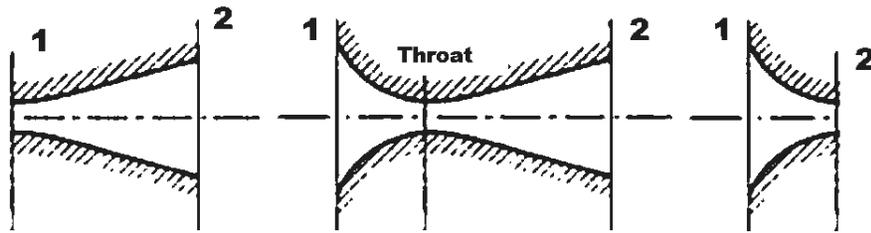
Figure 34: Divergent, Convergent-Divergent and Convergent nozzle.

The purpose of this chapter is to review and execute an analytical formulation for a convergent-divergent (CD) nozzle, so that such nozzles can be designed for particular duties of compressed air delivery pressure, temperature and mass flow within the ejector. This formulation will be used in two ways:

Firstly, for design nozzle geometries, the formulation will permit the profiles of pressure, temperature and velocity through and exiting the nozzle to be predicted, for specific compressed air delivery conditions. This is important in the context of the thesis as a whole because it is the motive nozzle that converts the high pressure, relatively high temperature air at inlet into high velocity, low temperature air at outlet. The work needs a method of altering the geometry of a nozzle under design so that the temperature of the air at nozzle outlet can be engineered to be sufficiently low to impart sufficient cooling to the mine ventilation air. Such nozzles can then be manufactured.

Secondly, and as will be presented in a subsequent chapter of the thesis, Computational Fluid Dynamics (CFD) is used as an ejector design tool, where the temperature and velocity of the air issuing from the motive nozzle are required as boundary conditions to such models

4.2 Pressure, velocity and temperature profiles in a CD nozzle

Figure 35 shows seven distinct cases of convergent-divergent nozzle performance that can occur, with the variation between the cases essentially comprising the magnitudes of delivery pressure (LHS) and back pressure (RHS) that exist across the nozzle, (M is the Mach number). In case Figure 35 a) the delivery pressure is relatively low, the flow at the throat of the CD nozzle is not choked, and the divergent section acts as a diffuser so that the pressure at inlet is nearly completely recovered at outlet. In this case, the nozzle behaves as a venturi meter.
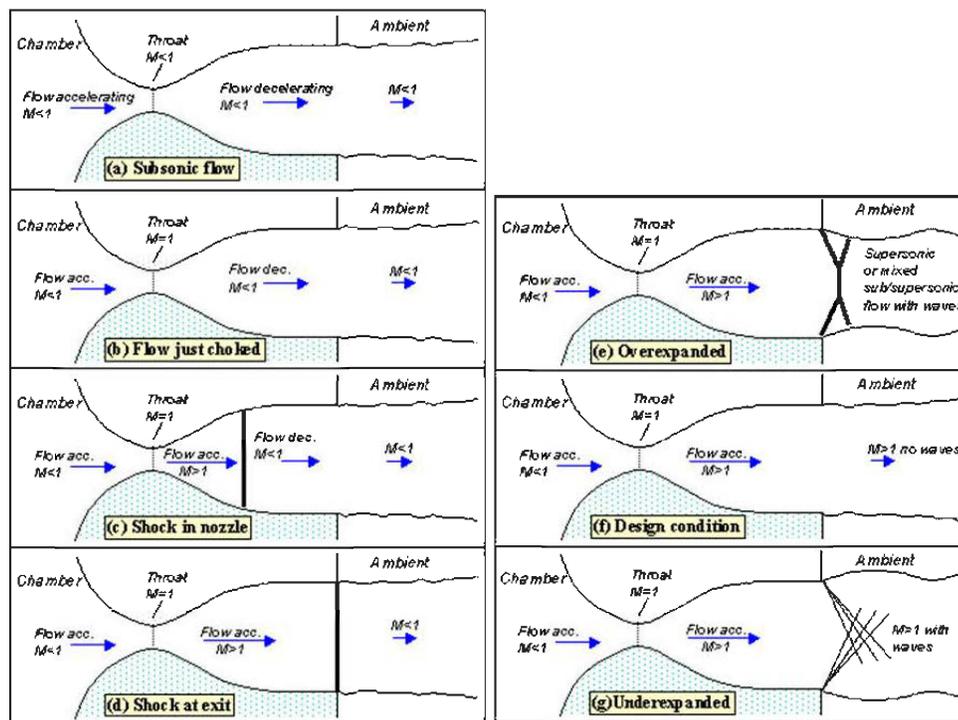
Figure 35: Nozzle flow patterns from Devenport, 2001

The difference between cases a) and b) in Figure 35, is that in the latter, the back pressure is reduced so that the flow accelerates sufficiently in the convergent section

to just become choked at the CD nozzle throat with the air moving at sonic velocity, and then it retards subsequently in the divergent section.

In four of the five remaining cases illustrated, shock waves develop as a means of satisfying energy, momentum and mass flow conditions and consistency with the back-pressure boundary condition. From the point of view of this work, thrust arising from mass flow in the free jet that issues from the CD nozzle is not really required. Instead it is the low temperature achievable in the depressurization and expansion of the air, according to the Joule-Thompson effect. In all of the five remaining cases, the desired very low temperatures result, but it is only in the case (f), involving so-called 'Design conditions' where the nozzle geometry, delivery pressure and back pressure are set at values where no shock wave results as the air issues from the CD nozzle.

The development of a shock wave in the air in the CD nozzle represents a major source of irreversibility. Shock irreversibility is manifest in the condition of the air as a rise of the air stream temperature, which is indistinguishable from the temperature rises attributable to simple frictional loss that, without the shock, would lead to estimates of the isentropic efficiency similar to those reviewed in Chapter 3.

Consequently, in order that the very low temperatures that are required of the motive nozzle in the mine ejector cooling concept presented herein are actually realized, it is vital that the motive nozzle remains in design condition at all times.
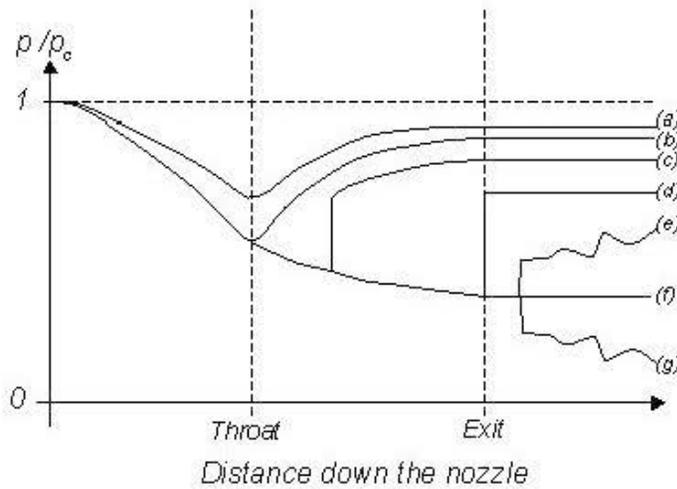
Figure 36: Pressure distribution along the nozzle from Devenport, 2001

As can be seen in Figure 36, the bracketed labels (a) to (g) reflect the back pressure boundary condition applying. In the application context this will be a relatively unvarying value equal to the absolute static pressure of the mine air at the location where the compressed air issues from the motive nozzle in the ejector. As an example, for a mining depth of around 2500 m and ignoring geothermal heating but considering adiabatic conditions in a 7 m diameter shaft with surface asperities around 0.01 m (a 'smooth' concrete lined shaft) passing 212 m³/s air, this pressure would be around 130.5 kPa, that is: surface atmospheric pressure plus the increase in pressure of the mine air after it has descended to the mine level where the refrigeration system is installed, less pressure drop due to airway friction. As airway doors are opened and closed, conveyances travel the shaft, this back-pressure may be expected to vary over a few kPa, that is: not much.

These deliberations on back pressure lead to an important realization that, for a fixed motive nozzle geometry (area of throat and area of exit plane) as the back pressure will remain broadly constant, the design condition may be maintained through the adjustment of the pressure of compressed air delivered to the motive nozzle. Such considerations are quite distinct from those that may be involved with the optimal

design of jet propulsion systems where the nozzle back pressure may be expected to vary substantially in service as vehicle altitude varies substantially. In these instances, it is thrust that is the central concern and air temperatures are of secondary importance. In the design of a motive nozzle for mine air cooling, it is the temperature of the issuing air that is of central concern and the thrust, although important, is a secondary design priority.

4.3 CD nozzle design formulation

Design of a CD nozzle for a particular duty or purpose essentially reduces to choose the shape of the nozzle. In order to calculate the best shape for the nozzle some assumptions are made: 1) no heat transfer, 2) no work on or by the fluid, 3) no change in elevation. The inlet flow comes from a large cross-sectional area reservoir where the velocity is very small denoted by 1 in Figure 37. The pressure P_1 and temperature T_1 at this point are the total or stagnation values. The expansion of the flow is done isentropically to achieve supersonic speed at the nozzle exit. This point denoted by 2 in Figure 37.
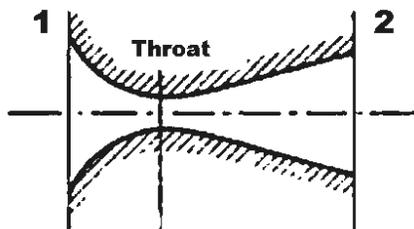
Figure 37: Schematic for subsonic-supersonic isentropic nozzle flow

The pressure and temperature are called delivery or exit values. In the CD nozzle the flow is subsonic at the entrance in the convergent section, at the throat area is sonic and at the divergent area is supersonic.

Assuming uniform flow properties across a cross-sectional area A where the flow properties vary only in the x direction, the governing equations can be expressed as

Continuity:

$$\rho_1 V_1 A_1 = \rho_2 V_2 A_2 \tag{56}$$

Momentum:

$$\rho_1 V_1 + \rho_1 V_1^2 A_1 \int_{A_1}^{A_2} P dA = P_2 A_2 + \rho_2 V_2^2 A_2 \tag{57}$$

Energy:

$$(h + \frac{1}{2} V^2)_1 = (h + \frac{1}{2} V^2)_2 \tag{58}$$

where the subscripts 1 and 2 denote the locations according to Figure 37. Additionally with the perfect gas equation of state,

$$P = \rho R T \tag{59}$$

the definition of heat capacity,

$$C_p - C_V = R \tag{60}$$

$$a_2 = \sqrt{\gamma R T_2} \tag{61}$$

where $\gamma = C_p/C_v$ the speed of sound, the stagnation equation from chapter 3 and the relations for an isentropic process

$$\frac{P_1}{P_2} = \left(\frac{\rho_1}{\rho_2}\right)^{\gamma} = \left(\frac{T_1}{T_2}\right)^{\frac{\gamma}{\gamma-1}} \tag{62}$$

the ratio of total static pressure, temperature and density at a point in the flow are function of the Mach number M.

$$\frac{P_1}{P_2} = \left(1 + \frac{\gamma - 1}{2} M^2\right)^{\frac{\gamma}{\gamma-1}} \tag{63}$$

$$\frac{\rho_1}{\rho_2} = \left(1 + \frac{\gamma - 1}{2} M^2\right)^{\frac{1}{\gamma-1}} \tag{64}$$

$$\frac{T_1}{T_2} = \left(1 + \frac{\gamma - 1}{2} M^2\right) \tag{65}$$

The variation of the Mach number through the nozzle is defined only by the area ratio.

$$\left(\frac{A_2}{A^*}\right)^2 = \frac{1}{M^2}\left[\frac{2}{\gamma + 1}\left(1 + \frac{\gamma - 1}{2} M^2\right)\right]^{\frac{\gamma+1}{\gamma-1}} \tag{66}$$

This implies that the ratio of the exit area A_2 to the throat area A^* defines if the flow is subsonic, sonic or supersonic. Therefore, the area ratio is responsible for the exact size of the nozzle.

4.4 Performance of small scale rocket motor CD nozzle

In this section the performance of the small scale rocket motor CD nozzle is tested. The CD nozzle utilized is a premanufactured nozzle (Figure 38). A performance prediction is done followed by the experimental procedure to verify such prediction.
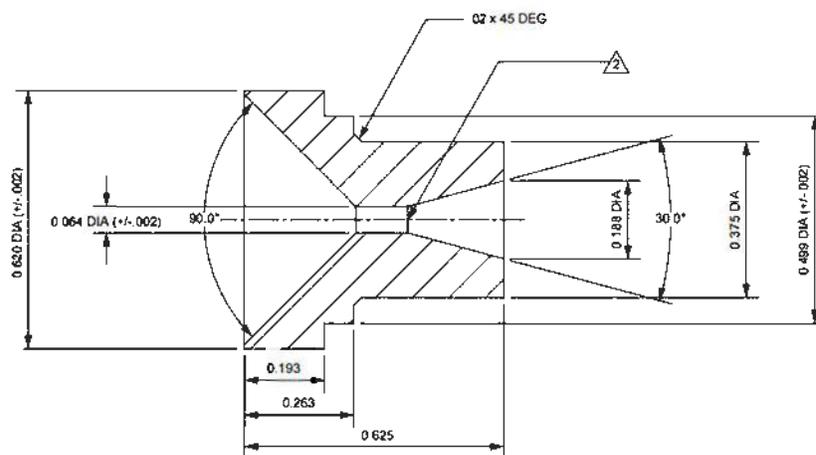
Figure 38: Schematic of a premanufactured rocket nozzle (in inches)

4.4.1   Performance prediction

The manufactured nozzle adopted for laboratory testing had a very simple shape with non-curved convergent and divergent surfaces. It was designed in plastic as a disposable unit for use in a toy rocket motor. For the operation conditions the area ratio 8.629 and the pressure ratio 0.009 defines the flow condition and the possibility of shock waves in it. . The shock wave is a sudden source of irreversibility, that is, inefficiency, relative to isentropic conditions, and so the temperature of the issuing air jet will be a lot higher than expected. Two cases are tested:

1) On-design conditions, the parameters used are collected in Table 7. On Figure 39 illustrate the shape of the nozzle, temperature and pressure profiles.

Table 7: On-design conditions

Parameter	Value	Unit
Delivery pressure	111.1	bar(abs)
Back pressure	1	bar(abs)
Pressure ratio	0.009	
Compressed air temperature	30	°C
Diameter of exit	0.188	inches
Diameter of exit	4.775	mm
Area of exit	17.909	mm2
Diameter of throat	0.064	inches
Diameter of throat	1.626	mm
Area of throat	2.075	mm2
Area ratio	8.629	
Convergence angle (cone)	90	o
Divergence angle (cone)	30	o
Convergence length	1.575	mm
Divergence length	5.877	mm
Total length	7.452	mm
Temperature of jet at exit	83.43	K
	-189.72	°C
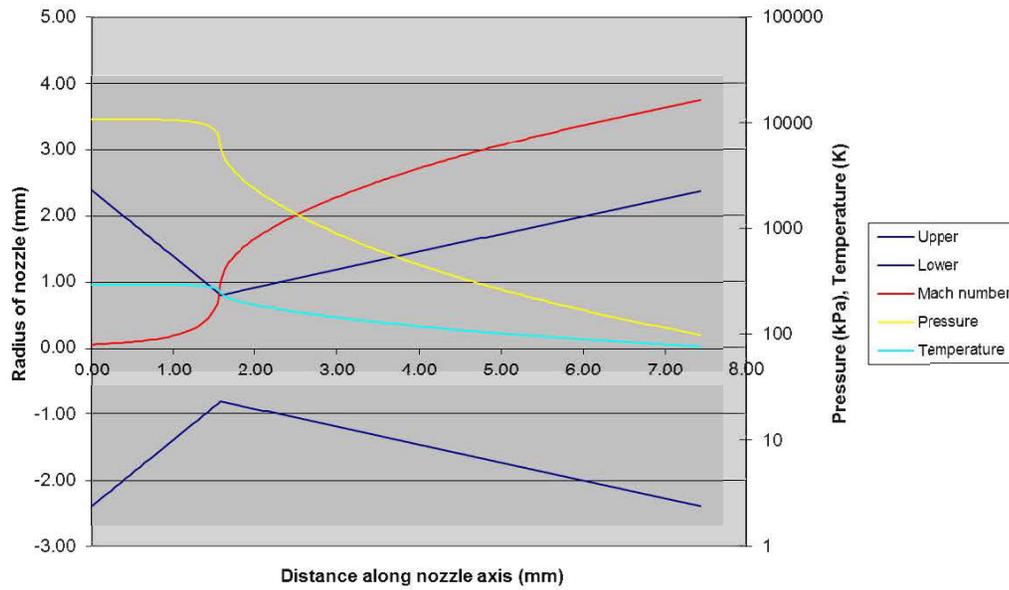
Figure 39: Shape of the nozzle, temperature, Mach number and pressure profiles on-desigu

The design condition for this nozzle geometry is a shockwave free jet as shown in Figure 39

2) Off-design conditions, the parameters used are collected in Table 8. On Figure 40 illustrate the shape of the nozzle, temperature and pressure profiles.

Table 8: Off-design conditions

Parameter	Value	Unit
Delivery pressure	4.5	bar(abs)
Back pressure	1	bar(abs)
Pressure ratio	0.222	
Compressed air temperature	30	°C
Diameter of exit	0.188	inches
Diameter of exit	4.775	mm
Area of exit	17.909	mm2
Diameter of throat	0.064	inches
Diameter of throat	1.626	mm
Area of throat	2.075	mm2
Area ratio	8.629	
Convergence angle (cone)	90	o
Divergence angle (cone)	30	o
Convergence length	1.575	mm
Divergence length	5.877	mm
Total length	7.452	mm
Temperature of jet at exit	297.72	K
	24.57	°C
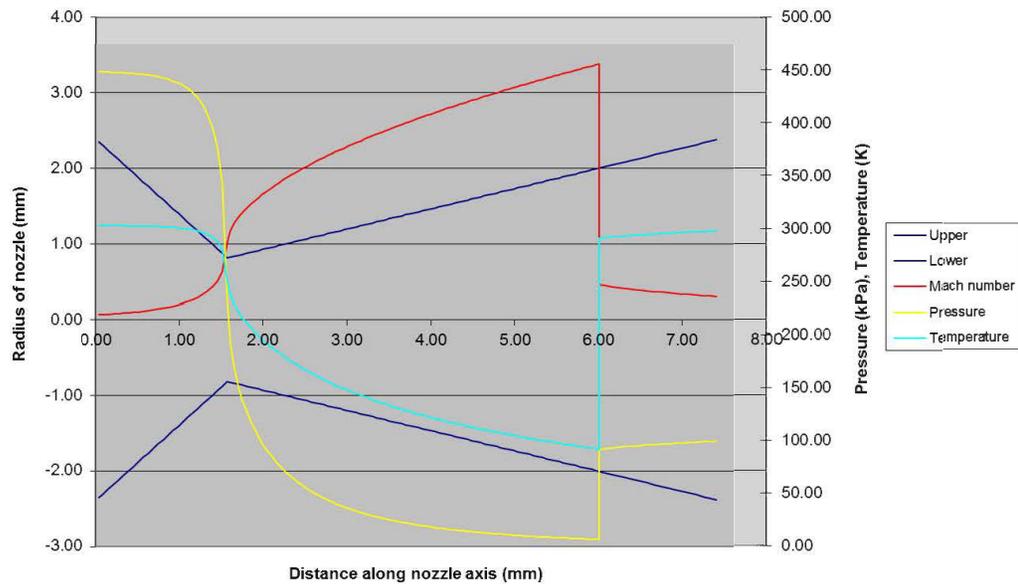
Figure 40: Shape of the nozzle, temperature, Mach number and pressure profiles off-design

The condition for this nozzle geometry reveals a shockwave inside the nozzle, which occurs at 6mm of distance along the nozzle axis. It is operating in a condition well off the design condition, a result of the low delivery pressure of 4.5 bar adopted. In that point there is a rise in pressure and temperature as illustrated in Figure 40.

4.4.2   Experimental performance

Making the comparison between thermal imaging camera, with the thermometer bulb in the shot and the prediction from the applet, the experimental performance can be obtained. It is important to remember that as the thermometer bulb was obstructing

the flow, the fluid would have been brought to rest, and thus will be higher than the temperature at which the air issued from the nozzle beforehand.

The temperature sensed by the thermal imaging camera is illustrated in Figure 41.
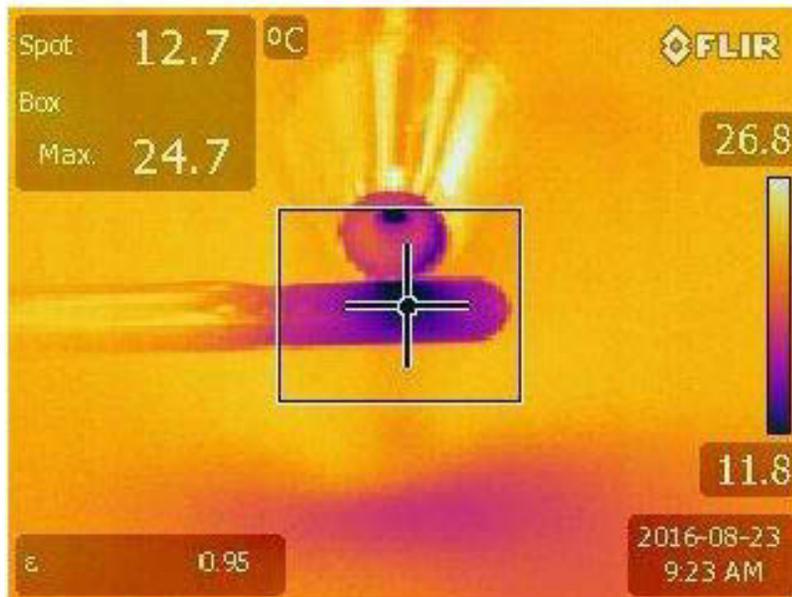
Figure 41: Thermal image of nozzle and thermometer

The problem is that it is not the real temperature of the gas, because in measuring the temperature, the gas is slowed down. In order to find the static temperature, the temperature that it would measure if the thermometer was moving with the air, the relations for stagnation must be applied. In table 9, the results are shown.

Table 9: Temperatures off design comparison

Parameter	Value	Unit
Assumed temperature of delivery air	30	°C
	303.15	K
Static temperature of the gas at exit (theroretical)	297.72	K
	24.57	°C
Velocity of the gas at exit (theroretical)	104.58	m/s
Heat capacity of the gas	1005	J/kg K
Stagnation temperature of the gas at exit (theroretical)	303.16	K
	30.02	°C
Temperature measured on thermometer (expected)	12.70	°C
Assumed velocity on thermometer	186.55	m/s
Near stagnation temp of gas at exit (measured)	285.85	K
Field velocity	104.58	m/s
Predicted field static temperature	297.72	K
	24.57	°C

With the static temperature the isentropic efficiency is obtained. The final nozzle efficiency is 4.42%.

4.5 Performance of a modified laboratory scale CD nozzle

In this section the performance of the modified scale rocket motor CD nozzle is tested. The CD nozzle utilized is the premanufactured nozzle from the last section after the throat is modified. The new throat is 2.2 times the original. A performance prediction is done followed by the experimental procedure to verify such prediction.

4.5.1 Performance prediction

Knowing the impact of the area ratio the diameter of the throat has been increased, therefore the area ratio decreased. For the operation conditions the area ratio 1.803 and

the pressure ratio 0.11 defines the flow condition and the possibility of no shock waves in the free jet. .

Table 10: Modified conditions lab scale

Parameter	Value	Unit
Delivery pressure	9	bar(abs)
Back pressure	1	bar(abs)
Pressure ratio	0.111	
Compressed air temperature	22	°C
Diameter of exit	0.188	inches
Diameter of exit	4.775	mm
Area of exit	17.909	mm2
Diameter of throat	0.14	inches
Diameter of throat	3.556	mm
Area of throat	9.931	mm2
Area ratio	1.803	
Convergence angle (cone)	90	o
Divergence angle (cone)	30	o
Convergence length	0.610	mm
Divergence length	2.275	mm
Total length	2.885	mm
Temperature of jet at exit	157.55	K
	-115.60	°C
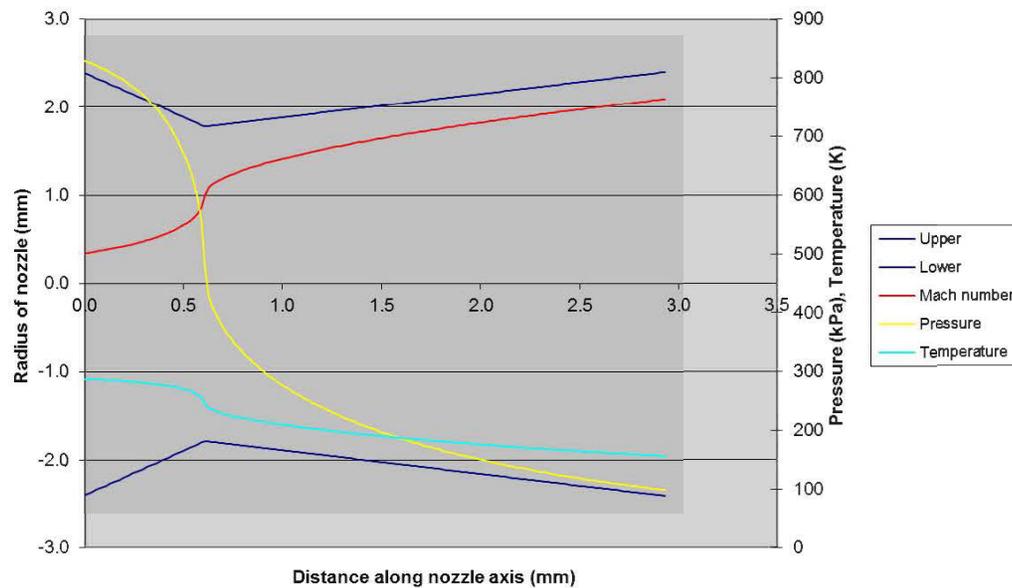
Figure 42: Shape of the nozzle, temperature, Mach number and pressure profiles of modified nozzle

The design condition for this nozzle geometry has no shockwave on the free jet. The trend is illustrated in Figure 42 where the Mach number increase as the pressure decrease.

4.5.2 Experimental performance

Making the comparison between thermal imaging camera, with the thermometer bulb in the shot and the prediction from the applet, the experimental performance can be obtained. It is important to remember that as the thermometer bulb was obstructing the flow, the fluid would have been brought to rest, and thus will be higher than the temperature at which the air issued from the nozzle beforehand.

The temperature sensed by the thermal imaging camera is illustrated in Figure 43.

Figure 43: Thermal image of modified nozzle and thermometer

The problem is that it is not the real temperature of the gas, because in measuring the temperature, the gas is slowed down. In order to find the static temperature, the temperature that it would measure if the thermometer was moving with the air, the relations for stagnation must be applied. In table 11, the results are shown.

Table 11: Temperatures lab scale comparison

Parameter	Value	Unit
Assumed temperature of delivery air	22	°C
	295.15	K
Static temperature of the gas at exit (theroretical)	157.55	K
	-115.60	°C
Velocity of the gas at exit (theroretical)	524.97	m/s
Heat capacity of the gas	1005	J/kg K
Stagnation temperature of the gas at exit (theroretical)	294.66	K
	21.52	°C
Temperature measured on thermometer (expected)	-14.3	°C
Assumed velocity on thermometer	270	m/s
Near stagnation temp of gas at exit (measured)	258.85	K
Field velocity	524.97	m/s
Predicted field static temperature	158.01	K
	-115.14	°C

With the static temperature the isentropic efficiency is obtained. The final nozzle efficiency has increased from 4.42% to 99.17%.

4.6 Performance of a CD nozzle for 750 Scfm mass flow.

In this section the performance of a 750 Scfm mass flow CD nozzle is tested. The CD nozzle utilized has been manufactured on steel stainless following the shape of previous CD nozzle tested. A performance prediction is done followed by the experimental procedure on a flied test to verify such prediction.

4.6.1   Performance prediction

For the operation conditions the area ratio 1.69 and the pressure ratio 0.111 defines the flow condition and the possibility of shock waves in the free jet. .

Table 12: Field Modified conditions

Parameter	Value	Unit
Delivery pressure	9	bar(abs)
Back pressure	1	bar(abs)
Pressure ratio	0.111	
Compressed air temperature	8	°C
Diameter of exit	0.870	inches
Diameter of exit	22.100	mm
Area of exit	383.597	mm2
Diameter of throat	0.669	inches
Diameter of throat	17.000	mm
Area of throat	226.980	mm2
Area ratio	1.69	
Convergence angle (cone)	90	o
Divergence angle (cone)	15	o
Convergence length	2.550	mm
Divergence length	19.369	mm
Total length	21.919	mm
Temperature of jet at exit	159.24	K
	-113.91	°C
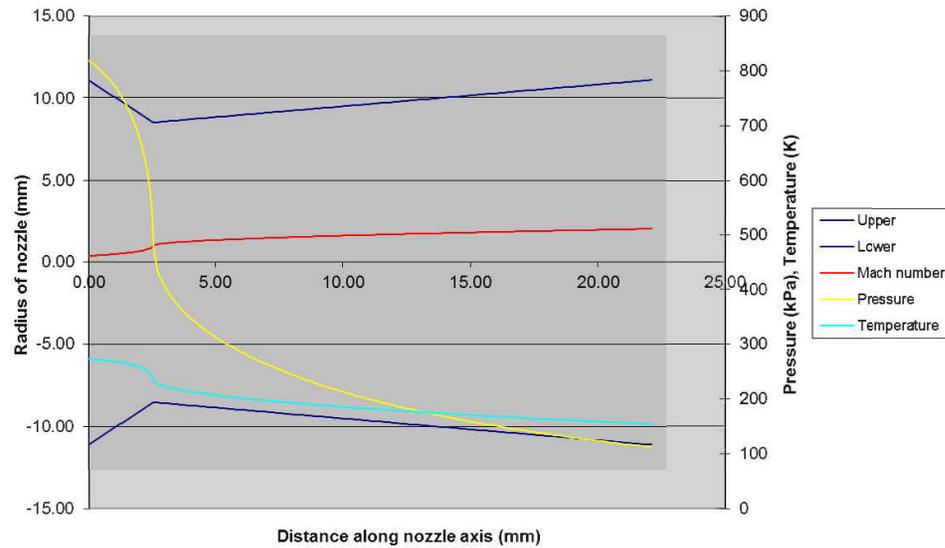
Figure 44: Shape of the nozzle, temperature, Mach number and pressure profiles of modified nozzle

The design condition for this nozzle geometry has expansion shockwave on the free jet. The trend is illustrated in Figure 44 where the Mach number increase as the pressure decrease

4.6.2   Experimental performance

Making the comparison between thermal imaging camera, with the thermometer bulb in the shot and the prediction from the applet, the experimental performance can be obtained. It is important to remember that as the thermometer bulb was obstructing the flow, the fluid would have been brought to rest, and thus will be higher than the temperature at which the air issued from the nozzle beforehand.

The temperature sensed by the thermal imaging camera is illustrated in Figure 45.
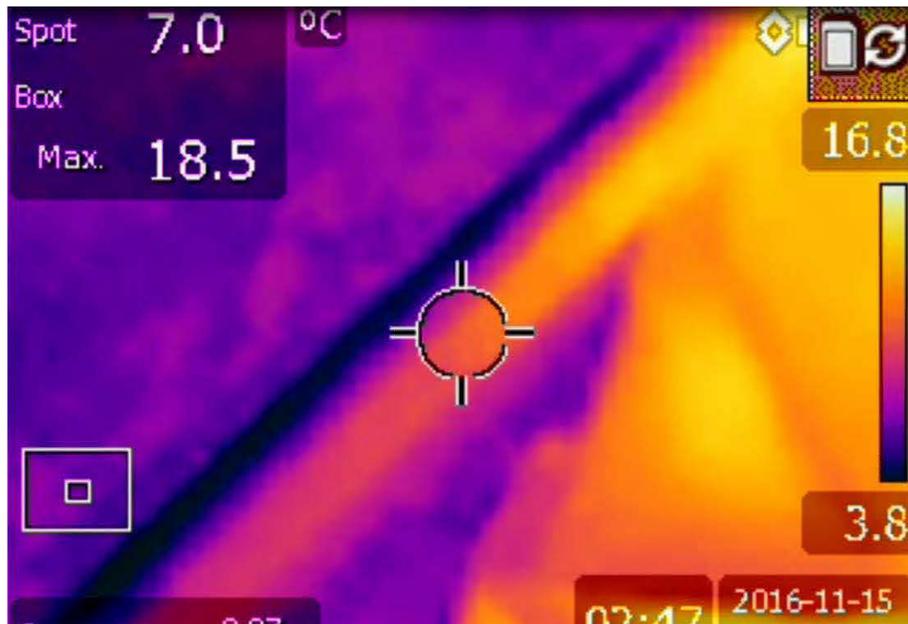
Figure 45: Thermal image of modified nozzle and thermometer

The problem is that it is not the real temperature of the gas, because in measuring the temperature, the gas is slowed down. In order to find the static temperature, the temperature that it would measure if the thermometer was moving with the air, the relations for stagnation must be applied. In table 13, the results are shown.

Table 13: Temperatures field comparison

Parameter	Value	Unit
Assumed temperature of delivery air	8	°C
	281.15	K
Static temperature of the gas at exit (threroretical)	159.24	K
	-113.91	°C
Velocity of the gas at exit (threroretical)	500.77	m/s
Heat capacity of the gas	1005	J/kg K
Stagnation temperature of the gas at exit (threroretical)	284.00	K
	10.86	°C
Temperature measured on thermometer (expected)	7.00	°C
Assumed velocity on thermometer	299.39	m/s
Near stagnation temp of gas at exit (measured)	280.15	K
Field velocity	500.77	m/s
Predicted field static temperature	199.98	K
	-73.17	°C

With the static temperature the isentropic efficiency is obtained. The final nozzle efficiency is 60.92%.

4.7 Performance of a CD motive nozzle for a mine scale ejector

Table 14: Mine scale conditions

Parameter	Value	Unit
Delivery pressure	8.50	bar(abs)
Back pressure	1.35	bar(abs)
Pressure ratio	0.16	
Compressed air temperature	-105.00	°C
Diameter of exit	4.528	inches
Diameter of exit	115.000	mm
Area of exit	10386.902	mm2
Diameter of throat	4.094	inches
Diameter of throat	104.000	mm
Area of throat	8494.876	mm2
Area ratio	1.22	
Convergence angle (cone)	90.00	o
Divergence angle (cone)	30.00	o
Convergence length	5.500	mm
Divergence length	20.526	mm
Total length	26.026	mm
Temperature of jet at exit	112.24	K
	-160.91	°C
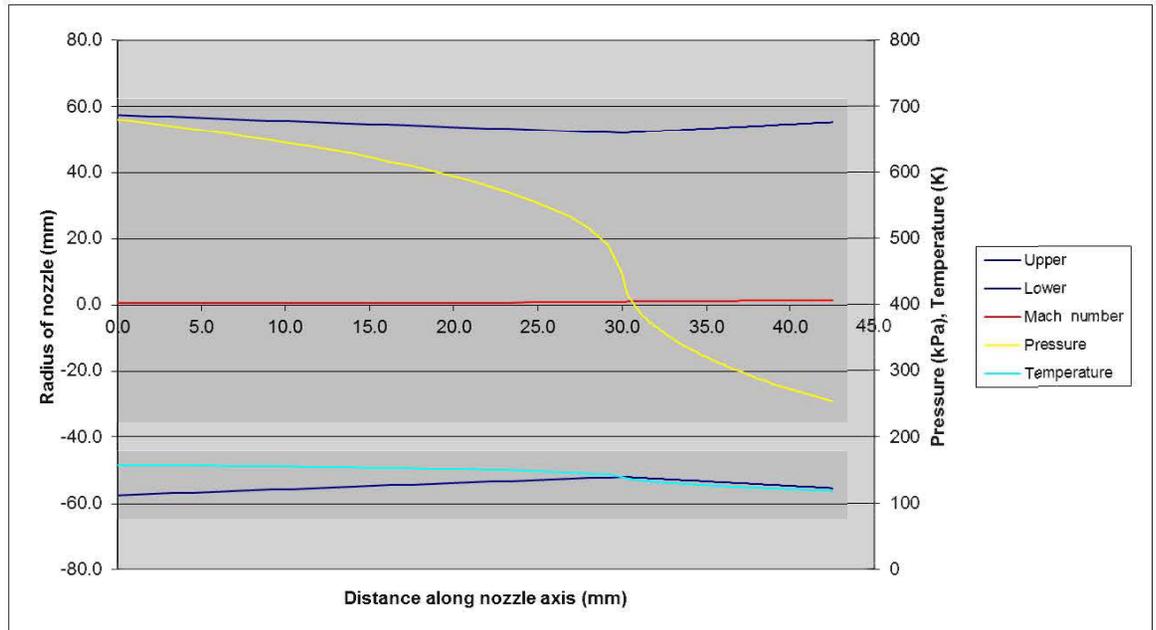
Figure 46: Shape of the nozzle, temperature, mach number and pressure profiles of modified nozzle

The design condition for this nozzle geometry has expansion wave on the free jet. This undexpanded wave is due to the exit area is too small for the optimum area ratio. An increase of pressure is created at the exit of the nozzle where the total expansion is complete. The trend is illustrated in Figure 46 where the Mach number stays constant as the pressure decrease.

Using the parameter shown on Table 14, a prediction of isentropic efficiency was performance assuming that it will possible to measure the temperature of the gas with a thermometer a 500 m/s. The isentropic efficiency would be 79.03%.

4.8 Discussion

In this chapter has been shown a full description of how to design a nozzle. It was explained how to calculate the exit mass flow and temperature

The design condition for the motive nozzle is where the air issuing from the nozzle does so without a shock wave. The design delivery pressure for the small scale rocket motor CD nozzle is approximately of the order of 100 bars, this nozzle has been manufactured only for propulsion purposes. Consequently, as it is running 'off design', in the latter case a shock wave inside the CD nozzle. Therefore the isentropic efficiency is very low less than 5%.

On the performance of the laboratory scale CD nozzle, the area ratio is reduced. This produces the desire effect and the system works under design condition, as result of this the isentropic efficiency is very high over 95%.

The field test performance of the CD nozzle for 750 scfm mass flow results in a overexpansion creating a shock wave on the free jet and reducing the isentropic efficiency to 60%.

Finally the CD motive nozzle for a mine scale nozzle. The prediction for the mine scale nozzle is an underexpanded nozzle with an efficiency of 79%

The assumptions made, following the results from the experiment on the ventilation test bench, will determine the hypothesis for the CFD model in chapter 5. The specific case where the assumption of inlet velocity negligible of the nozzle is not applicable has been explained as well. The stagnation value for the initial velocity was described with the nozzle flow patterns remarking the importance of the shape for the outcome. Finally, the values obtained for the design nozzle will be the boundary conditions to performance the CFD simulation.

CHAPTER 5

DESIGN AND PERFORMANCE OF A LAB SCALE COOLING EJECTOR

5.1 Introduction

Following the results from the experiment on the ventilation test bench, will determine the hypothesis for the CFD model in this chapter. The values obtained for the design nozzle will be the boundary conditions to performance the CFD simulation.

5.2 Experimental program using a lab scale cooling ejector

After the CFD simulation, the laboratory experiment was carried out to validate the CFD results. Several parameters and settings applied in the simulation need to be verify in order to trust the results. For instance, any small variation on the mesh for the ejector varies the CFD results. Therefore, a verification of the results is required. In this chapter, the fabrication of the model is explained with the test conditions and instrumentation used for this purpose. Then the results of the physically experiments are presented.

5.2.1 Fabrication of lab scale ejector

The main concern about the fabrication of the model is the control of the geometry. Since the ejector is very precise equipment a control mechanism should be used to manufacture it. For this reason, a 3D printer was chosen. The 3D lab scale model ejector was tested in a scale ventilation rig at the ventilation laboratory. The pressure drop achieved in the ventilation rig was compared with the CFD model results.

The use of the 3D printer had its limitations as well. The size of the lab scale model ejector could not exceed the dimensions of 0.3m x 0.3m x 0.3m, due to capability of the 3D printer to manufacture under this range. Besides, the connection to the ventilation rig had to fit perfectly. After scaling the ejector from the mine scale model it was noticed that the ejector required needed 49 cm length in order to perform its proper function. In practice, that meant to manufacture the ejector in three pieces and assembling them together. Other constraint of the lab scale model was the support of the nozzle. In the mine scale model, was not necessary since the jet pipe would be attached to the rock ceiling. However, for the lab scale model a support system was necessary. For that reason, a circular ring with three aerodynamic pattern bars, 2 mm width separated 120 degrees from each other, were used. This support, connected to the walls of the suction chamber, separated by a distance of 150.88 mm from the mixing section; allows having a movable nozzle. Besides, this outline was necessary to avoid turbulence and vortex effects. Finally, to accommodate the instrumentation at specific locations, where it was required to control the nozzle conditions and the ejector performance, orifices were introduced on the 3D lab scale model.

The ejector was manufactured using the Dimension 1200es (Dimension, 2013) 3D printer. The model material is P430ABS plus. The printer format is Stereo Lithography

format (.STL) which can be converted to from Solidworks format (.SLDPRT). Depending on the direction decided beforehand the layers are different. In this case, the direction chosen was perpendicular to the inlet and outlet, obtaining layers of <1mm of thickness. The total time of manufacture was 72 hours for two pieces, including the acid bath P400-SC needed after the printer, to dissolve the construction support plate debris. After the printing, a concern was raised. The roughness of the 3D printed ejector could affect the results increasing the flow resistance. This concern is explained later on the experimental results.

For the final ejector piece, 18 mm motive nozzle from Rocket Motor Components Inc, with a 0.064 inches, 0.0016256 m, throat was used (Figure 47 and Figure 48).

Figure 47: Rocket nozzle, lateral view

Figure 48: Rocket nozzle, top view

At the beginning of the suction nozzle, a coupling section was needed to support it and give it an aerodynamic shape (Figure 49 and Figure 50). This component was manufactured in stainless steel to resist the compressor pressure, and to connect to a 20 mm pipe.

Figure 49: Coupling section, lateral view

Figure 50: Coupling section, top view

In Figure 51, Figure 52 and Figure 53 are illustrated the ejector 3D printed before assembling

Figure 51: Suction-Mixing chamber, lateral view

Figure 52: Suction-Mixing chamber, top view

Figure 53: Diffuser, lateral view

5.2.2   Description of the ejector test rig

The purpose of this verification experiment was to confirm the CFD results, in particular the secondary mass flow and the exit temperature. The steps were:

- The ejector model was assembled.
- The nozzle was assembled together with the coupling piece and the delivery pipe. Then, this assembly it was placed inside the ejector.
- An orifice of 0.072136 m is placed in the middle of the rig and half of the exit is taped to increase the pressure along the rig.

- The ejector with the nozzle assembly is connected to the rig and taped to avoid air losses.

- The delivery pipe from the compressor is connected.

- The nozzle position is chosen and the ejector is leveled and aligned.

- The instrumentation is installed.

- The compressor is started and run until it achieved a steady operating point.

- The room pressure and temperature is recorded. Then the measurements of each instrument were recorded in each point. Finally, the thermal camera takes the temperature at the thermistor inlet.

There are seven measuring points to get enough information to confirm CFD, they are illustrated in Figure 54, Figure 55 and Figure 56:
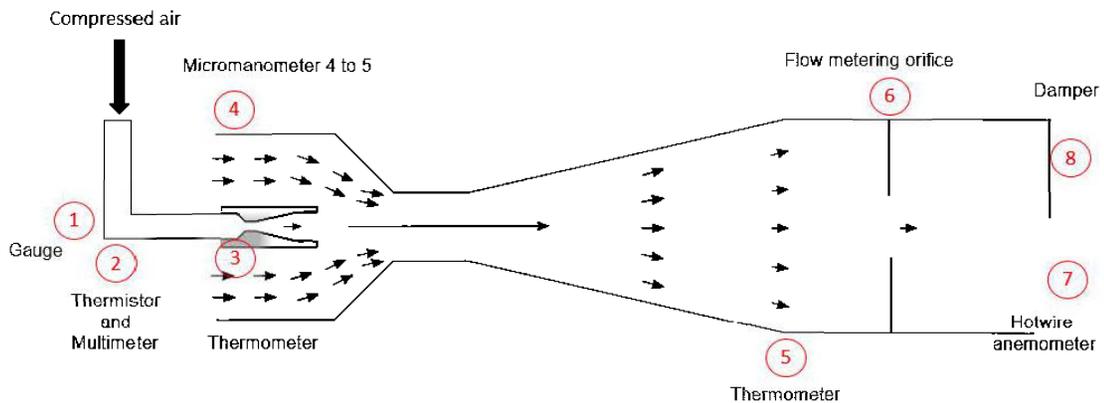
Figure 54: Schematic of the laboratory experiment

1. Gauge, measure the pressure delivery by the compressor at steady operating point.

2. Thermistor, measure the temperature delivery by the compressor at steady operating point.

3. Yellow thermometer, measure the temperature at the inlet for the secondary flow,
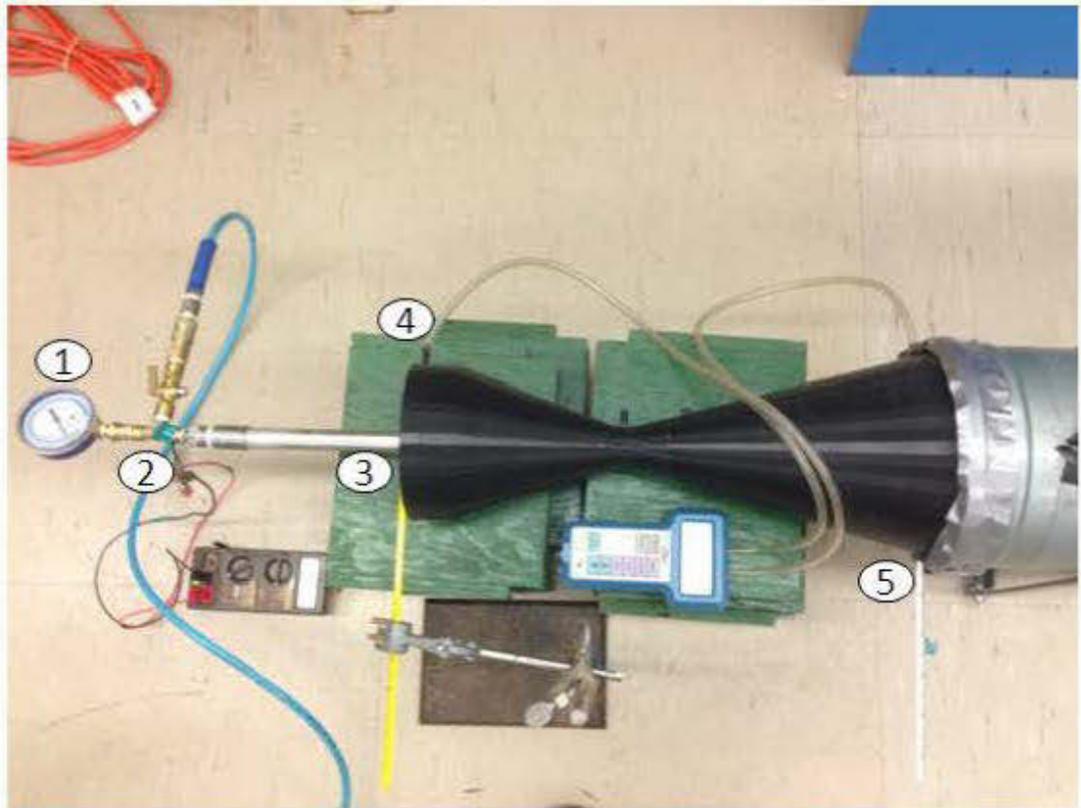
Figure 55: Laboratory setup, ejector.

4. Micromanometer, measure the pressure drop across the eductor, between position 4 and 5.

5. White thermometer, measure the temperature of the mixed flow.

6. Micromanometer, measure the pressure drop across the orifice rig.

7. Hotwire anemometer, measure the velocity of the flow at the exit

8. Damper, to create resistance and increase the pressure.
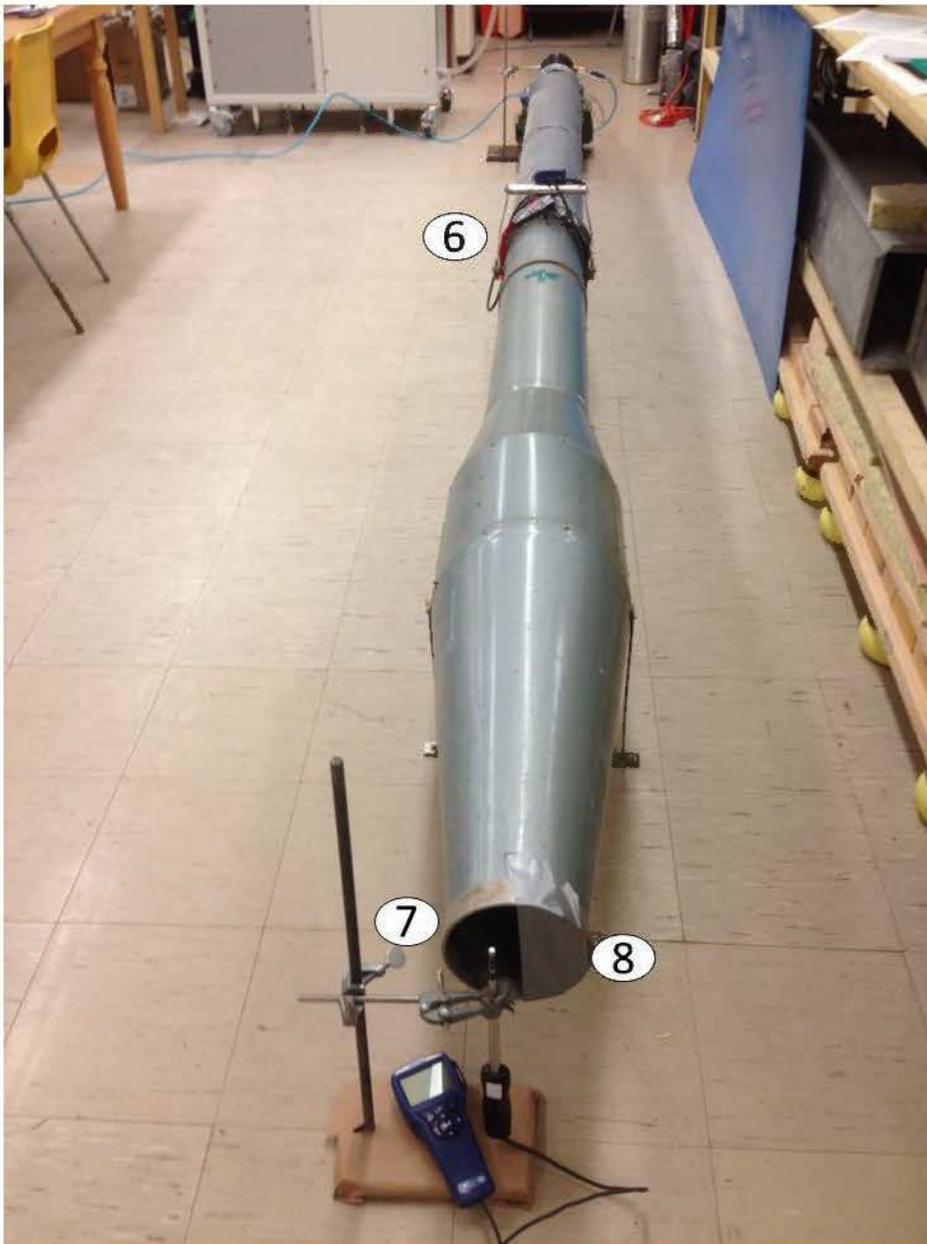
Figure 56: Setup of the ventilation rig

The instrumentation used in each measuring point, illustrated in Table 15, are explained in detail in Appendix D,

Table 15: Instrumentation used for the test

Instrumentation	Position	Measuring	Units
Gauge	Exit compressor delivery	Pressure	Pa
Thermistor	Exit compressor delivery	Temperature	°C
Multimeter	Connected to the thermistor	Temperature	kΩ
Thermomether F.	Inlet eductor	Temperature	°C
Micromanometer 8702	Inlet-outlet eductor	Drop pressure	Pa
Thermomether B.	Outlet eductor	Temperature	°C
Micromanometer 5825	Restriction point	Drop pressure	Pa
Hotwire anemometer	Exit ventilation rig	Velocity	m/s
Digiquartz pressure	Two meters away from eductor	Pressure	kPa
Hygrometer - Thermomether	Two meters away from eductor	Temperature	°C
Thermal camera	Exit compressor delivery	Temperature	°C

5.2.3   Testing procedure

In this section the four experiments are explained.

5.2.3.1   Commissioning experiment

The commissioning experiment is based on the results obtained during the CFD simulations. The main hypothesis is that the best nozzle exit position is 60mm away from the entrance of the mixing chamber. It was expected a 1000 Pa pressure increase, 10 °C drop in temperature and an entrainment ratio of 10.9 for the mass flow.

The observations from the first experiment were a pressure drop of 21 Pa, 0.85°C drop in temperature and an entrainment ratio of 5.66 for the mass flow. The first test rejected the hypothesis. This discrepancy in the results was assumed by a problem of recirculation or vortex, also the scale. In order to verify the real issue, the nozzle pipe was removed from the 3D eductor.

5.2.3.2 Nozzle experiment

For the second experiment, the hypothesis is that the nozzle efficiency is high, around 73%. In this case, a special setup was used, as illustrated in Figure 57 and Figure 58.

Figure 57: Setup nozzle experiment
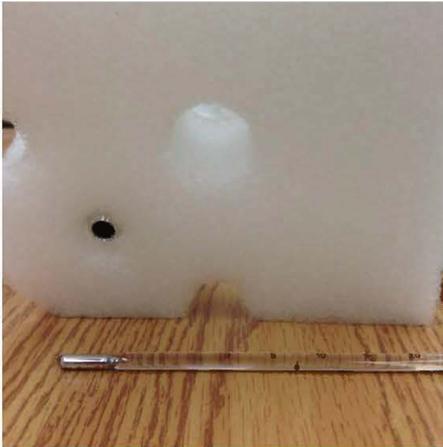
Figure 58: Zoom exit nozzle and thermometer

Using the Fisherbrand thermometer, the thermal camera and a piece of polystyrene to insulate the steel couple piece outside the rocket nozzle; the temperature was measure at the steady operation point of the compressor, 3.9 bar. The minimum temperature measure at 23.13°C and 98.467 kPa room conditions, it was 11.8°C, this is illustrated in Figure 59.
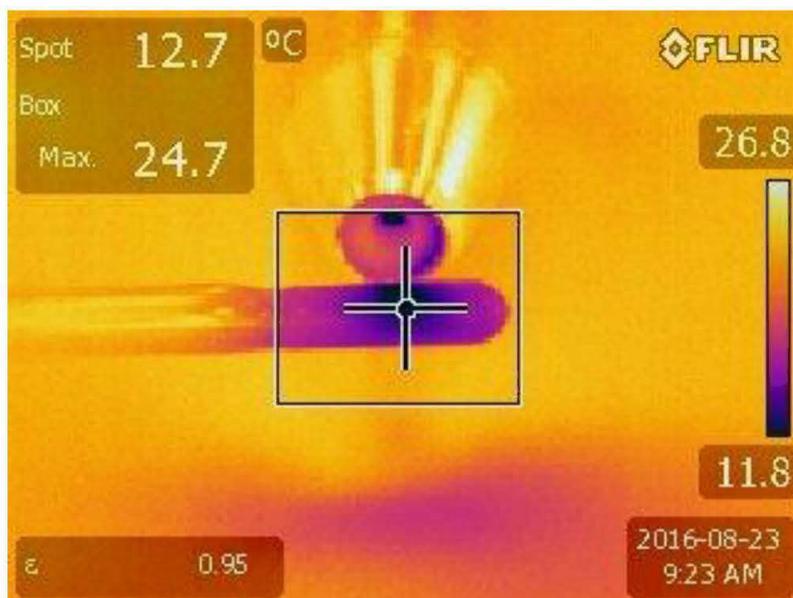
Figure 59: Thermal image of nozzle and thermometer

In order to verify the result the nozzle equations must be applied and stagnation conditions explained.

When a thermometer is inserted into a moving gas stream, the gas around the bulb of the thermometer is brought to rest. This arresting process takes placed suddenly with little chance for heat transfer, and is also frictionless as there is no 'duct' for the fluid to flow along. Hence the process may be taken to be a frictionless adiabatic; that is, an isentropic process. In the current context any measurement taken with a thermometer will not measure the ordinary or static temperature because the gas streams are moving with appreciable velocity. Instead, the thermometer will measure a so-called stagnation temperature, and will have to be corrected to allow for the velocity.

A suppose gas moves with a velocity (V) and temperature (T) to rest adiabatically, attaining a temperature T_0 at rest, called stagnation or total temperature, applying that to the steady flow energy equation:

$$\frac{(V^2 - V_0{}^2)}{2} + g(Z - Z_0) + W_{12} = h_0 - h - q_0 \tag{67}$$

Applying, now usual assumptions of constant elevation, adiabatic with no work and recognising that the fluid is brought to rest:

$$h = h_0 + \frac{V^2}{2} \tag{68}$$

$$C_P T = C_P T_0 + \frac{V^2}{2} \tag{69}$$

$$T_0 = T + \frac{V^2}{2 C_P} \tag{70}$$

The stagnation temperature T_0 is measured by the bulb of a thermometer placed in the gas stream since the gas moves to rest. The static values are only possible to measure with thermometer moving at the same velocity as the gas.

Using the isentropic relationship

$$\frac{T_2}{T_1} = \left(\frac{P_1}{P_2}\right)^{\frac{\gamma-1}{\gamma}}$$

(71)

An approximation to the stagnation pressure can be derived for cases where the velocity is less than 0.2 times the speed of sound (that is, in the current context, at inlet)

$$P_1 = P_2 + \frac{\rho V_2^2}{2}$$

(72)

At the inlet to a nozzle, the velocities are relatively low (23.22m/s) for the laboratory experimental case, but nevertheless the equations above can be used to correct thermometer measured values, if they are measured with a thermometer, before being used to assed the nozzle critical pressures and temperatures.

From the values measured, the rest are calculated using NIST, (2005).

Table 16: Initial values

Parameters	Symbol	Value	Units
Absolute pressure	P1	490	kPa
Temperature in Celsius	t1	23.13	°C
Temperature in Kelvin	T1	296.28	K
Entropy	s1	6.398799	kJ/kg K
Enthalpy	h1	295.6637	kJ/kg

Table 17: Isentropic values

Parameters	Symbol	Value	Units
Back pressure	P2	98.467	kPa
Temperature in Celsius	t2s	-86.2091	°C
Temperature in Kelvin	T2s	186.9309	K
Entropy	s2s	6.398799	kJ/kg K
Enthalpy	h2s	186.5444	kJ/kg

Table 18: Actual values

Parameters	Symbol	Value	Units
Back pressure	P2	98.467	kPa
Temperature in Celsius	t2	11.8	°C
Temperature in Kelvin	T2	284.95	K
Entropy	s2	6.823007	kJ/kg K
Enthalpy	h2	285.1703	kJ/kg

Therefore the final nozzle efficiency is

$$\eta_{nozzle} = 9.62\%$$

These calculations confirm that the isentropic efficiency for high efficiency nozzle is correct.

Since the hypothesis for the nozzle is correct, a third experiment is performance.

5.2.3.3   Eductor secondary inlet blocked experiment

With the observations of the second experiment a nozzle efficiency of 9.62% is expected. In order to verify the value of the nozzle efficiency is correct, the third experiment is done. In this case, the inlet area of the eductor was blocked with a cardboard piece. The experiment was done as explained in section 6.3. The results are presented in the Table 19.

Table 19: Results from secondary mass flow blocked according to NXP

Parameters	NXP, Nozzle Exit Position			Units
	72	60	48	mm
Date	24-Aug	24-Aug	24-Aug	dd-mm
Time	16:25	17:42	17:50	hh:mm
Atmospheric pressure	98101	98080	98077	Pa
Atmospheric temperature	24.3	24.4	24.3	°C
Multimeter	12.67	12.64	12.63	kΩ
Thermistor	23.22	23.28	23.3	°C
Thermometer F.	23.3	23.5	24	°C
Thermometer B.	22.75	22.9	22.75	°C
Drop pressure eductor	1307	1203	925	Pa
Drop orifice rig	5.4	5.1	4.9	Pa
Hotwire anemometer	0.88	0.83	0.8	m/s
Gauge	3.9	3.9	3.9	bar

The data of this experiment, in particular the drop pressure across the orifice rig, the hotwire anemometer velocity, atmospheric temperature and pressure was used to obtain the mass flow.

Table 20: Mass flow calculations

Parameters	NXP, Nozzle Exit Position			Units
	72	60	48	mm
Atmospheric pressure	98101	98080	98077	Pa
Atmospheric temperature	24.3	24.4	24.3	°C
Density	1.1568	1.1562	1.1565	kg/m^3
Mass flow	0.00659	0.00641	0.00629	kg/s

In order to verify this value, the mass flow at the nozzle throat has to be the same as the exit nozzle to confirm the adiabatic hypothesis. Using the known geometry of the nozzle, the critical and initial properties, which was explained before they don't depends on the geometry only on the gas, the throat mass flow is calculated.

Table 21: Throat mass flow

Parameters	Value	Units
Throat diameter	0.064	in
	1.6256	mm
Throat area	2.08E-06	m2
Throat flow rate	6.56E-04	m3/s
Throat mass flow	0.002404	kg/s

When the same method is applied to the nozzle exit mass flow the final value doesn't match.

Table 22: Nozzle exit mass flow

Parameters	Value	Units
Exit diameter	0.188	in
	4.7752	mm
Exit area	1.79E-05	m2
Exit flow rate	2.60E-03	m3/s
Exit mass flow	0.003134	kg/s

Since these values must match to keep the mass continuity, the discrepancy on the nozzle efficiency is due to the measurement temperature value assumed. The final nozzle efficiency is 5.825% and the actual temperature at the exit is 15.87°C. The hypothesis has been probed before but the nozzle efficiency is lower. From the observations, the increase on the mass flow of 4 g/s is due to the small holes through the eductor and the connection with the rig. This explanation is verified by the Atkinson equation where the drop pressure in a fan is due to the resistance at which is connected.

$$P_{drop} = RQ^2 \tag{73}$$

These values from observations in the second and third experiment are the background for the fourth experiment.

Table 23: Data analysis from mass flow measurements

Parameters	NXP 60 , Nozzle Exit Position 60 mm			Units
	Eductor	Before Orifice	Rig exit	
Drop pressure	1203	5.1	0	Pa
Pressure	96882.1	98085.1	98080	Pa
Mass flow	2.4		6.4	g/s

5.2.3.4   Field test

A convergent divergent nozzle fabricated in aluminum was fitted to a 750 Scfm capacity industrial, portable, 2 stage, diesel fueled air compressor manufactured by Sullair. The compressor was operated and the temperature of the air jet issuing from the nozzle was estimated by sensing the surface temperature of a steel bar 'drogue' held within the flow of the exiting air jet, around 30 cm from the nozzle exit. (Figure 60) The operating condition during test was 8 bar (gauge) at 1440 rpm. The ball valve was completely open during test: The nozzle throat diameter was 17.5 mm. The nozzle exit diameter was 22.1 mm. The nozzle divergence angle was 15° from axis to divergent section. The purpose of the experiment was to obtain proof of concept that nozzles could be designed to produce appreciable temperature drops in expanded air jets, after the discrepancy obtained in the laboratory test.

Figure 60: High speed air jet impinging on steel 'drogue' bar during test. Drogue surface was not polished and was oxidized.

Compressed air delivery pressure was measured on a gauge mounted on the compressor panel. Compressor speed was set to be the lowest practically possible without compromising the compressor lubrication system. With ball valve in the completely open position, the pressure measured by the gauge was assumed to be that applying in the chamber, immediately upstream of the convergent-divergent nozzle. Practically, this pressure was 8 bar, around 2 bar higher than the 6 bar design chamber pressure for the nozzle, assuming atmospheric back pressure. Consequently, it was known before the test started that i) the nozzle would be operating in an off design condition, ii) the air would be underexpanded at the nozzle exit, and iii) a shock wave

introducing appreciable irreversibility would arise downstream of the convergent-divergent nozzle exit.

Using the nozzle equations introduced in chapter 4, some prediction were done before the final results of the field test as shown in Table 24.

Table 24: Prediction for the field nozzle test

Parameters	Value	Unit
Pressure at exit of nozzle	125.65	kPa
Mass flow rate	0.4744	kg/s
Volumetric flow rate	777.6	scfm
Velocity at nozzle exit	544.53	m/s
Temperature at nozzle exit	-74.3	°C

Temperatures sensed with the thermographic imaging camera taken of the cavity upstream of the nozzle orifice are free from incident light and other incident radiation, and hence reflections or other interferences that would otherwise complicate interpretation. It can be reasonably certain that the temperature of the compressed air delivered to the upstream nozzle chamber was around 76 to 78°C.

Air temperatures measured on the steel 'drogue' bar upon which the jet exiting from the nozzle impinged are subject to greater difficulties in interpretation. The complications arise due to i) reflections of ambient light off the 'drogue' surface and ii) the sensed temperatures of the drogue surface being close to the ambient air temperature of 8°C and the background hard standing asphalt at around 5 to 6°C.

The emissivity parameter for the thermographic camera was set for steel.

Figure 61, imaging the lee side of the steel drogue seems to provide the most reliable evidence of a thermal effect of the air jet on the drogue, with the drogue located around 30 cm from the nozzle exit plane. Within this image, the drogue appears to be being heated by the air jet above and below the spot measurement point, although the

temperature 'observation' from these upper and lower locations will depend, to some extent, on reflections from ambient sources, including diffuse sunlight. To the left and right of the spot measurement point, along the drogue, the lowest temperatures (of 2.1°C) recorded in the field of view are on surfaces that are approximately normal to the camera viewing direction. These areas are thought to be outside the zone of thermal influence of the impinging jet. Consequently, a drogue surface temperature of around 8°C is speculated from this image.
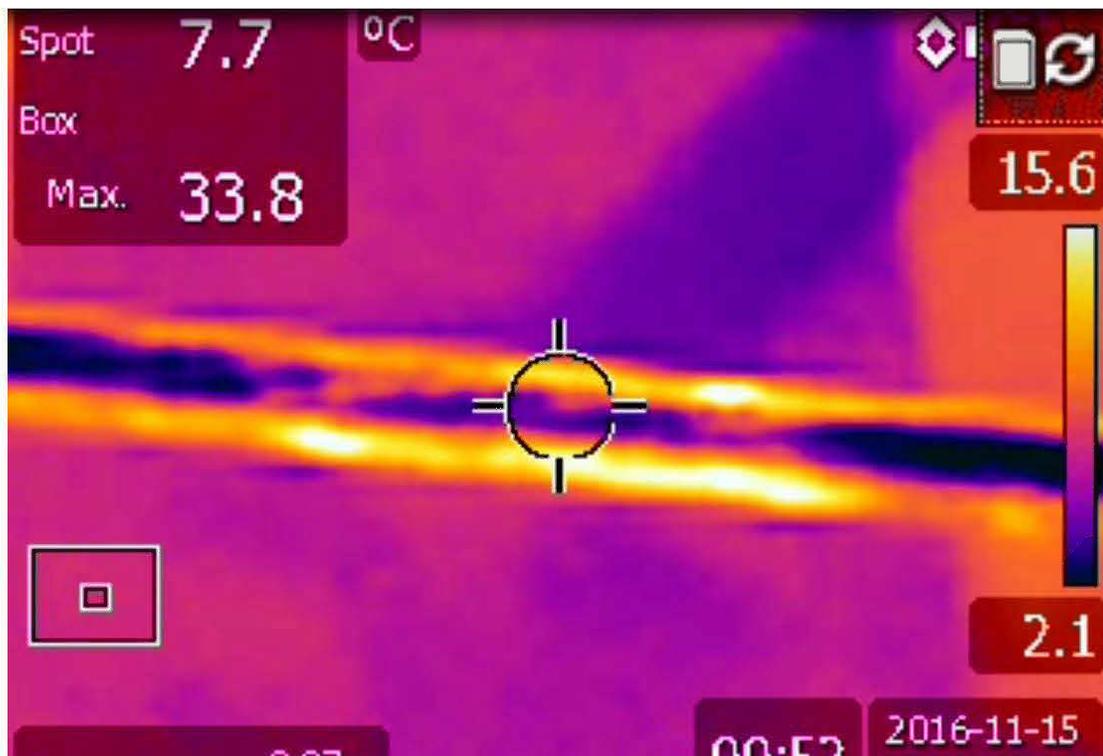
Figure 61: Thermal image of the drogue held within impinging air jet issuing from nozzle. Taken from a position so that drogue is positioned between nozzle and thermal imaging camera, such that the spot temperature (of 7.7°C) measures the temperature of the rear (lee side) of the steel bar.

Figure 62 images the upstream side of the drogue and suggests a drogue surface temperature of around 7°C within the zone of the impinging air jet.
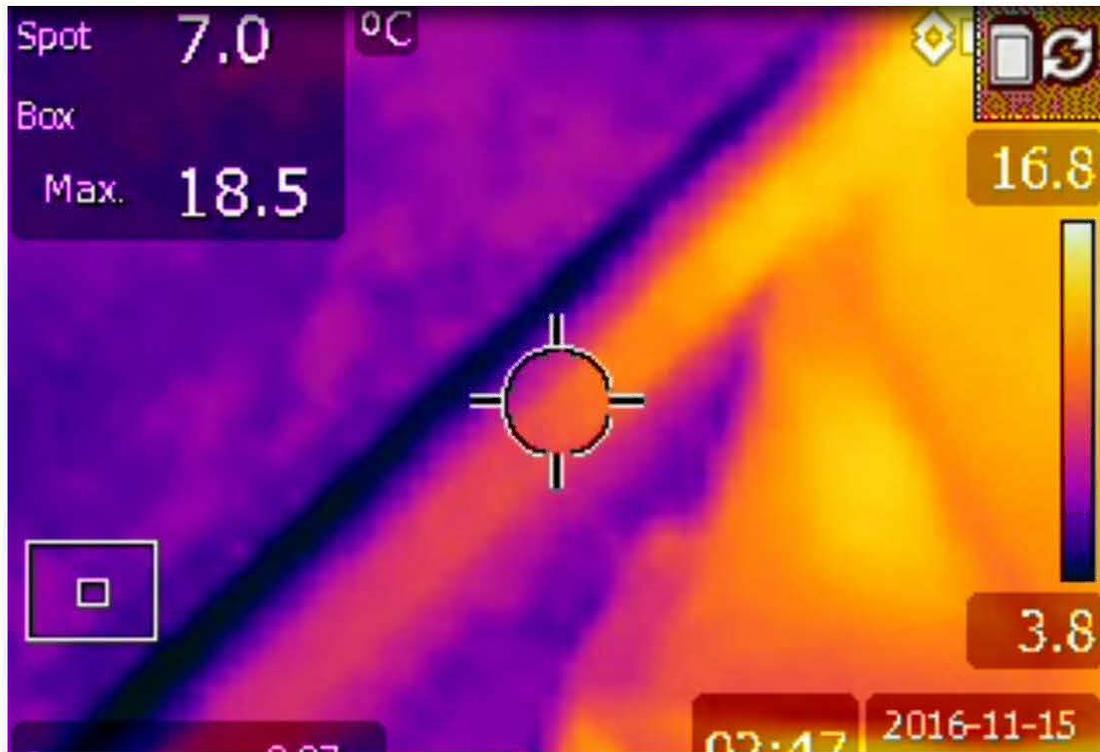
Figure 62: Thermal image of the steel drogue held within the impinging air jet in order to sense the latter temperature. Image taken from a direction looking onto the face of the drogue. Spot temperature (of 7.0°C) location is approximately normal to viewing direction.

Passing one's hand from atmospheric air across the air jet approximately 2 meters from the nozzle exit plane and back revealed that the air temperature felt slightly colder than ambient.

With a nozzle chamber temperature of between 76 and 78°C and jet temperature at the drogue location estimated at 7 to 8°C, a provisional conclusion is that the nozzle has produced a temperature drop of at least ~70°C. If the compressed air had been

aftercooled to ambient temperature of 8°C, a temperature of around -62°C may have been produced on the drogue surface. (Figure 63)
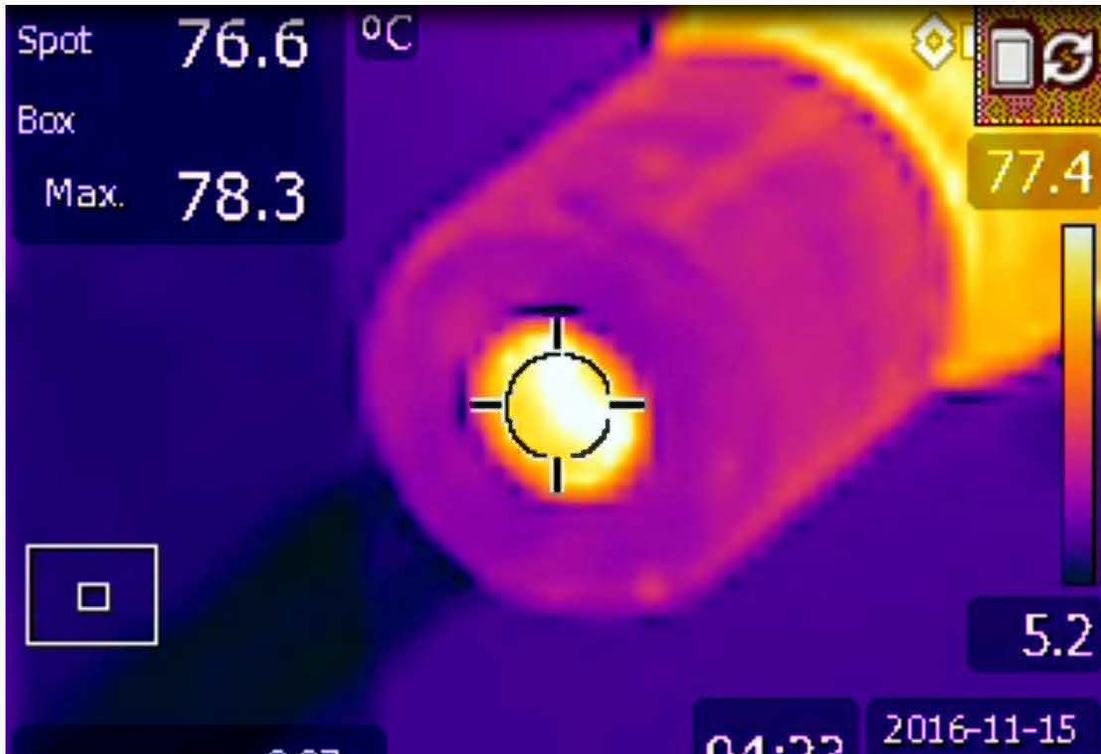
Figure 63: Thermal image of the nozzle mounted on the compressor while air jet issuing from nozzle. Highest temperature sensed is 78.3°C (off the inner surface of the nozzle viewed through the orifice), corresponding approximately to spot value beneath cross hairs (76.6°C). Note that nozzle exterior surface was non-oxidized and reflective. The 2 inch adapter upon which the nozzle was mounted was made of steel that was highly oxidised.

Nozzle analysis predicted that the flow through the nozzle was choked (mass flow 0.4689 kg/s; 768.6 Scfm), and confirmed that at 8 bar (g) it was operating in an off-design condition (the design chamber pressure was 6.2 bar (g)). With this higher delivery pressure, the jet was underexpanded in the nozzle (predicted pressure at nozzle

exit = 125.65 kPa). A shock wave would be expected in the jet as it moved from the nozzle into the free atmosphere and this would represent a source of irreversibility leading to higher air jet temperatures than in the design operating condition, however the location of this irreversibility is unknown. According to the nozzle equations using the actual pressure (8 bar (g)) and temperature (76°C) sensed for the compressed air in the nozzle delivery chamber, the air jet temperature was predicted to be -73.17°C at the nozzle exit. Nozzle isentropic efficiency (including the expected shock wave irreversibilities) under the observed operating conditions would thus be estimated at around 50%.

During all the test runs, the lowest temperature seen with the thermal imaging camera was -16.7°C (Figure 64).
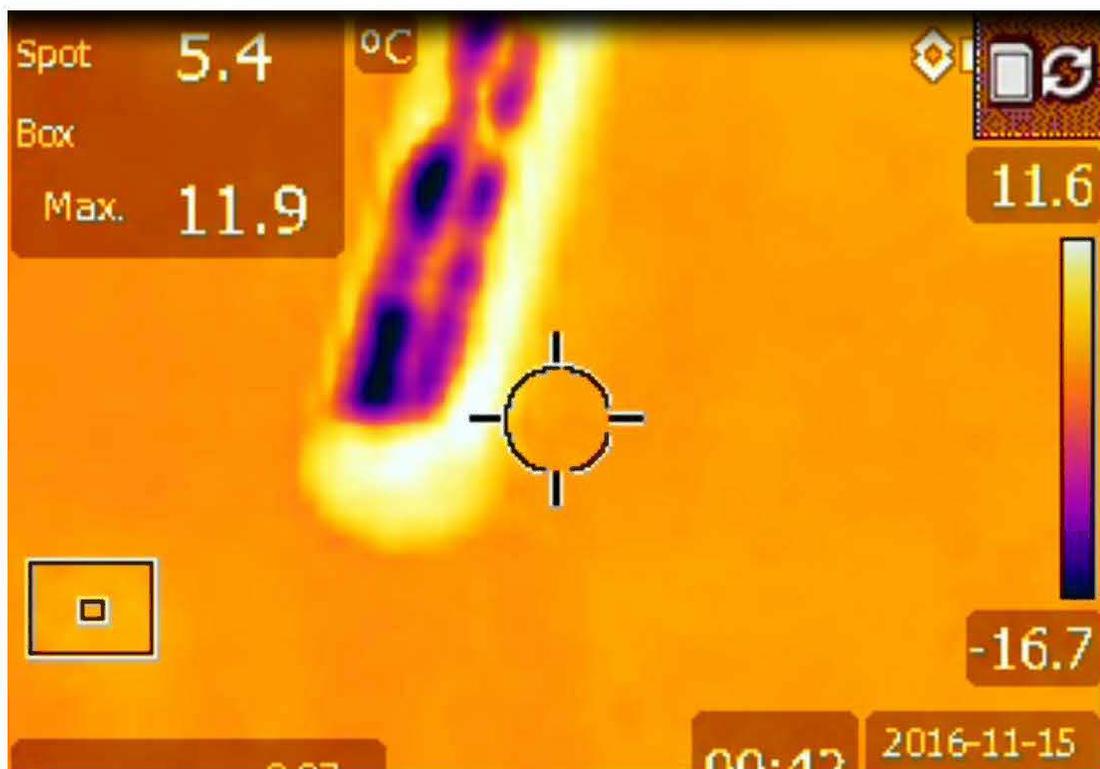
Figure 64: Thermal image of the steel drogue used to sense the temperature of the impinging air jet. Lowest temperature sensed on the upper surface of the cylindrical drogue (-16.7°C). Spot temperature on the ground below drogue (5.4°C)

5.2.3.5   Eductor experiment

The hypothesis for the fourth experiment is nozzle efficiency 5.825% and the expected temperature at the exit is 15.86°C.

The test was performed as explained above. The nozzle was placed in three different positions, far from the mixing chamber, 48, 60 and 72mm.

5.2.4   Presentation of results

The results are presented in Table 25.

Table 25: Final test measurements

Parameters	NXP, Nozzle Exit Position						Units
	72		60		48		mm
Location	Laboratory	Test	Laboratory	Test	Laboratory	Test	n/a
Date	24-Aug	24-Aug	24-Aug	24-Aug	24-Aug	24-Aug	dd-mm
Time	10:53	11:30	12:14	13:03	15:04	15:40	hh:mm
Atmospheric pressure	98541	98495	98489	98434	98364	98272	Pa
Atmospheric temperature	23.6	23.9	23.8	24.2	24.1	24.2	°C
Thermometer F.	23.5	23.5	23.6	23.6	23.7	23.7	°C
Thermometer B.	23.2	22.5	24	22.75	23.3	23	°C
Multimeter	12.41	12.79	12.59	12.69	12.58	12.67	kΩ
Thermistor	23.73	22.99	23.38	23.19	23.4	23.22	°C
Thermo Camera °C	23.8	23	23.5	22	23.3	22	°C
Drop pressure eductor	0	29	0	21	0	15	Pa
Drop orifice rig	0	37.8	0	32.9	0	27.3	Pa
Drop throat difusser	0	250	0	300	0	150	Pa
Hotwire anemometer	0	2.62	0	2.45	0	2.22	m/s
Compressor	0	5.5	0	5.5	0	5.5	bar
Gauge	0	3.9	0	3.9	0	3.9	bar

The measurements are used to obtain the results from the experiments.

The results values are calculated using the equations from chapter 4 and the direct measurements.

Table 26: Results from experiments

Parameters	NXP, Nozzle Exit Position			Units
	72	60	48	mm
Temperature at nozzle exit	15.73	15.93	15.94	°C
Nozzle isentropic efficiency	5.825	5.83	5.844	%
Mass flow rate of nozzle	0.002405	0.002404	0.002404	kg/s
Velocity of air at nozzle exit	113.05	113.15	113.34	m/s
Mass flow through orifice	0.0171	0.0160	0.0146	kg/s
Secondary mass flow	0.0147	0.0136	0.0122	kg/s
Eductor mass flow ratio	6.1306	5.6668	5.0786	
Temp of inducted air	23.5	23.6	23.7	°C
Temp of mixed air	22.41	22.45	22.42	°C
Predicted Temperature difference Induced to Mix	1.09	1.15	1.28	°C
Actual Temperature difference Induce to Mix	1.0	0.85	0.7	°C

Those values from observations verify the hypothesis of the experiment. According to the data presented in Table 26, the actual temperature difference between the induced and the mix is maximum 1°C. Some of the values measure during the experiment were photographed and then scaled to obtain as much accuracy as possible.

This represents a potential error on the final experimental results because of the instrumentation resolution. Since there is a discrepancy in the results obtained before with the CFD, the field test were performance to confirm the impact of the nozzle in the results.

5.2.5   Discussion and conclusion

In this chapter has been shown a full description of the ejector laboratory experiment and its results. It was explained the fabrication of the model, the experimental procedure, instrumentation and final results.

The assumptions made, following the results of the laboratory model, will determine the expected results for ejector design in chapter 5.2. The results obtained show the impact of the nozzle diameter in the outlet temperature and entrained mass flow. The hypothesis was verified through the laboratory experiment. Finally a field test showed that the nozzle has a direct impact on the final performance of the ejector.

In the next chapter, new CFD simulations will be performance to confirm the experiment since there is a discrepancy in the results obtained before. Several parameters and settings applied in the simulation need to be verify in order to trust the results.

5.3 CFD simulation of a lab scale cooling ejector

After the laboratory experiment was carried out, a discrepancy was found. To validate the results a CFD simulation needs to be done. Defined parameters and settings must be applied in the simulation to verify the laboratory experiments. In this chapter, a verification of the laboratory results is explained with the settings and parameters for this purpose on the CFD model. Then a comparison with the results of the physically experiments are presented.

5.3.1 Geometry of ejector

The geometry of the ejector is defined by the lab scale model. Using the geometry illustrated in Figure 65, the simulations were run.
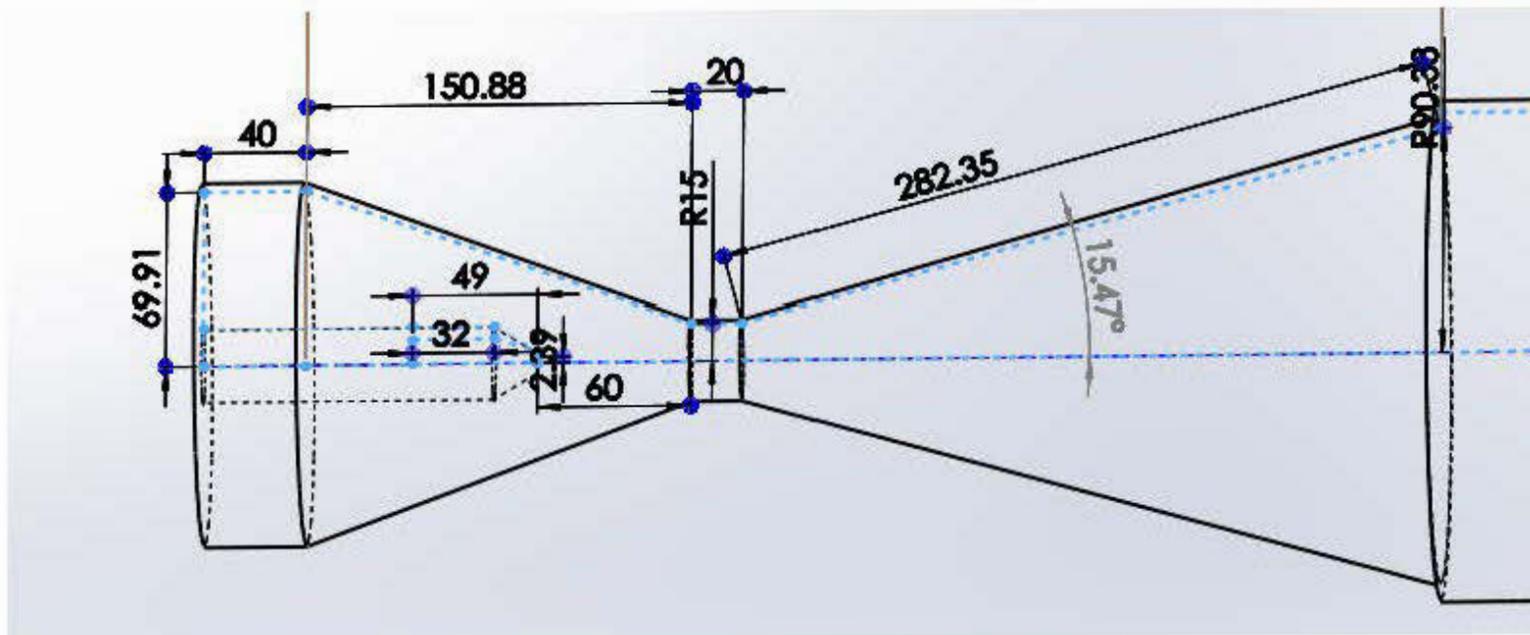
Figure 65: Geometry final of the educator

5.3.2   Boundary and initial conditions applied

The values for this verification were a pressure drop of 21 Pa, 0.85°C drop in temperature and an entrainment ratio of 5.66 for the mass flow. These values are applied for the NXP 60 position. All the values are compiled in Table 27.

Table 27: Values expected for the CFD simulation

Parameters	NXP, Nozzle Exit Position			Units
	72	60	48	mm
Temperature at nozzle exit	15.73	15.93	15.94	°C
Nozzle isentropic efficiency	5.825	5.83	5.844	%
Mass flow rate of nozzle	0.002405	0.002404	0.002404	kg/s
Mass flow through orifice	0.0171	0.0160	0.0146	kg/s
Secondary mass flow	0.0147	0.0136	0.0122	kg/s
Eductor mass flow ratio	6.1306	5.6668	5.0786	
Temp of inducted air	23.5	23.6	23.7	°C
Temp of mixed air	22.41	22.45	22.42	°C
Drop pressure eductor	29	21	15	Pa
Atmospheric pressure	98495	98434	98272	Pa

The settings using during the simulation for the CFD are the same as used for the mine simulations which will be explain on detail in chapter 6. The main differences are the boundary conditions. Since the boundary conditions are changed the turbulence intensity and the hydraulic mean diameter are recalculated for each specific position. It is important to mention that the pressure in each case is used as the operating condition.

5.3.3   Method of monitoring the CFD model

The three cases converged. In order to verify this convergence, three monitors were applied: the scale residuals, mass weight average inlet total pressure and mass weight

average outlet static temperature. The mesh was verified as well at the end, to confirm the quality of the adapt mesh gradient.

5.3.4 Presentation of results

A cross sectional XY plane was defined in Ansys to visualize the results.

In Figure 66, a comparison of the static pressure is illustrated, where the optimum suction pressure point into the ejector is 60 NXP.
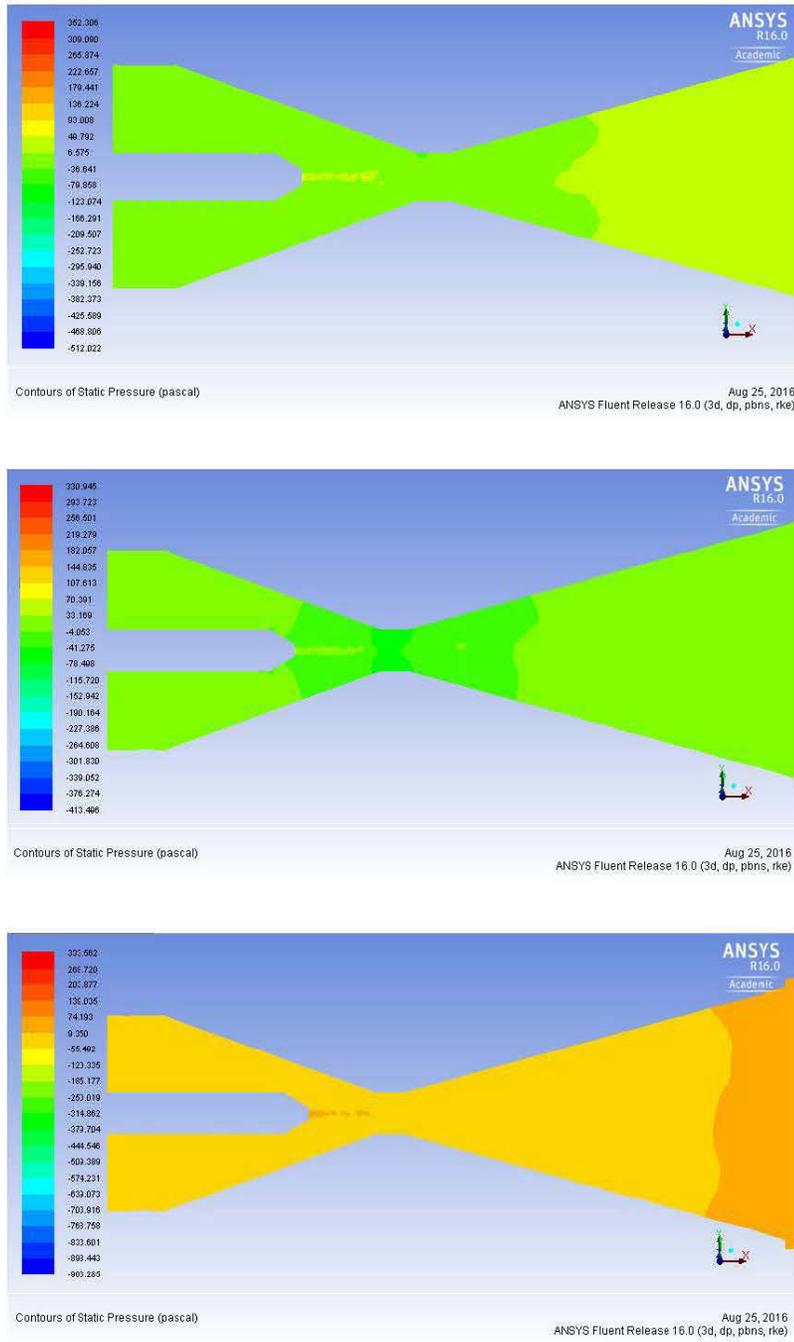
Figure 66: XY plane for static pressure at NXP 72, 60 and 48

In Figure 67, a comparison of the velocity magnitude is illustrated, where 60 NXP is the optimum point of entrainment with the same velocity.
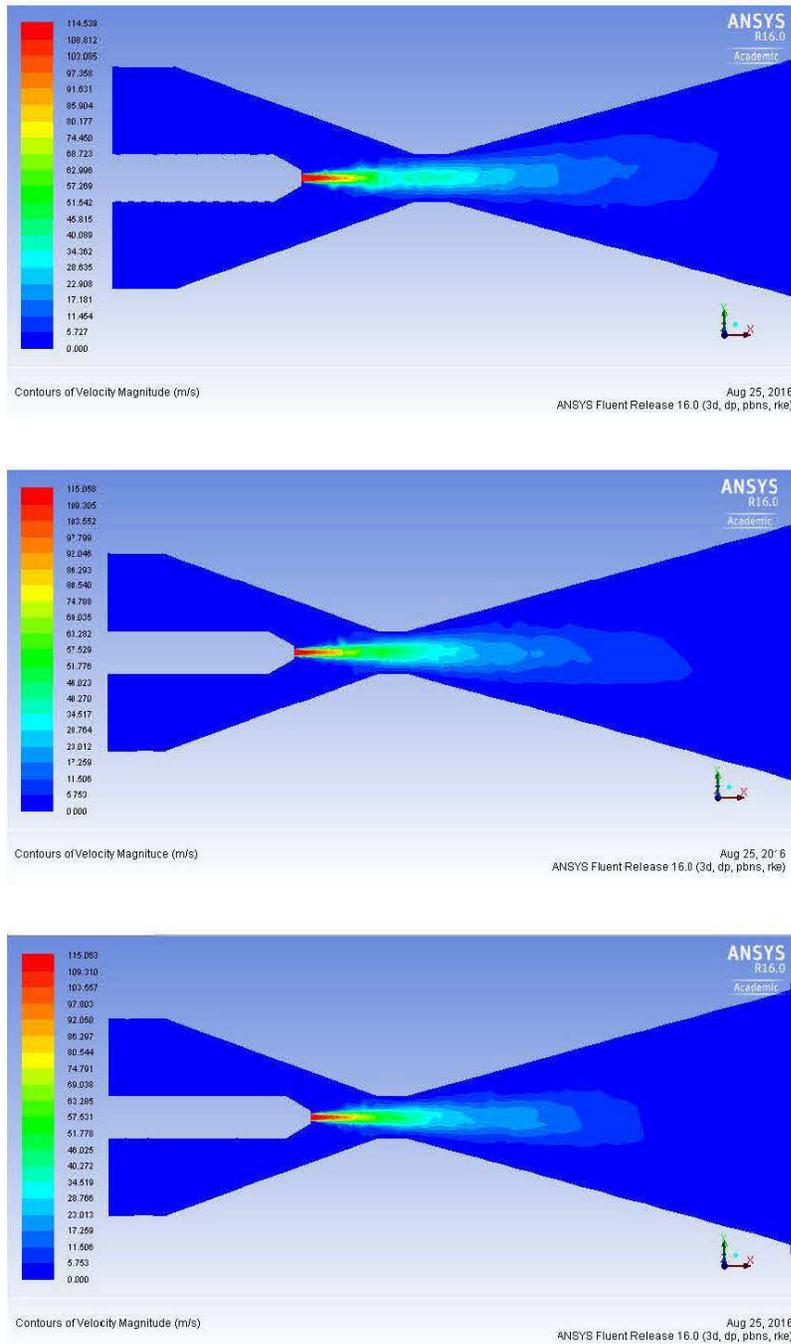
Figure 67: XY plane for velocity magnitude at NXP 72, 60 and 48

In Figure 68 a comparison of the static temperature is illustrated, where the optimum point for reducing temperature is 48 NXP.
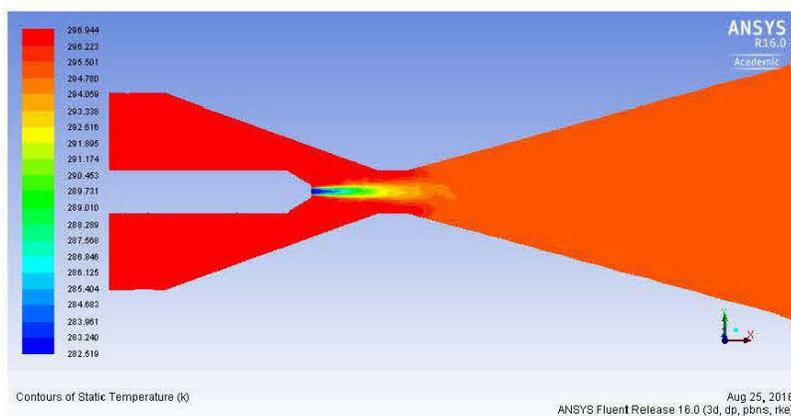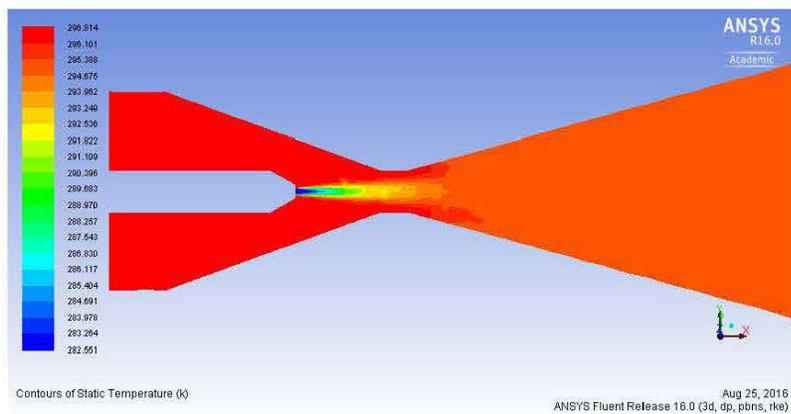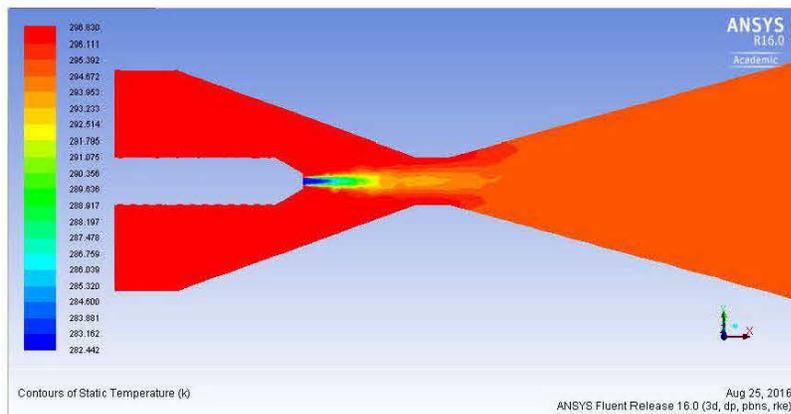
Figure 68: XY plane for static temperature at NXP 72, 60 and 48

5.3.5   Comparison of CFD results with experimental values

The comparison of CFD results with experimental results are resumed in Table 28,

Table 28: Numerical results comparison

Parameters	NXP, Nozzle Exit Position						Units
	72		60		48		mm
Type of test	Laboratory	CFD	Laboratory	CFD	Laboratory	CFD	n/a
Pressure	98495		98434		98272		Pa
Drop pressure eductor	29		21		15		Pa
Mass flow rate of nozzle	0.002405	0.002405	0.002404	0.002404	0.002404	0.002404	kg/s
Secondary mass flow	0.0147	0.0110	0.0136	0.0115	0.0122	0.0091	kg/s
Eductor mass flow ratio	6.1306	4.5717	5.6668	4.7849	5.0786	3.7496	
Temp of inducted air	23.5	23.5	23.6	23.6	23.7	23.6	°C
Temp of mixed air	22.41	22.1	22.44	22.15	22.42	22.08	°C
Temperature difference Mixed Air	1.40%		1.31%		1.54%		%

The CFD results presented in Table 28 shows less than 0.35°C difference between the predicted temperature induced and the mix for the experimental work and the CFD simulations for the eductor as whole. This consistency in the results suggests that the CFD simulations for the mine scale model will be realistic.

5.3.6 Motive nozzle performance verification

The complexity of the eductor and its specific different constraints during the experimental validation were responsible for the discrepancy. This disparity has further implications. In order to validate the experimental work additional CFDs were required one from the geometry testes at the lab and other for the rocket nozzle used in the laboratory experiment.

The CFD results presented in Table 28 shows less than 0.35°C difference between the predicted temperature induced and the mix for the experimental laboratory work and the CFD simulations for the laboratory scale eductor as whole. This consistency should lead to an increase in confidence in the results of the same CFD methodology applied to mine scale.

In the case of the rocket motive nozzle, the convergence was verified as in chapter 4.

In Table 29 the numerical values from the surface integrals obtained using Fluent Ansys are presented.

Table 29: Numerical values

Parameters	Jet inlet	Outlet	Units
Static pressure	489984.49	0	Pa
Velocity magnitude	2.12	135.12	m/s
Static temperature	296.28	286.83	K

In Figure 69, illustrate the static pressure, velocity magnitude and static temperature respectively.

Figure 69: XY plane for rocket motive nozzle

From the observations in chapter 6, the efficiency of the nozzle was 5.62%, a really low value. According to these results, the hypothesis about recirculation or vortices is rejected. The numerical results presented a nozzle efficiency of 7.82%, close to the percentage predicted in chapter 6.

Looking closely at Figure 69, an important issue can be identified, a shock wave in the nozzle, which was presented in chapter 4. Due to this situation, a fast new nozzle experiment, as explained in chapter 6, was performance. Figure 70 shows the thermal picture.
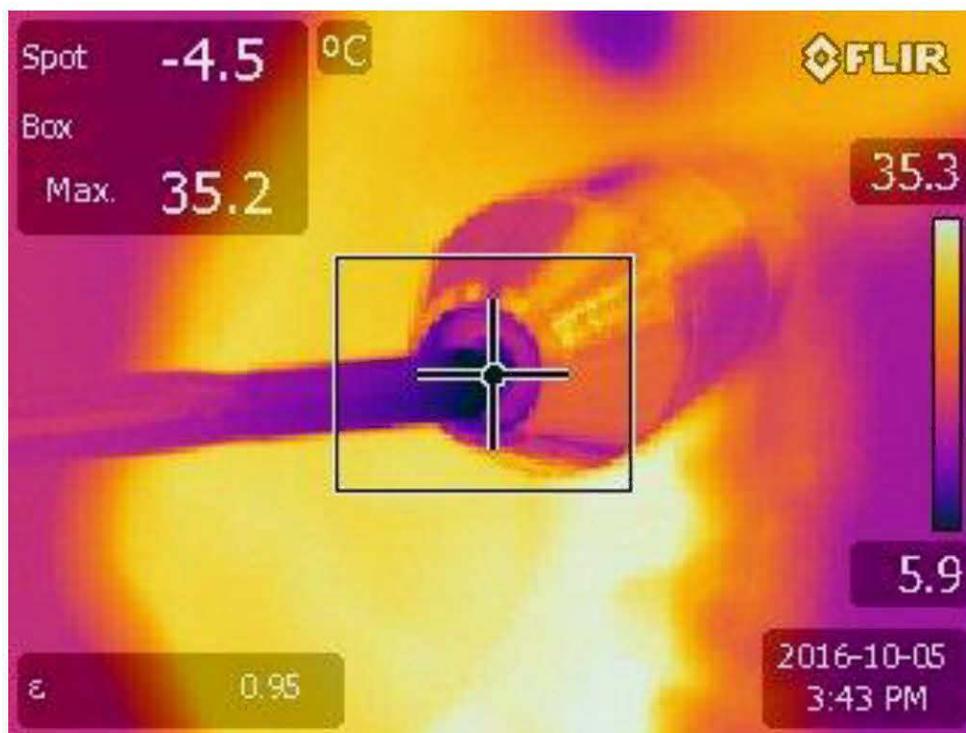
Figure 70: Thermal image for 11 bar gauge

The pressure of the compressor was increased at 11 bar gauge. The same nozzle produces a much lower free jet temperature, difference of 40°C but after verifying the flow pattern, shock waves still occur in the free jet. This is consequence of the rocket

nozzle, since its operating point is not 11 bar is closely 100 bar, therefore the rocket nozzle is operating very off design.

An alternative nozzle was design using the nozzle equations from chapter 4, to compare the performance with the rocket nozzle and validates the original nozzle efficiency assumption.

In Table 30 the numerical values from the surface integrals obtained using Fluent Ansys are presented

Table 30: Numerical values for new nozzle design

Parameters	Jet inlet	Outlet	Units
Static pressure	489986.21	11553.27	Pa
Velocity magnitude	2.00	462.26	m/s
Static temperature	296.28	189.24	K

The same procedure was used as for the rocket nozzle. Figure 71, illustrate the static pressure, velocity magnitude and static temperature respectively.
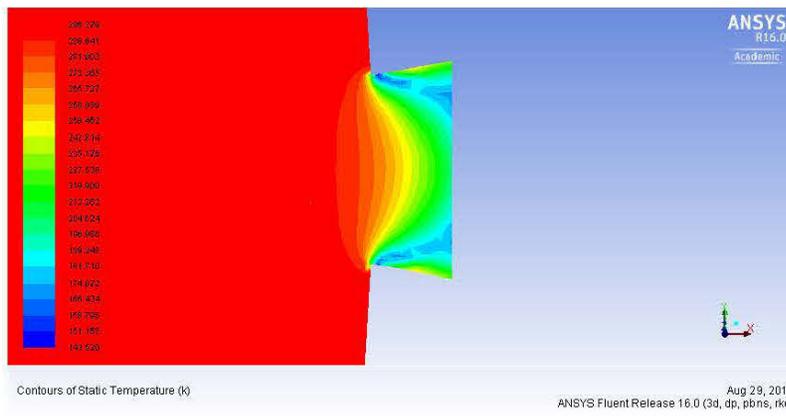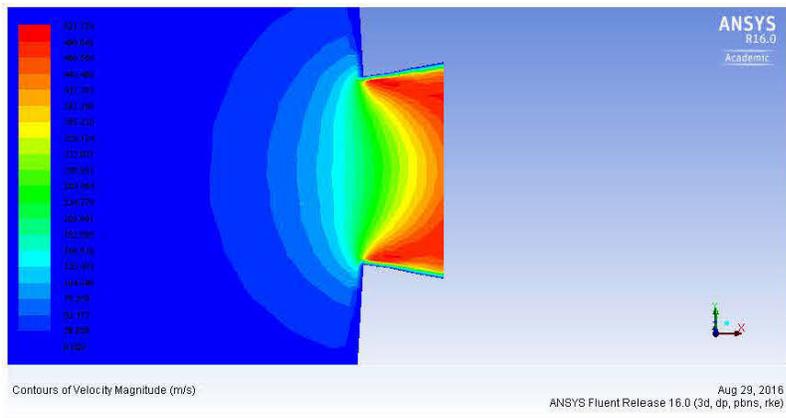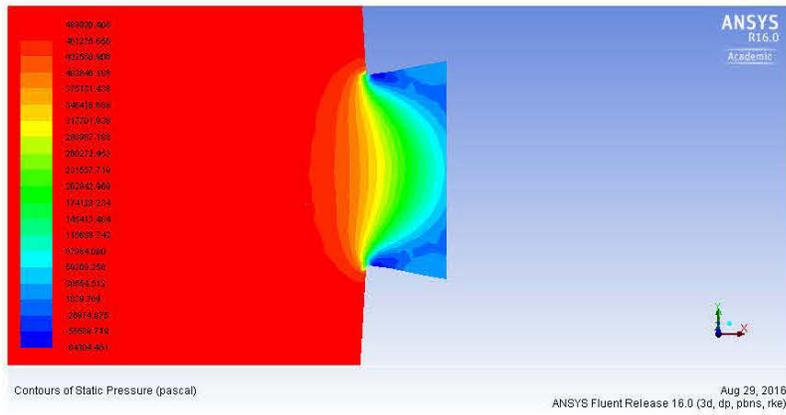
Figure 71: XY plane for alternative motive nozzle

In this case, the numerical results presented a nozzle efficiency of 97.25%, however after verification of the flow pattern a shock wave in the jet were discovered.

5.4 Discussion

In this chapter has been shown a short description of how to model the ejector lab scale in CFD. It was explained the settings, boundary conditions and constraints. The assumptions made, following the results from nozzle design in chapter 4, have determined the boundaries for the CFD model. The results obtained show the impact of the nozzle diameter in the outlet temperature and entrained mass flow

Overall, the nozzle is the most important part in the eductor. This chapter, probes the necessity of further study to optimize the eductor according to the design conditions and verify the flow pattern in advance to obtain an optimal performance.

In the next chapter, the experiment will carry out to validate the mine scale cooling ejector CFD results. Several parameters and settings applied in the simulation need to be verify in order to trust the results.

CHAPTER 6

CFD SIMULATION OF A MINE SCALE COOLING EJECTOR

6.1 Introduction

The models reviewed in chapter 4 for ejector performance only approximate interactions between boundary layers, shock waves and mixing. Computational Fluid Dynamics (CFD) is a reasonably low cost tool to obtain more accurate representation of the expected ejector performance. In this chapter an outline description of the CFD software and model will be presented and prior experience from the literature will be reviewed. Following this, the CFD campaign undertaken to characterize the performance of a mine scale cooling ejector coupled to a mine ventilation system presenting specified resistance to flow is described. Although presented earlier in the thesis, CFD simulations with the purpose of verifying laboratory scale ejector experiments, follow the same CFD methodology as described in detail, in this chapter.

6.2 Review of CFD simulations of ejectors

Most ejector studies base their ejector geometry upon results in documents: ASHRAE (1969) and ESDU (1985). Both documents provide information for the design and performance evaluation of ejectors. Since in the ejector sonic velocities and higher occur, the design process is complex as the behavior is not always obvious.

Riffat et al., (1996), in his study of computational fluid dynamics applied to heat pumps incorporating ejectors illustrated the capability of CFD to identify the most

favorable ejector design, and highlight the importance of position and type of motive nozzle for optimum ejector efficiency, however the compressibility was not considered. Smith et al., (1997), used CFD to design low-pressure ejectors with an accuracy of 80% in comparison with experimental results.

Bartosiewicz et al., (2005), reported on numerical and experimental investigations of supersonic ejectors using the k–omega–sst model. Rusly et al., (2005), undertook CFD analysis of an ejector in an ejector cooling system, validating Huang et al., (1999) results.

Bartosiewicz et al., (2006), in their numerical assessment of ejector operation for refrigeration applications based on CFD, reveal the importance of the selection of the turbulence model for optimum results. Pianthong et al., (2007), in their investigation for improvement of ejector refrigeration systems using CFD, incorporate the 'operation conditions' effect. Sriveerakul et al., (2007), carry out a prediction of the performance of a steam ejector using CFD for critical back pressure and entrainment ratio. Zhu et al., (2009), numerically investigated the geometry parameters for the design of high performance ejectors, concluding that the convergence angle and position of the motive nozzle depends on the specific operational conditions. Li et al., (2012), studied the configuration dependence and optimization of the entrainment performance for gas-gas and gas-liquid ejectors, where the effect of the motive nozzle position can improve the performance of mixing in the ejector throat. Lin et al., (2013), carried out a numerical investigation of geometry parameters for pressure recovery of an adjustable ejector in a multi-evaporator refrigeration system that revealed the importance of the length of the constant-pressure mixing section and the angle of the divergent nozzle for the adjustable ejector. Hakkaki-Fard et al., (2015), show a computational methodology for ejector design and performance maximisation, concluding that the motive nozzle and its position determines the performance.

6.3 Outline description of Fluent

CFD affords a more detailed representation and understanding of the hydrodynamics of the ejector. Capabilities to handle complex geometries and detailed mathematical models for transfer phenomena make its applications in a multitude of analyses and problems possible. Importantly accurate turbulence and near-wall models permit the inclusion of the effects of buoyancy and compressibility; heat transfer including mixed, forced and natural convection, and finally the effects of radiation for combustion. Based on the Navier-Stokes equations and a numerical approach with finite volume method, Ansys Fluent solves momentum, energy and species conservation equations when heat transfer, compressibility and mixing-reactions are involved. Turbulence is approached with a modification of the governing equations to solve the effects of the mean flow. In the case of the time averaged approach used in this study, more terms will appear in the Navier-Stokes equations; the Reynold stress terms become present to compensate for the turbulence effects.

The Reynolds-averaged approach to turbulence modeling requires that the Reynolds stresses are appropriately modeled. Different approaches to estimate the Reynold stress are available:

1) In the Spalart-Allmaras model, only one additional transport equation (representing the turbulent viscosity) is solved;

2) In the k-ε and k-ω models, two additional transport equations are involved (one for the turbulent kinetic energy, and a second either for the turbulence dissipation rate, or the specific dissipation rate). Turbulent viscosity is computed as a function of k and ε or k and ω. The advantage of this approach is the relatively low computational cost associated with the computation of the turbulent viscosity for the Reynold stress. Alternative models are available to represent the turbulence. However, according to

Hart, (2002), Ablwaifa, (2006), Chen, (2008) and Maqsood, (2008) the k-ε Model is the best option to simulate refrigeration ejectors.

6.3.1 Mesh settings

To solve for the flow within a given spatial domain according to the conservation equations, a computational mesh requires definition. This mesh utilizes a great number of nodes forming finite volume cells, upon which the stability accuracy, quality of the results depend. The size and position of the cells is determined by the flow gradients. In the simulations of this work, a quadrilateral mesh was used since it is reported (Ansys Inc, 2014) to generate a high quality mesh and can align well with the main flow direction. In the Advance Sizing Mesh setting, two types were used. The mine scale mesh, proximity and curvature sizing of mesh elements was chosen, due to its flexibility. In the laboratory scale simulations some constraints were introduced because of the small size of the physical object and the need to anchor the jet pipe. The proximity and curvature sizing method occasionally created irregularities in the mesh, so for this CFD model the Curvature Advance Size option was chosen.

The solution method used to resolve the discretized equations was the Fluent 'coupler solver'. The main reason for this is that for steady state flows, the 'couple solver' achieves a more robust and accurate solution for compressible flow problems using an explicit approach than other solvers. This approach maintains solution stability and enables faster convergence.

Fluent approximates the differential equations, based on the finite control volumes (explained in chapter 3). A discretization method is used for these purposes whereby Fluent applies the second order upwind difference scheme, based on truncated Taylor

series expansions. This implies that the numerical solution may be mesh dependent and so dedicated testing methods are required, especially for large grids. Due to the importance that a coarse mesh may ruin numerical exact solutions, complementary settings in Fluent have been used in this study to ensure a mesh independent solution and assure proper convergence, such settings include under-relaxing factors, use of multi-grid techniques.

6.3.2   Ejector Simulation approach

In this case, the simplified largely analytical models of ejector performance were used to estimate the expected behaviour for the ejector as design guidance.

Frequently, experimental data are obtained to verify the CFD code, the operating conditions used to validate the CFD model are obtained in advance by experimental data. As the mine-scale application of ejector theory is a concept never tested. In practice prior experimental data doesn't exists. Using the data from the review literature in chapter 3, the operating conditions can be approximated as a starting point for CFD and to initialise some parameters. After validating the code, different operating conditions can be simulated taking into account the turbulence model. The turbulence model ought to be calculated in advance to introduce into the system the turbulence intensity and the hydraulic mean diameter required for the simulation. To verify the model, 3000 iterations were set, to be sure about the stability and accuracy of the model.

The errors, the code and the calculation must be evaluated. In this case, three different parameters were used to evaluate simulation output.

1) Two virtual surface monitors were set to control the solution, i)a mass weighted average static pressure and ii) a static temperature;

2) Checks were made to ensure that the secondary mass flow was positive at the inlet (i.e. inflowing), hence the total mass flow was negative at the outlet and equal to the sum of primary and secondary flow;

3) The residual errors or so-called convergence criteria parameters, had to be at least 10^{-4} order of magnitude to define as the steady state.

Some of the studies that will be presented in the next section, predict shockwaves inside of the ejector suggesting that simulated chamber pressure is too low, although the flow may still be chocked. For the mine-scale model, simulations are for 2.5 km deep conditions; nozzle and eductor performance. These reflect nozzle back pressure typically higher than atmospheric free air at surface. For safety reasons, noise and vibration must be minimised in the mine environment. This means whenever possible running off the design point must be avoided because under or overexpansion will cause this vibration. Consequently, in the mine-scale model this has been taking in consideration, by ensuring velocities are low where personnel may be present to avoid Mach speed.

6.4 Mine-scale ejector set up and orientating simulations

Following ASHRAE (1969), ESDU (1985), previous studies named before a first geometry for the mine-scale ejector was defined. Since the design software Inventor has the capability to link an Excel document and update the geometry, so for simplicity a parametric Excel spreadsheet linked was created.

Although the motive nozzle did not feature in the simulations, the jet issuing from the motive nozzle was included through the prescription of mass flow, pressure and

temperature boundaries at the motive nozzle exit. These values were obtained from the results of chapter 4. A gauge pressure boundary condition of 0 Pa was defined at the gallery inlet, a pressure assumed shared by the motive nozzle outlet. At the ejector outlet, a gauge pressure boundary of +1000 Pa was set. Mass flow at gallery inlet and outlet were the principal free variables determined through relaxation in the CFD analysis.

Table 31: Boundary conditions for inlets and outlet in the CDF simulation

Parameters	Unit	Jet	Gallery	Outlet
Mass flow	(kg/s)	22.36		
Temperature	(K)	283.15	312.15	
Pressure gauge	(Pa)	0	0	1000

The operation pressure is 140325 Pa (calculated by autocompression), in other words the pressure in the gallery and jet is 139325 Pa. The turbulence intensity and hydraulic mean diameter used in each simulation was re-calculated when the boundaries conditions changed.

Initially being guided by experience reported in the literature, fifteen simulations were completed varying the position and diameter of the motive nozzle throat, suction chamber, mixing chamber, diffuser angle and extra length to find a workable model. The approach principally aimed to discover the effect of the motive nozzle position along the ejector axis on the entrained flow. The values of the first stable geometry are reported in Table 32 and illustrated in Figure 72.

Table 32: Geometry parameters for the first stable simulation

Parameters	Value	Unit
Nozzle diameter	101.6	mm
Mixing diameter	1000	mm
Extra diameter	4000	mm
Throat diameter	101.6	mm
Suction diameter	4000	mm
Nozzle length	4000	mm
Throat length	4000	mm
Suction length	2000	mm
Mixing length	2000	mm
Extra length	20000	mm
Suction angle	170	deg
Diffuser angle	176	deg
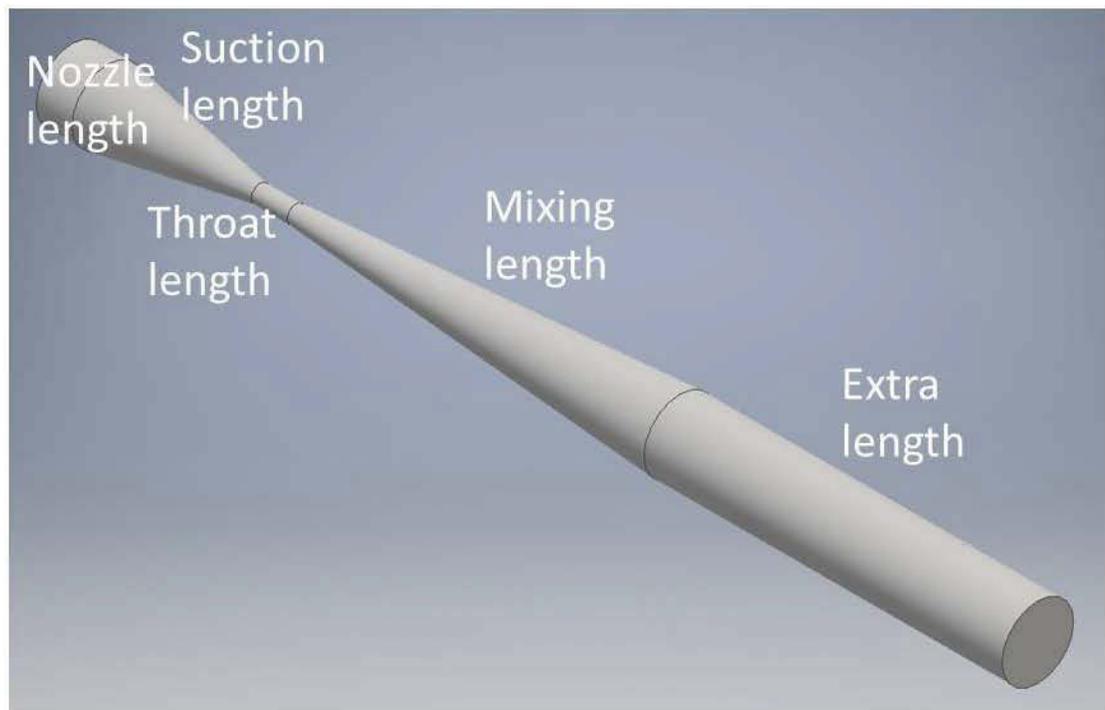
Figure 72: Ejector geometry in 3D

With this geometry a modification was applied, the nozzle exit position in the computational domain was reduced to 2000 mm, in order words, the nozzle was retracted. Less secondary mass flow entrained from the gallery was obtained. Then, the simulation with 4000 mm nozzle exit position was repeated but with the temperature from the jet was set 201.83 K, the temperature predicted from motive nozzle analysis of chapter 3.

Results from this model also gave satisfactory results. The next step was to improve the moving away from a curvature defined mesh toward a as proximity and curvature mesh, known to produce more accurate results. Since a huge turbulence viscosity was noticed. Some modifications on the mesh were done. The solution found, it was the adaptive mesh refinement, which reduces the numerical error in high-gradient regions with minimal numerical cost and without changing the initial settings. This dynamic gradient adaptation, reducing coarsen and refine threshold, and the increased in the maximum turbulence was perform. The results converged perfectly. After this result, a nine cases matrix was performed. In the next section the data will be explained.

6.5 CFD simulations varying motive nozzle and mixing section diameters

The different nozzle diameters were chosen according to available pipe options for the HAC delivery. In the case of the mixing chamber, the diameter was defined by the lesson learned during the simulations and the literature on ejector design (ASHRAE, 1969), (ESDU, 1985). Table 33 compiles the results of simulations with geometry and boundary conditions given by X and Y, while motive nozzle diameter ranged and mixing chamber diameter ranged. These values were obtained from the simulation

results through integrated over defined planes and surface integrals at 22.36 kg/s of initial mass flow for the primary nozzle.

Table 33: Entrained mass flow and eductor outlet (mixed) air temperature for an inlet secondary air temperature of 312.15K and a pressure rise of 1000Pa across the eductor

Parameters			Mixing Chamber Diameter (m)			Mixing Chamber Diameter (m)		
			0.75	1	1.25	0.75	1	1.25
			Entrainment mass flow (kg/s)			Outlet temperature (K)		
Nozzle Diameter (in)	4	(101.6 mm)	93.17	188.29	298.54	290.78	300.38	304.33
	6	(152.4 mm)	76.25	159.91	243.83	278.12	298.57	302.79
	12	(304.8 mm)	19.55	51.41	71.25	253.29	278.7	285.79

The data from the nine cases is shown in Appendix A where it can be observed the solution has converged in each case, according to the residuals limits, the mass weight averaged temperature and pressure and the total mass flow. Additionally some gradient adaptations were needed since in some cases coarsen and refine threshold were too tight.

The observations for the CFD simulations showed the increase of mass flow and temperature as the mixing chamber diameter increased for the same nozzle diameter.

In next page, one example for static pressure, velocity magnitude and static temperature of the nine cases is illustrated. The complete sets of contour graphics, created by defining an XY plane surface in the direction of the flow, are presented in the Appendix A as well.
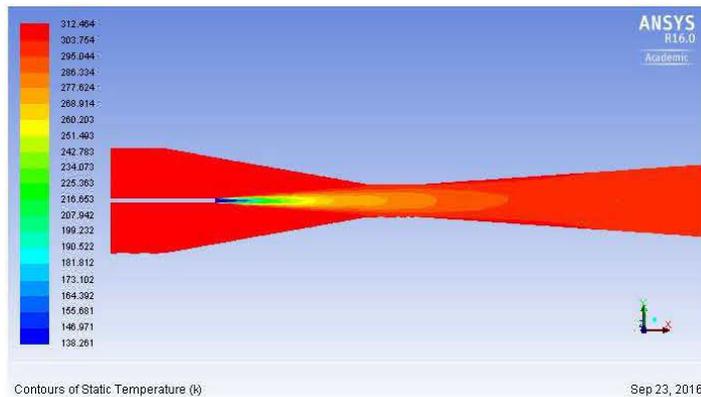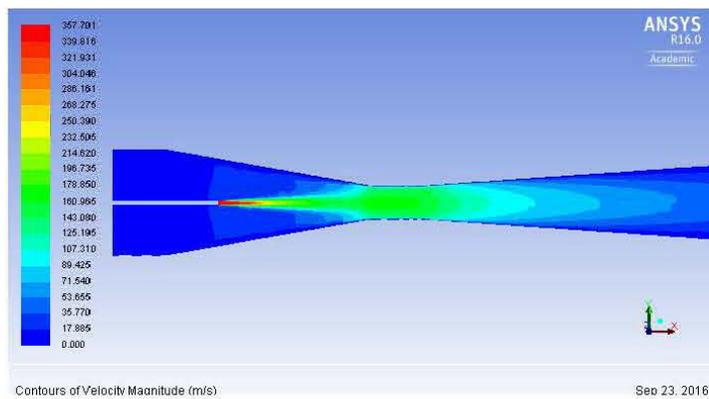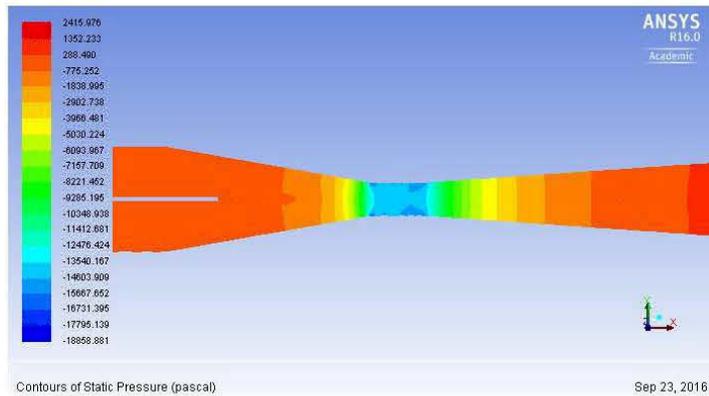
Figure 73: Cross sectional plane XY for static pressure, velocity magnitude and static temperature (Nozzle diameter 152.4 mm, 1.25 m mixing chamber) for intake secondary air temperature of 312.15K and pressure rise across ejector of +1000Pa

In Figure 74 and Figure 75, the outlet temperature and entrainment mass flow is plotted against the mixing chamber diameter. In the temperature chart, 101.6 mm and 152.4 mm are close in values. In the case of the mass flow, the 101.6 mm pipe looks superior.
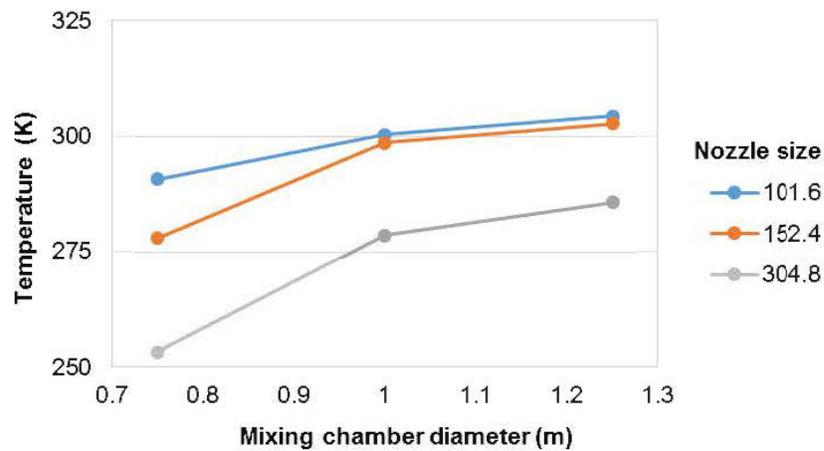
Figure 74: Parametric investigation: temperature-mixing chamber diameter
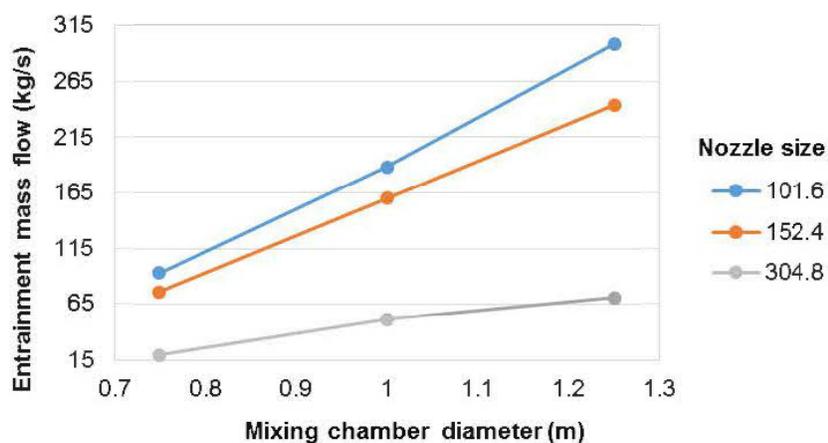
Figure 75: Parametric investigation: entrainment mass flow-mixing chamber diameter

However, the velocity inside the mixing chamber in the 101.6 mm pipe is much bigger, in any case, that the 152.4 mm pipe, for that reason after the nine simulations, the nozzle diameter 152.4 mm and 1.25 m mixing chamber were chosen as the operation point for its mass flow, low temperature and velocity than the others. Having in mind the use of a common diameter pipe for mining purposes with maximum entrained flow and low outlet temperature.

6.6 CFD simulations varying the motive nozzle mass flow rate and the pressure across the ejector

From these results, another nine simulations were made to create 'fan curves' for the ejector and be able to compare them later with real fans, explained in detail in the next section.

Following the observations in chapter 4 with different nozzle diameters simulated, the operating point of the ejector was defined and used to model the mine scale model.

It is known, a priori, precisely what pressure will be developed across the ejector, because this pressure will be governed by the mine resistance to air flow ' seen' by the ejectors, in the same way as the pressure developed by a fan depends on the resistance that it is connected to.

The mine scale model, an underground gallery of 4 meters diameter and 32 meters long, with a convergent initial section, containing a 6 inch pipe delivering a compressed air jet, sent to a narrow throat and subsequently to a divergent, pressure recovering section. The design is supported by thermodynamic calculations. Inlet, secondary air flow is assumed to be at 39 °C reflecting the temperature of air that must be cooled.

The air jet comprises a mass flow of 22.36 kg/s at -71.32 °C. A 1 kPa static pressure rise is maintained from the inlet to the outlet (at the diffuser exit) where the mass flow of the air is 243.82 kg/s (including the secondary air flow) at 29.02 °C. As the air comprising the jet is drier than the secondary air flow, through the mixing process, the humidity of the air is reduced too. In short, the system behaves like a dehumidifying, cooling, booster fan.

Consequently, the values above are recomputed with varying pressure maintained across the arrangement (500, 1500, 2000 Pa). The entrained mass flow varies for each pressure rise maintained so that taken together the data form a curve describing how the pressure rise developed varies with mass flow which is similar to a fan curve. The actual operating point of the ejector will depend on where the system resistance characteristic curve crosses this curve. Three curves resembling a 'fan curve' were obtained, as illustrated in Figure 76.
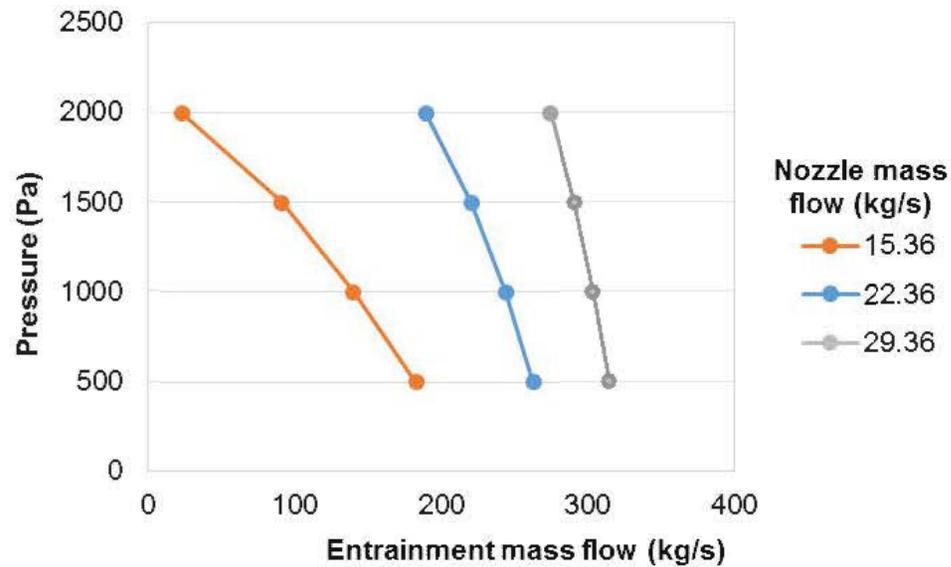
Figure 76: Parametric investigation: Fan curves

A flow rate regulator can be installed on the delivery line supplying the motive nozzle. With this control deemed to be in place, a family of ejector 'fan' curves emerge. There curves are akin to those that results when the speed of a conventional fan is adjusted, or the pitch of the blades on an axial flow fan is adjusted.

Further simulations with air jets with mass flows of 15kg/s and 29 kg/s are presented in Table 34, to create a suite of fan curves for mine ventilation design purposes. The goal of those simulations was to create different possible scenarios for a mine and finally compare the performance of the ejector with a mine fan.

Table 34: 'Fan curves' according to the primary mass flow and pressure increase

Parameters		Pressure (Pa)			
		500	1000	1500	2000
		Entrainment mass flow (kg/s)			
Nozzle Mass Flow (kg/s)	15.36	183.09	140.27	91.55	23.75
	22.36	262.74	243.83	220.74	189.46
	29.36	314.59	303.43	291.03	274.64
		Outlet temperature (K)			
Nozzle Mass Flow (kg/s)	15.36	303.56	301.23	296.28	268.86
	22.36	303.39	302.79	301.93	300.45
	29.36	302.58	302.28	301.91	301.38

From the observations, it is possible to form a judgment of the results. First, the mass flow always decreases with the rise in pressure for any operation point. Second, if the pressure is 500 Pa the temperature increases inversely proportional to the mass flow. Third, the optimum pressure operating point will depend on the needs of mass flow, cooling temperature and resistance to the system is connected. Over 1500 Pa, the cooling capacity is better but as expected the mass flow fall considerably.

In next page, one example for static pressure, velocity magnitude and static temperature of the nine cases is illustrated. The complete sets of contour graphics, created by defining an XY plane surface in the direction of the flow, are in the Appendix B.
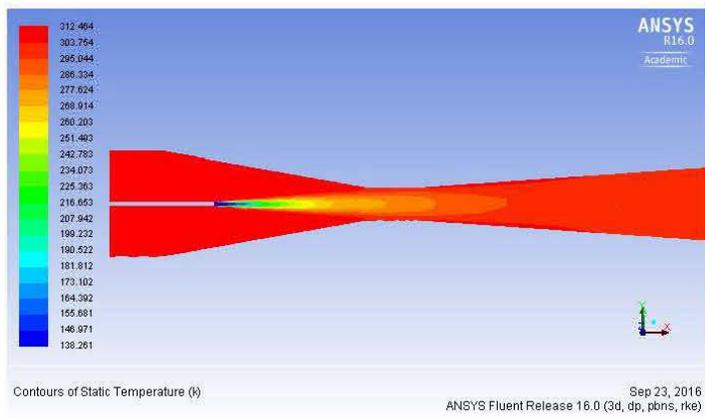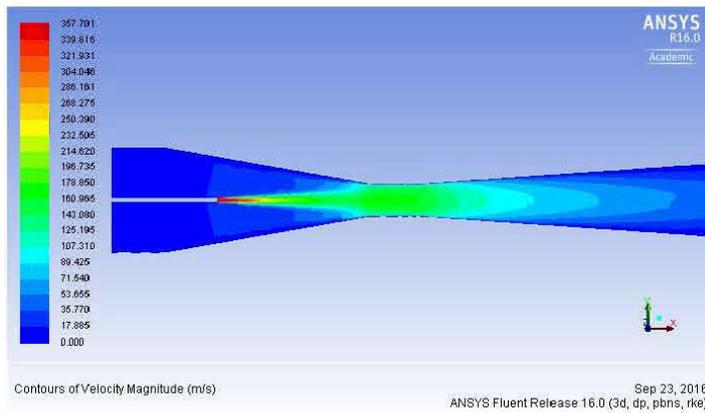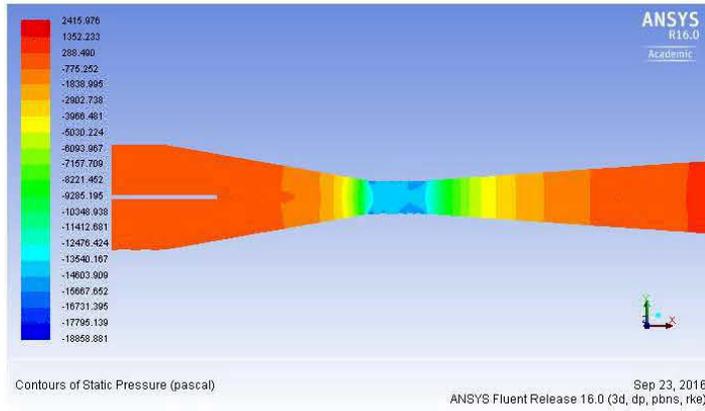
Figure 77: Cross sectional plane XY for static pressure, velocity magnitude and static temperature (mass flow 22.36 kg/s, Pressure 1000 Pa)

6.7 CFD simulation varying the motive nozzle position

A modification to the nozzle-throat length was applied reducing to 2000 mm, in order words, the NXP position changed. Less mass flow from the gallery was obtained. In order to verify with the operation point chosen, other three simulations were done with the nozzle-throat length 2000 mm and 6000 mm, as illustrated in Table 35.

Table 35: Mass flow and temperature according to the nozzle position

Parameters		Nozzle length (mm)		
		2000	4000	6000
Mass flow (kg/s)	22.36	Entrainment mass flow (kg/s)		
		186.56	243.82	231.3
		Outlet temperature (K)		
		300.28	302.17	302.34

In Figure 78 and Figure 79, the temperature and mass flow is plot against the nozzle length. In the temperature chart the nozzle length of 2000 mm got better performance, but in the mass flow 4000 mm nozzle length position is superior: Since the goal of the ejector is to entrain as much mass flow as possible keeping the temperature low, the optimum position for these operating conditions should be 4000 mm. The complete sets of contour graphics, created by defining an XY plane surface in the direction of the flow, are in the Appendix C.
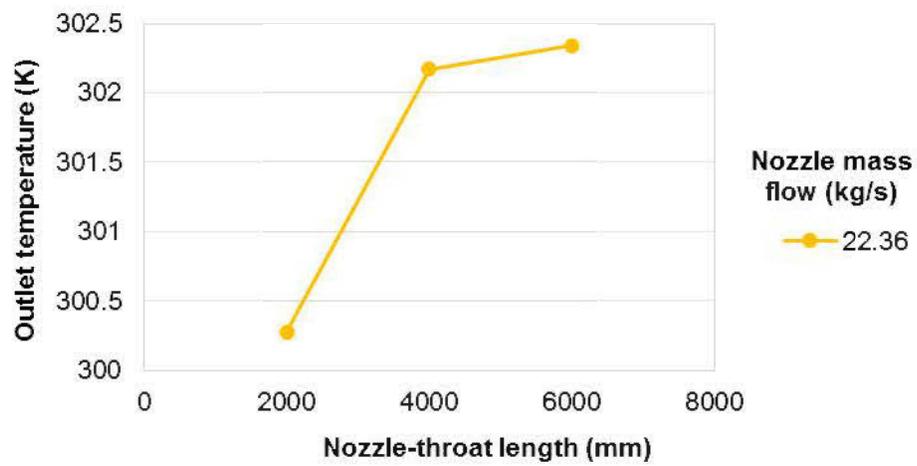
Figure 78: Parametric investigation: Temperature-Nozzle length
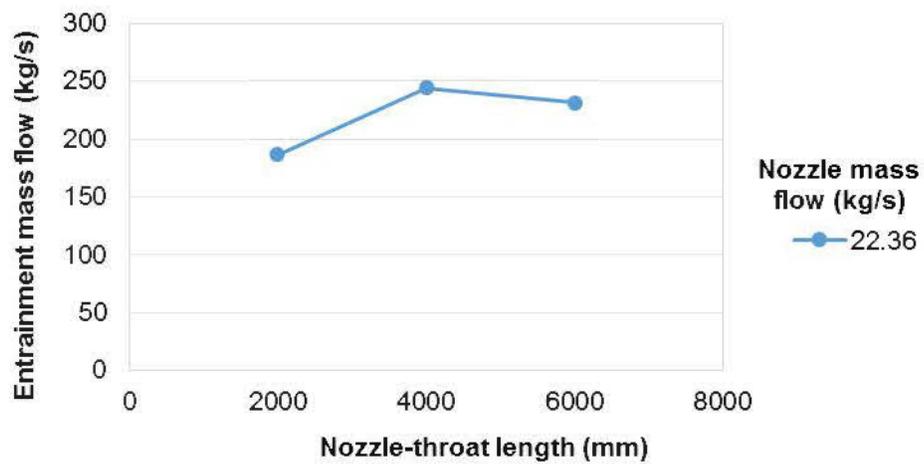
Figure 79: Parametric investigation: Mass flow-Nozzle length

In Figure 80 are illustrated the three nozzle exit positions or nozzle-throat length.
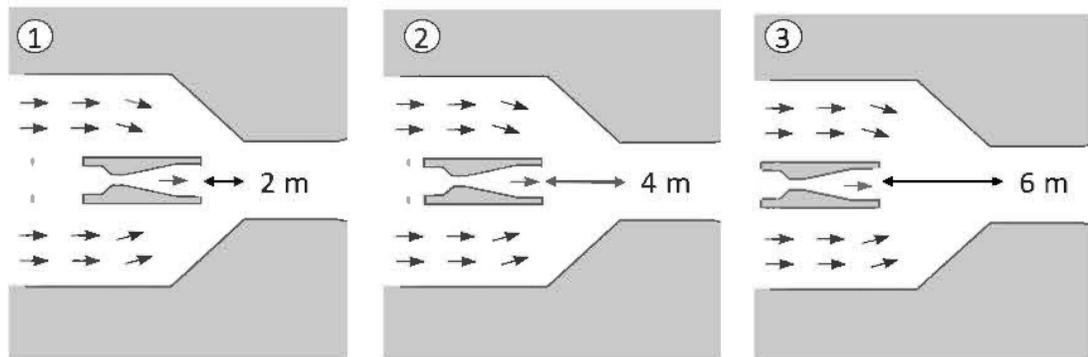
Figure 80: NXP for the ejector

6.8 Discussion and conclusion

In this chapter has been shown a full description of how to model an ejector in with CFD. It was explained the settings, boundary conditions and constraints.

The assumptions made, following the results from nozzle design in chapter 4, will determine the boundaries for the CFD model. The results obtained show the impact of the nozzle diameter in the outlet temperature and entrained mass flow. Using multiples mass flows discovered the capability of the ejector to work as a booster fan. Finally the exit position of the nozzle has a direct impact on the final performance of the ejector.

In the next chapter, a full discussion of the results will be developed.

CHAPTER 7

RESULTS AND DISCUSSION

This chapter presents discussions relating to the ejector design, CFD results, experiment findings and implications for cooling sub-surface.

7.1 For the lab scale ejector, experimental results and CFD results qualitatively agree

It was important that all the ejector performance experiments were conducted in steady state compressor operating conditions. This was to ensure that the ejector can deliver the same back pressure along the system. Additionally, the motive nozzle pipe had to be level and aligned at the beginning of each experiment to avoid more turbulence and extra friction losses. Because of the economic, time and space constraints in using the 3D printer, the model tested could not be as optimal as the mine scale one. Some of the findings, due to these constraints are described below:

1. The greater potential for inaccuracy in the nozzle efficiency might arise from the assumption that the rocket motive nozzle delivery pressure was 4.5 bars. The minimum temperature reported in Figure 36 was utterly out of the

expected temperature at the motive nozzle exit. In addition, the results were verified using the equations in chapter 4. The final nozzle efficiency was 4.42% as presented in chapter 4. However, the discrepancy still existed; extra discussion will be introduced further in the text.

2. The inherent imprecision of the instrumentation could emerge from the actual range to measure. In particular, the thermometers. These mercury thermometers have a precision of 0.5°C. This resolution was assumed enough, due to fact that CFD results the decrease temperature expected was around 10°C. According to the data presented in Table 24, the actual temperature difference between the induced and the mix is maximum 1°C. Some of the values measure during the experiment were photographed and then scaled to obtain as much accuracy as possible. This represents a potential error on the final experimental results because of the instrumentation resolution.

3. The field test bore out the approach and give further consistency to the results. Emphasizing the critical impact of the nozzle in the total efficiency of the ejector.

7.2 For nozzle sizes and scales analysed, predictions from the CD nozzle simulation tool were consistent with observations

The functionality of the ejector relies on the motive nozzle having the optimum geometry. This characteristic depends upon the angle of the divergence section, which should be kept below 20 degrees to avoid separation of the mass flow. The simplistic and logical approach to the motive nozzle design that is described in chapter 4 is shown to be a satisfactory method. However, due to the fact that the nozzle efficiency depends also on the operating conditions, the actual performance will deviate from the perfect

solution. A further consideration of this discrepancy is deeply discussed in the next sections.

7.3 *As motive nozzle cooling, and ejector performance have been verified at small scale, the CFD results for mine scale performance are supported*

The CFD results have shown the capability of the CFD to be an effective tool for simulating the ejector. It is evident as well, that the CFD ought to be conscientiously optimized to obtain sensible results. Previous studies had shown that the predicted operational performance can differ around 30% of the numerical parameters. Normally the operating conditions used to validate the CFD model are obtained in advance by experimental data. In this work, the approach is different because the mine scale application for the ejector was a concept never tested. Therefore, there is not previous experimental data. So using the data from the numerical approach in chapter 3, the operating conditions were simulated.

To verify the model 3000 iterations were set, to be sure about the stability and accuracy of the model. Moreover, the errors, the code and the calculation were evaluated. In this case, three different parameters were used to evaluate it: 1) Two surface monitor were set to control the solution, a mass weight average static pressure and temperature; 2) checking the secondary mass flow was positive at the inlet, hence the total mass flow was negative at the outlet and equal to the sum of primary and secondary flow; 3) the residual errors or so-called convergence criteria parameters, that should be at least 10^{-4} order of magnitude for the steady state. Last, in the majority of studies presented in chapter 3, they deal with shockwaves inside of the ejector. This work had a different approach in this subject because the mine scale model is simulated for sub-surface conditions.

Since the prediction worked, the next step was to improve the mesh. The solution found it was the adaptive mesh refinement, which reduce the numerical error in high-gradient regions with minimal numerical cost and without changing the initial settings. This dynamic gradient adaptation, which reduces coarsen and refine threshold, therefore the increased in the maximum turbulence was perform. The results converged as expected.

The simulations performed; helped to understand the influence in the behavior of the eductor and its critical parts. It is clear from the CFD results that the mine scale ejector can cool the sub-surface. This is evident from the data presented in Figure 81 where the matrix nozzle-mixing diameter shows 7.82K to 58.86K of temperature reduction from the gallery at initial temperature of 312.15K.
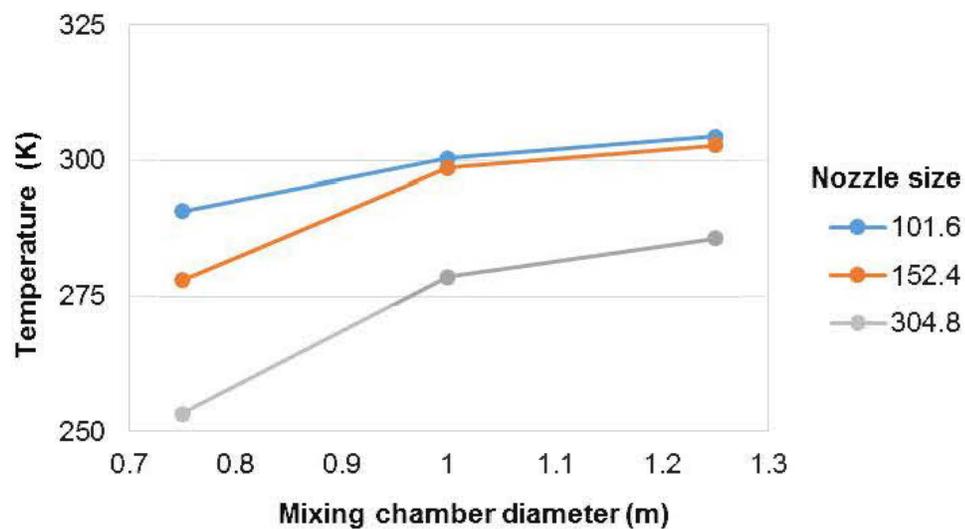
Figure 81: Cooling effect of nozzle size

Following the data presented in Figure 81, the mixing chamber diameter and the nozzle diameter have a direct impact in the temperature rise as well as the entrainment ratio. It is clear from both figures that the entrainment ratio would be better for an ejector with a mixing chamber diameter of 1m and a motive nozzle diameter of 101.6mm. Otherwise, the temperature decrease would be better for and ejector with a small mixing chamber, 0.75m, and a bigger motive nozzle diameter of 304.8mm. There are not studies about this correlation. In the case of the nozzle exit position, NXP, the optimum position for the motive nozzle is 4000mm from the mixing chamber. The best ejector performance is in this position where the entrainment ratio is maximum in comparison with the other two nozzle exit position. Additionally, the NXP can reduce the temperature at the same time for an optimum position. This could be cause by the shock loss and friction loss due to the contact of both turbulent flows. Previous studies such as (Zhu et al., 2009), shows the correlation between the optimum NXP and the entrainment ratio.

A potential further benefit of these results is the possibility to use the ejector as a fan. Following the data presented from the CFD results, it possible to recognize the pattern of a fan curve. The data presented in Figure 82 shows three fan curves developed by the ejector for typical pressures in mine fan installations for a pressure of 500 Pa, 1000 Pa, 1500Pa and 2000Pa; 218.95 m^3/s, 203.19 m^3/s, 183.95 m^3/s and 157.88 m^3/s respectively of entrainment flow at standard density 1.2 kg/m^3, proving this point.
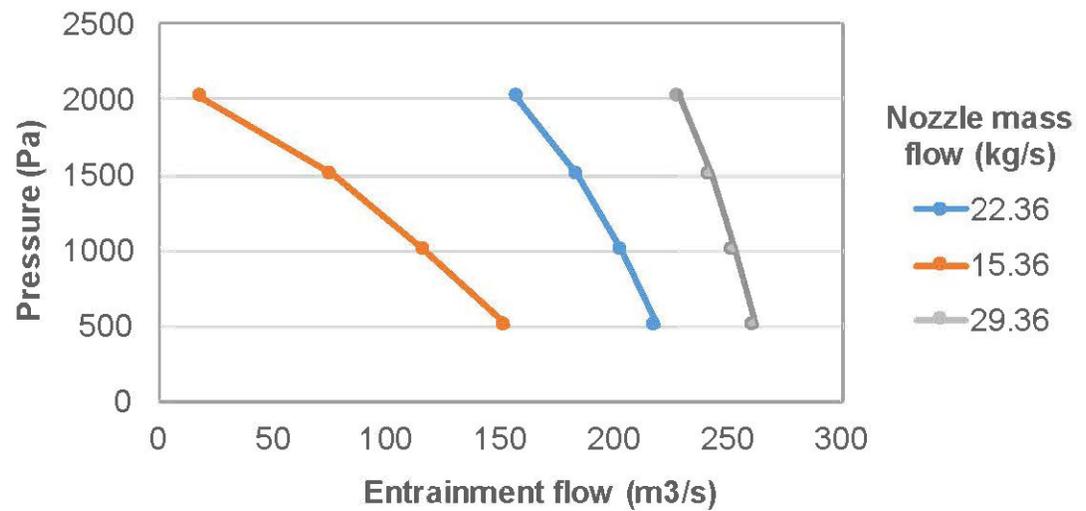
Figure 82: Fan behaviour of nozzle mass flow variation

Analyzing the data presented, the entrainment ratio increase for small pressures as expected for a fan. In addition, the decrease in temperature behaves as the mass flow, lower for higher pressures. As shown, the CFD results have probed the capability of the eductor to work as a fan, for different mass flows and pressures.

CHAPTER 8

CONCLUSIONS

In this chapter conclusions are presented relating to the research questions posed in chapter 1 and the additional findings. These conclusions are referenced to the current development status of the eductor and a summary of recommended further work is introduced.

8.1 Outline of the main findings of this work

This work started with the proposal of replacement of a turbo-expander with an ejector as the expansion device in the RBRC. The ejector has the potential to be a simpler, smaller, lower maintenance and potentially more economical solution and a third key variation step on the RBRC concept set out by Del Castillo. First, an analytical study based on the general governing equations to define the best thermodynamic model of ejector design. After defining the model, the expected performance could be taken into account, creating a comparison in design. This simple comparison showed the complexity of designing an ejector and how several geometric constraints may affect the performance, such as the position of the nozzle, the operation conditions, diameter and length of each component. Nevertheless, it has been possible to produce guidance for design of cooling ejectors. The optimum geometry depends on the operating conditions and specific function of the ejector. Then a comparison of thermodynamic conditions for a turbo expander and ejector, to conclude that

replacement of the turbo-expander with a nozzle in Del Castillo's concept will in no way diminish the low exit air temperatures that may be expected, providing nozzle irreversibilities can be minimized.

Consequently, more detailed analysis was presented. The pressure distribution along the nozzle and flow pattern were introduced to avoid the possibility of shockwaves inside the ejector. Four scenarios were explained, in different scales, showing the performance prediction and experimental performance with laboratory data. The entire methodology was explained in chapter 5 to develop a procedure for further research. Finally, the CFD was used to verify the laboratory scale and mine scale prediction. The latter, was able to verify the hypothesis of an ejector working as a booster fan (Appendix B) with several improvements (Appendix C).

A further question was raised at this stage regarding the relevance of the motive nozzle to the design of such ejectors. Clearly it is always necessary to have a rigorous understanding of the operational capabilities. However, the motive ejector performance varies according to the design. Designing an ejector with a performance motive nozzle should be the focus to achieve the necessary decrease in temperature a maximum entrainment ratio. A motive nozzle well designed will reduce the shock loss and improve the entire nozzle efficiency. This is demonstrate by the CFD results in chapter 5, where the nozzle efficiency from 7.82% to 97.25%. However the flow pattern must be verify always to avoid shock waves in the performance.

Further work is require to finalize the understanding of the ejector as a no moving parts solution for cooling deep mines, its operational capabilities and how nozzle can improve its performance.

These points are presented as follows:

1. A new design nozzle should be developed, verify by the flow pattern, tested at the laboratory and finally confirmed by CFD simulations.

2. A mine scale should be developed. However the geometric constraints may be studied, such as the position of the nozzle, the operation conditions, diameter and length of each component, to avoid shockwaves inside the nozzle or even on the free flow.

In summary, a no moving parts solution for cooling deep mines has been analyzed from a mine scale point of view. High attention has been paid to previous studies in refrigeration systems, in order to obtain a clear overview of the capabilities and expected performance. The reverse Brayton cycle and its possibility to be applied underground has been provided using an ejector. Deep understanding of the motive nozzle in the ejector has allowed verifying the experimental results. The use of a power tool such as Ansys Fluent has confirmed the consistency of the initial hypothesis, making realistic the approach for the mine scale ejector. Furthermore, the discrepancy on the nozzle efficiency can be turned into an advantage for future work as presented during the discussion in chapter 4, 5 and 6. The operating conditions must match the nozzle design-shape to achieve the desire effect and therefore an optimal performance. The design-shape due to be optimized according to flow pattern to obtain the high isentropic efficiency, with emphasis on the nozzle diameter and its position to maximize the entrained mass flow.

REFERENCES

Ablwaifa, A.E., 2006. A Theoretical and Experimental Investigation of Jet- Pump Refrigeration system, Ph.D Thesis, University of Nottingham.

ACGIH, 2013. 2013 TLVs® and BEIs® - Threshold Limit Values for Chemical Substances and Physical Agents and Biological Exposure Indices. (Source:http://www.ccohs.ca/oshanswers/phys_agents/hot_cold.html#_1_3/otm_ iii_4.html#iii:4_1).

Alexis, G.K., Rogdakis, E.D., 2003. A verification study of steam-ejector refrigeration model. Appl. Therm. Eng. 23, 29–36. doi:10.1016/S1359-4311(02)00116-3.

Allen, C., Morgan, J., Rantanen, E., 2012. Modular thermal transfer unit (MTTU) – Portable surface ice stope. Proceedings of the 14th U.S./North American Mine Ventilation Symposium 2012, Utah, US,.

Aly, N.H., Karameldin, A., Shamloul, M.M., 1999. Modelling and simulation of steam jet ejectors. Desalination 123, 1–8. doi:10.1016/S0011-9164(99)00053-3.

Ansys Inc, 2014. Ansys Fluent. Users Guide., Version 16.0, Ansys Inc., Canonsburg, PA, USA.

Aphornratana, S., Eames, I.W., 1997. A small capacity steam-ejector refrigerator: experimental investigation of a system using ejector with movable primary nozzle. Int. J. Refrig. 20, 352–358. doi:10.1016/S0140-7007(97)00008-X.

ASHRAE, 1969. Steam-jet refrigeration equipment. ASHRAE Guid. Data Book, ASHRAE, USA, Ch.13.

Atlas Copco, 2012. Delivering complete ORC solutions 16.

Auclair, A., 1957. Ragged chutes. Can. Min. J. 78 (8) 98e101.

Bartosiewicz, Y., Aidoun, Z., Desevaux, P., Mercadier, Y., 2005. Numerical and experimental investigations on supersonic ejectors. Int. J. Heat Fluid Flow 26, 56–70. doi:10.1016/j.ijheatfluidflow.2004.07.003.

Bartosiewicz, Y., Aidoun, Z., Mercadier, Y., 2006. Numerical assessment of ejector operation for refrigeration applications based on CFD. Appl. Therm. Eng. 26, 604–612. doi:10.1016/j.applthermaleng.2005.07.003.

Bidini, G., Grimaldi, C.N., Postrioti, L., 1999. "Performance Analysis of a Hy- draulic Air Compressor," Proc. Inst. Mech. Eng. Part A, 213(A3), pp. 191–203.

Cemič, L., Kleppa, O.J., 1987. High temperature calorimetry of sulfide systems. Phys. Chem. Miner. 14, 52–57. doi:10.1007/BF00311148.

Chen, J., Havtun, H., Palm, B., 2014. Investigation of ejectors in refrigeration system: Optimum performance evaluation and ejector area ratios perspectives. Appl. Therm. Eng. 64, 182–191. doi:10.1016/j.applthermaleng.2013.12.034.

Chen, Q., 2008. Performance of Air-Air Ejectors with Multi-ring Entraining Diffusers. University of Queen.

Davies, E., 1922. Air cooling plant, Morro Velho Mine, Brazil. Trans. Inst. Min. Engrs. . 63 SRC-, 326–341.

De Souza, E., 2015. Cost Saving Strategies in Mine Ventilation.

Del Castillo, D., 1988. Air cycle refrigeration system for cooling deep mines. Int. J. Refrig. 11, 87–91. doi:10.1016/0140-7007(88)90118-1.

Devenport, W., 2001. Nozzle Applet. [Online]. [Accessed 10 October 2016]. Available from: http://http://www.engapplets.vt.edu.

Domanski, 1995. Theoretical Evaluation of the Vapor Compression Cycle With a Liquid-Line/Suction-Line Heat Exchanger, Economizer, and Ejector. NISTIR 5606. Nistir 5606 1–37.

Eames, I.W., Aphornratana, S., Haider, H., 1995. A theoretical and experimental study of a small-scale steam jet refrigerator. Int. J. Refrig. 18, 378–386. doi:10.1016/0140-7007(95)98160-M.

El-Dessouky, H., Ettouney, H., Alatiqi, I., Al-Nuwaibit, G., 2002. Evaluation of steam jet ejectors. Chem. Eng. Process. 41, 551–561. doi:10.1016/S0255-2701(01)00176-3.

Elbel, S., Hrnjak, P., 2008. Experimental validation of a prototype ejector designed to reduce throttling losses encountered in transcritical R744 system operation. Int. J. Refrig. 31, 411–422. doi:10.1016/j.ijrefrig.2007.07.013.

ESDU, 1985. Ejectors and jet pumps, data item 86030. London: ESDU International Ltd.

GE, 2008. Turboexpander-Generators For natural gas applications GE has achieved a leadership position in the international oil and gas industry through constant improvements in the technology and effectiveness of its solutions . GE Global Research facilities in Nor.

Grenier, M., Gangal, M., Young, D., Butler, K., Edwardson, E., Feres, V., 2000. Evaluation of the contribution of light-duty vehicles to the underground atmosphere diesel emissions burden, Phase I. Report of Investigation submitted to the Diesel Emissions Evaluation Program (DEEP)., CANMET - Mining and Mineral Sciences Laboratories Report 2000-030(CR). doi:10.1017/CBO9781107415324.004.

Hakkaki-Fard, A., Aidoun, Z., Ouzzane, M., 2015. A computational methodology for ejector design and performance maximisation. Energy Convers. Manag. 105, 1291–1302. doi:10.1016/j.enconman.2015.08.070.

Hart, J.H., 2002. Supersonic Ejector Simulation and Optimisation, Ph.D thesis, University of Sheffield.

He, S., Li, Y., Wang, R.Z., 2009. Progress of mathematical modeling on ejectors. Renew. Sustain. Energy Rev. 13, 1760–1780. doi:10.1016/j.rser.2008.09.032.

Howes, M., Hortin, K., 2005. Surface cooling at Kidd Creek Mine. In: Conference Proceedings of the Eighth International Mine Ventilation Congress.

Huang, B.J., Chang, J.M., Wang, C.P., Petrenko, V.A., 1999. 1-D analysis of ejector performance. Int. J. Refrig. 22, 354–364. doi:10.1016/S0140-7007(99)00004-3.

Johnson, G.K., Steele, W. V., 1981. The standard enthalpy of formation of chalcopyrite (CuFeS2) by fluorine bomb calorimetry. J. Chem. Thermodyn. 13, 991–997. doi:10.1016/0021-9614(81)90076-8.

Keenan, J.H., Neumann, E.P., 1942. A simple air ejector. ASME Journal of Applied Mechanics, 64:75–82.

Keenan, J.H., Neumann, E.P., F., L., 1950. An investigation of ejector design by analysis and experiment. ASME Journal of Applied Mechanics, 72:299–309.

Kohler, J., Richter, C., Tegethoff, W., Tischendorf, C., 2007. Experimental and theoretical study of a CO2 ejector.

Kumar, N.S., Ooi, K.T., 2014. One dimensional model of an ejector with special attention to Fanno flow within the mixing chamber. Appl. Therm. Eng. 65, 226–235. doi:10.1016/j.applthermaleng.2013.12.055.

Langan, B.W., Weng, K., Ward, M.A., 2002. Effect of silica fume and fly ash on heat of hydration of Portland cement. Cem. Concr. Res. 32, 1045–1051. doi:10.1016/S0008-8846(02)00742-1.

Langborne, P.L., 1979. Hydraulic air compression: old invention e new energy source, Chart. Mech. Eng. 26 (10) (1979) 76e81.

Li, C., Li, Y., Wang, L., 2012. Configuration dependence and optimization of the entrainment performance for gas-gas and gas-liquid ejectors. Appl. Therm. Eng. 48, 237–248. doi:10.1016/j.applthermaleng.2011.11.041.

Lin, C., Cai, W., Li, Y., Yan, J., Hu, Y., Giridharan, K., 2013. Numerical investigation of geometry parameters for pressure recovery of an adjustable ejector in multi-evaporator refrigeration system. Appl. Therm. Eng. 61, 649–656. doi:10.1016/j.applthermaleng.2013.08.033.

Liu, F., Groll, E.A., 2013. Study of ejector efficiencies in refrigeration cycles. Appl. Therm. Eng. 52, 360–370. doi:10.1016/j.applthermaleng.2012.12.001.

Maqsood, A., 2008. Ejectors, Subsonic Air-air Bent, Short Tubes, Mixing.

McGovern, R.K., Prakash Narayan, G., Lienhard, J.H., 2012. Analysis of reversible ejectors and definition of an ejector efficiency. Int. J. Therm. Sci. 54, 153–166. doi:10.1016/j.ijthermalsci.2011.11.003.

McPherson, M., 1993. Subsurface Ventilation Engineering (Online Edition). Mine Ventilation Services.

Millar, D., Hutchison, A., Noula, C., Pavese, V., Rico, J., Young, S., 2016. The role of water solubility in applications of hydraulic air compressors in mining, in: Proceedings of 2016 Energy & Water Symposium.

Millar, D., Trapani, K., Romero, A., Ahmed, N., 2014. COOLING OPTIONS FOR ULTRA DEEP MINES IN NORTHERN ONTARIO.

Millar, D.L., 2014. A review of the case for modern-day adoption of hydraulic air compressors. Appl. Therm. Eng. 69, 55–77. doi:10.1016/j.applthermaleng.2014.04.008.

Munday, J., Bagster, D., 1977. A new ejector theory applied to steam jet refrigeration. Ind. Eng. Chem. Process Des. Dev. 16, 442–449. doi:10.1021/i260064a003.

Newman, L., Herbert, Y., 2009. "The use of deep water cooling systems: Two Canadian examples." Renewable Energy 34(3): 727-730.

NIST, 2005. NIST chemistry webbook: NIST Standard Reference Database Number 69.

O'Connor, D., 2008. Ventilation on demand (VOD) auxiliary fan project–Vale Inco Limited, Creighton Mine. Proc. 12th US Mine Vent. Symp. 41–44.

Obert, E.F., 1960. Concepts of Thermodynamics. McGraw-Hill, New York.

Oosthuizen, N.L., 2012. Optimum water distribution between pumping stations of multiple mine shafts 3–5.

Ouzzane, M., Aidoun, Z., 2003. Model development and numerical procedure for detailed ejector analysis and design. Appl. Therm. Eng. 23, 2337–2351.

Özdeniz, A.H., Kelebek, S., 2013. A study of self-heating characteristics of a pyrrhotite-rich sulphide ore stockpile. International Journal of Mining Science and Technology, 23, 381- 386.

Pavese, V., Millar, D., Verda, V., 2016. Mechanical Efficiency of Hydraulic Air Compressors. J. Energy Resour. Technol. 138, 62005. doi:10.1115/1.4033623.

Pianthong, K., Seehanam, W., Behnia, M., Sriveerakul, T., Aphornratana, S., 2007. Investigation and improvement of ejector refrigeration system using computational fluid dynamics technique. Energy Convers. Manag. 48, 2556–2564. doi:10.1016/j.enconman.2007.03.021.

Riffat, S.B., Gan, G., Smith, S., 1996. Computational fluid dynamics applied to ejector heat pumps. Appl. Therm. Eng. 16, 291–297. doi:10.1016/1359-4311(95)00033-X.

Rusly, E., Aye, L., Charters, W.W.S., Ooi, A., 2005. CFD analysis of ejector in a combined ejector cooling system. Int. J. Refrig. 28, 1092–1101. doi:10.1016/j.ijrefrig.2005.02.005.

Rutherford, J., 1958. "Ventilation Heat Exchanger at Inco's Creighton Mine." Canadian Mining Journal: 97-100.

Schafrick, S., 2014. The geometry of heat exchange in fractured, broken rock. PhD Thesis. Laurentian University.

Schulze, L.E., 1954. Hydraulic Air Compressors. United States Department of Interior Information Circular 7683.

Sheer, J., del Castillo, D., Csatary, C., 1986. Unconventional systems cooling mines.

Smith, S.J., Dphil, S.B.R., Ceng, M., Mashrae, M., Wu, S., Eames, I., 1997. Low-pressure ejectors : Prediction of performance by computational fluid dynamics 179–182.

Sriveerakul, T., Aphornratana, S., Chunnanond, K., 2007. Performance prediction of steam ejector using computational fluid dynamics: Part 1. Validation of the CFD results. Int. J. Therm. Sci. 46, 812–822. doi:10.1016/j.ijthermalsci.2006.10.014

Sun, 1996. Geometry ejectors and their applications in ejector refrigeration systems. Energy 21, 919–929. doi:10.1016/0360-5442(96)00038-2.

Sun, D., Eames, I., 1996. Performance characteristics of HCFC-123 ejector refrigeration cycles. Int. J. Energy Res. 20, 871–885. doi:10.1002/(SICI)1099-114X(199610)20:10<871::AID-ER201>3.0.CO;2-4.

Taylor, C.H., 1913. The measurement of compressed air delivered by the hydraulic compressor, Cobalt, Can. Min. Metall. Trans. 16, 210e215.

Van der Waals, J.D., 1873. Over de Continuiteit van den Gas- en Vloeistoftoestand (on the continuity of the gas and liquid state) Ph.D. thesis, Universiteit Leiden.

Varga, S., Oliveira, A.C., Diaconu, B., 2009. Numerical assessment of steam ejector efficiencies using CFD. Int. J. Refrig. 32, 1203–1211. doi:10.1016/j.ijrefrig.2009.01.007.

Varga, S., Oliveira, A.C., Diaconu, B., 2009. Influence of geometrical factors on steam ejector performance – A numerical assessment, International Journal of Refrigeration, Volume 32, Issue 7, Pages 1694-1701.

Wassgren, C., 2010. Notes on Fluid Mechanics and Gas Dynamics.

Wu, H., Liu, Z., Han, B., Li, Y., 2014. Numerical investigation of the influences of mixing chamber geometries on steam ejector performance. Desalination 353, 15–20. doi:10.1016/j.desal.2014.09.002.

Yadav, R.L., Patwardhan, A.W., 2008. Design aspects of ejectors: Effects of suction chamber geometry. Chem. Eng. Sci. 63, 3886–3897. doi:10.1016/j.ces.2008.04.012.

Yang, X., Long, X., Yao, X., 2012. Numerical investigation on the mixing process in

a steam ejector with different nozzle structures. Int. J. Therm. Sci. 56, 95–106. doi:10.1016/j.ijthermalsci.2012.01.021.

Young, S., Hutchison, a, Sengupta, S., Clifford, T., Pavese, V., Noula, C., Myre, M., 2015. Conceptual design of a modern-day hydraulic air compressor.

Zhu, Y., Cai, W., Wen, C., Li, Y., 2009. Numerical investigation of geometry parameters for design of high performance ejectors. Appl. Therm. Eng. 29, 898–905. doi:10.1016/j.applthermaleng.2008.04.025.

Zhu, Y., Cai, W., Wen, C., Li, Y., 2007. Shock circle model for ejector performance evaluation. Energy Convers. Manag. 48, 2533–2541. doi:10.1016/j.enconman.2007.03.024.

Zhu, Y., Jiang, P., 2014. Experimental and analytical studies on the shock wave length in convergent and convergent-divergent nozzle ejectors. Energy Convers. Manag. 88, 907–914. doi:10.1016/j.enconman.2014.09.023.

APPENDICES

Appendix A- Nozzle –Mixing diameter simulations graphic contours

- Nozzle diameter 101.6 mm, 0.75 m Mixing chamber

Contours of Static Pressure (pascal)

Sep 23, 2016
ANSYS Fluent Release 16.0 (3d, dp, pbns, rke)

Contours of Velocity Magnitude (m/s)

Contours of Static Temperature (k)

- Nozzle diameter 101.6 mm, 1 m Mixing chamber

Contours of Static Pressure (pascal)

Sep 23, 2016
ANSYS Fluent Release 16.0 (3d, dp, pbns, rke)

Contours of Velocity Magnitude (m/s)

Sep 23, 2016
ANSYS Fluent Release 16.0 (3d, dp, pbns, rke)

Contours of Static Temperature (k)

Sep 23, 2016
ANSYS Fluent Release 16.0 (3d, dp, pbns, rke)
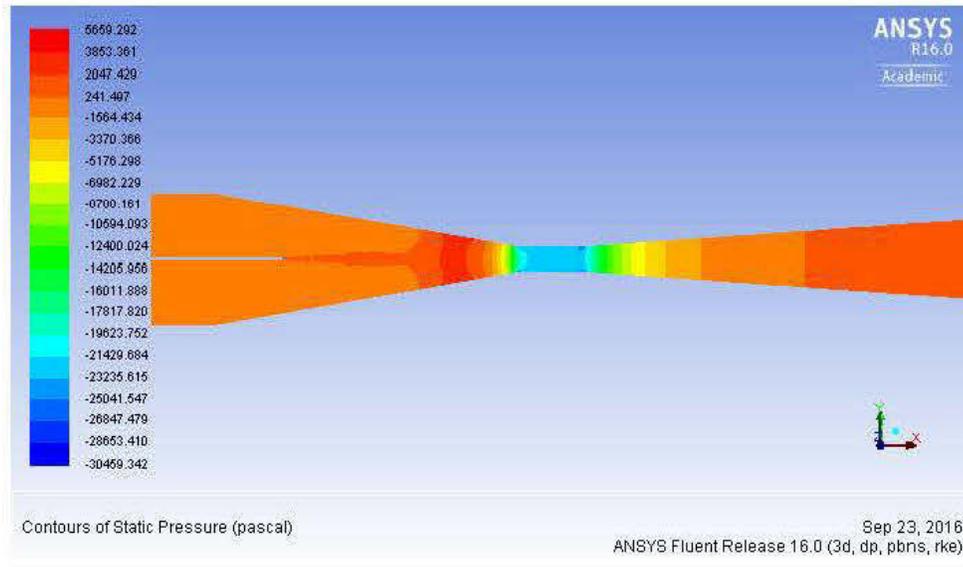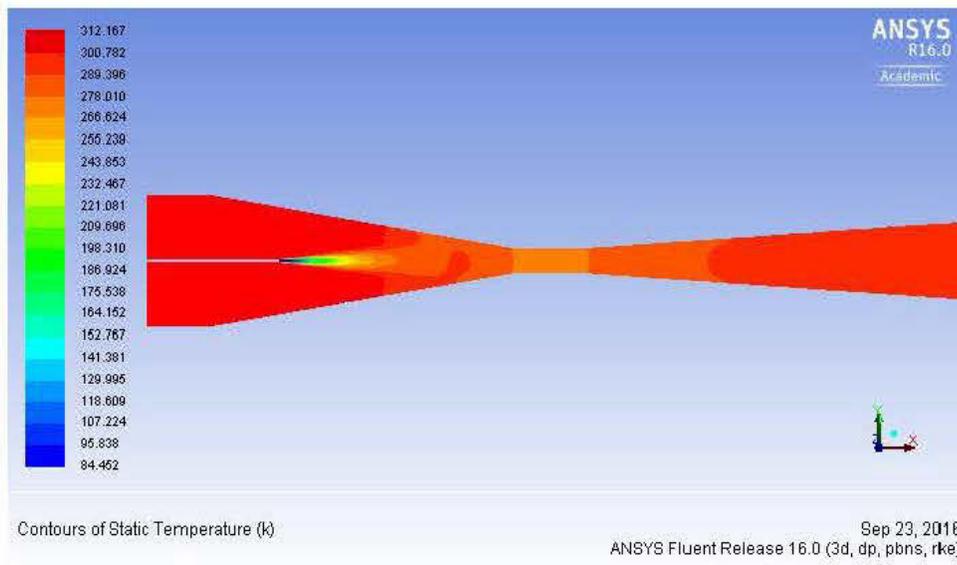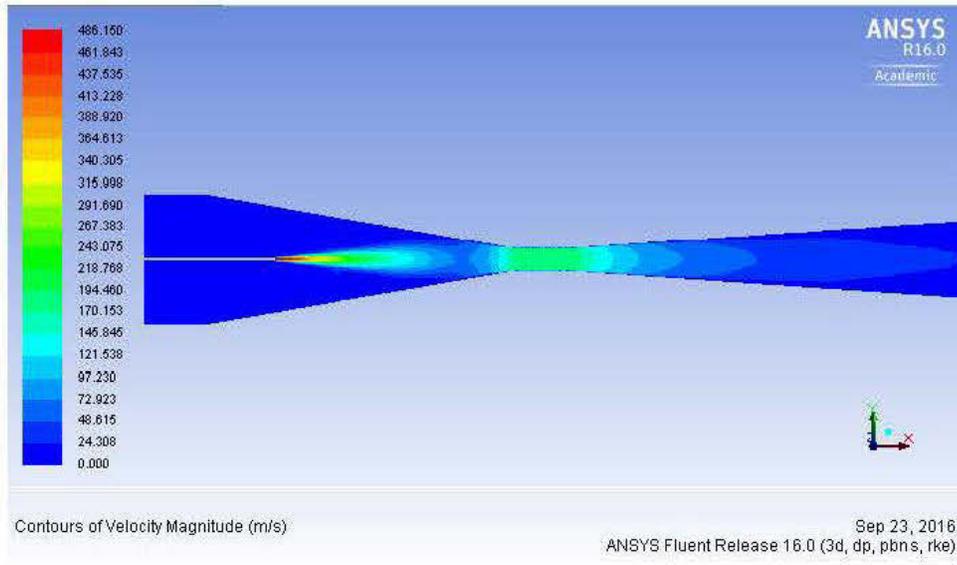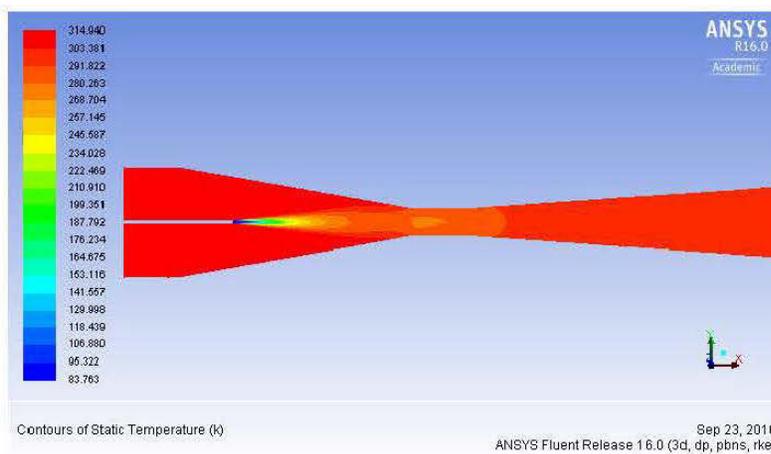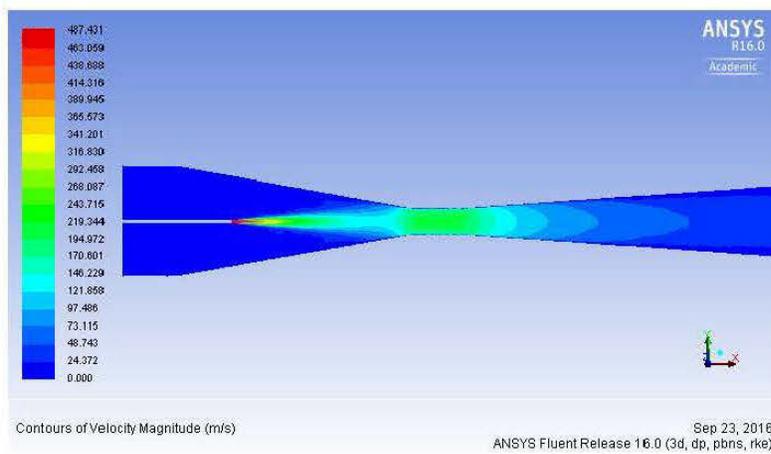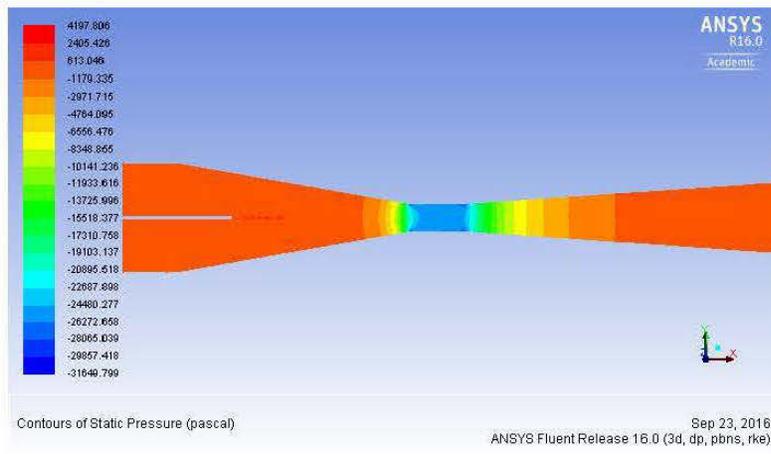
- Nozzle diameter 101.6 mm, 1.25 m Mixing chamber

Contours of Static Pressure (pascal)

Contours of Velocity Magnitude (m/s)

Contours of Static Temperature (k)
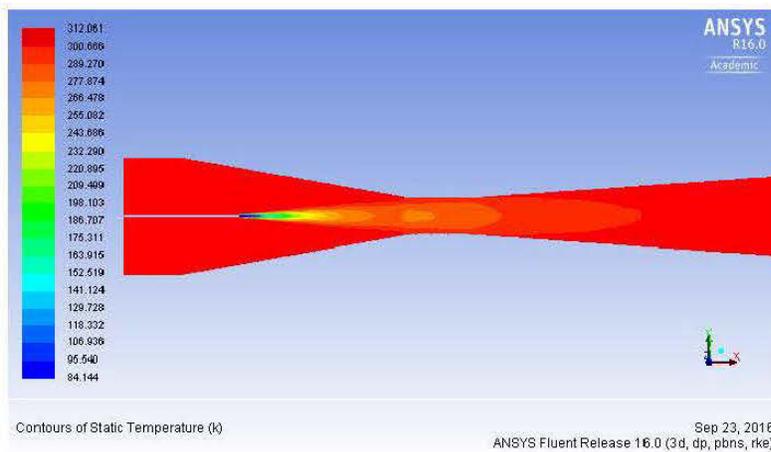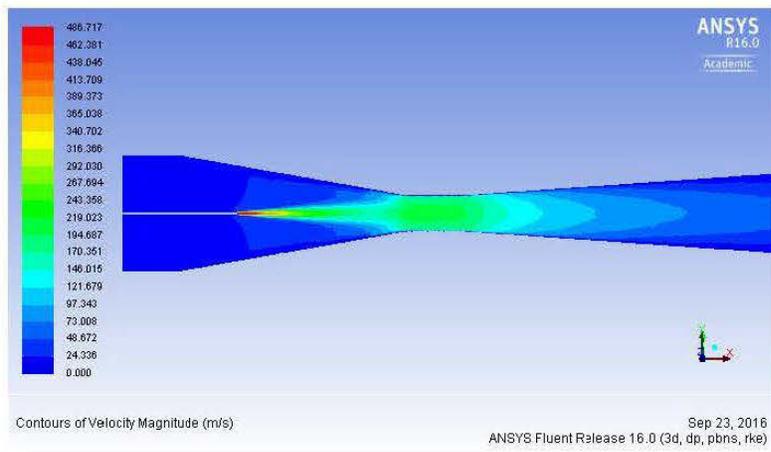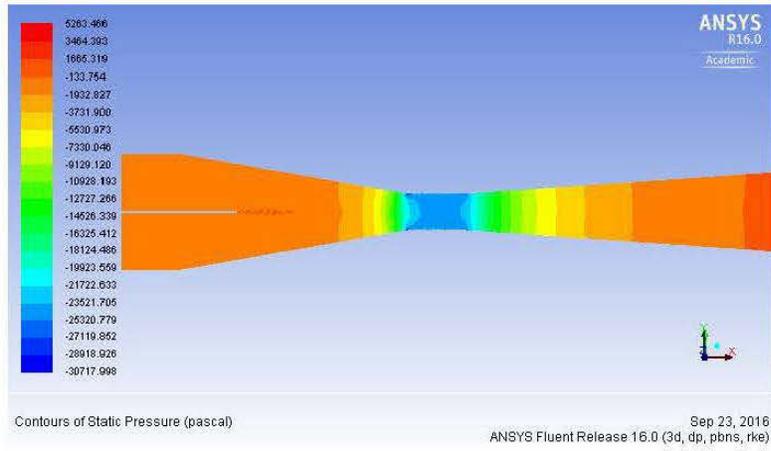
- Nozzle diameter 152.4 mm, 0.75 m Mixing chamber

Contours of Static Pressure (pascal)

Sep 23, 2016
ANSYS Fluent Release 16.0 (3d, dp, pbns, rke)

Contours of Velocity Magnitude (m/s)

Sep 23, 2016
ANSYS Fluent Release 16.0 (3d, dp, pbns, rke)

Contours of Static Temperature (k)

Sep 23, 2016
ANSYS Fluent Release 16.0 (3d, dp, pbns, rke)
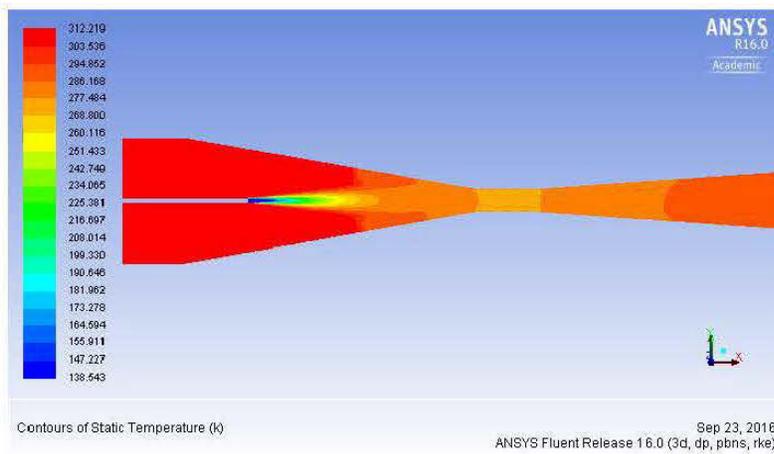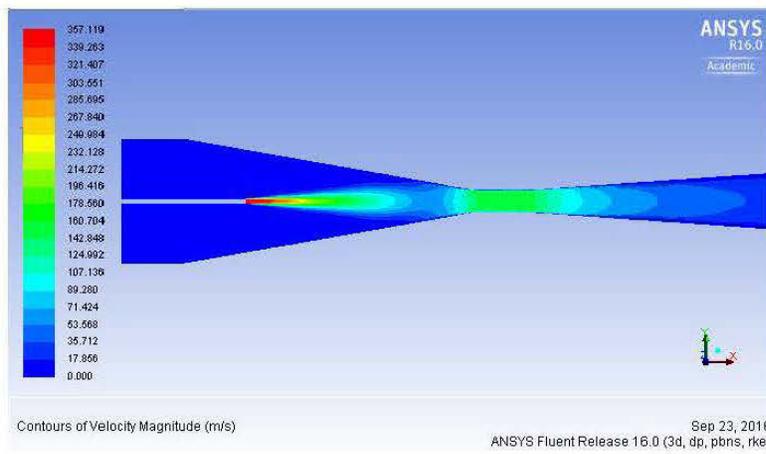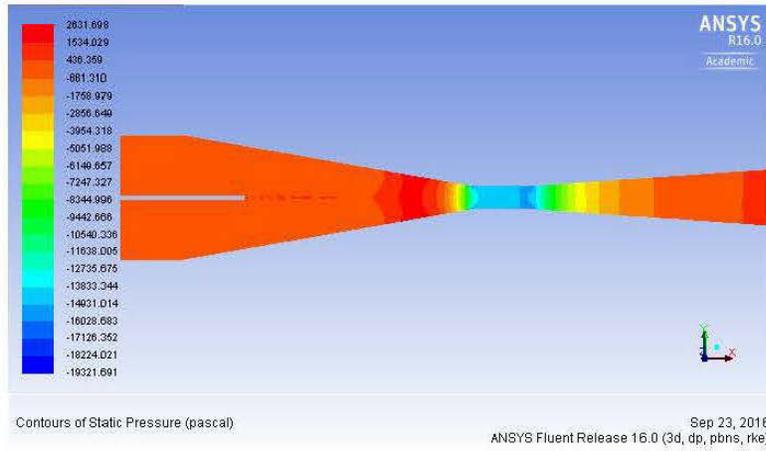
- Nozzle diameter 152.4 mm, 1 m Mixing chamber

Contours of Static Pressure (pascal)

Sep 23, 2016
ANSYS Fluent Release 16.0 (3d, dp, pbns, rke)

Contours of Velocity Magnitude (m/s)

Sep 23, 2016
ANSYS Fluent Release 16.0 (3d, dp, pbns, rke)

Contours of Static Temperature (k)

Sep 23, 2016
ANSYS Fluent Release 16.0 (3d, dp, pbns, rke)

- Nozzle diameter 152.4 mm, 1.25 m Mixing chamber

Contours of Static Pressure (pascal)

Sep 23, 2016
ANSYS Fluent Release 16.0 (3d, dp, pbns, rke)

Contours of Velocity Magnitude (m/s)

Sep 23, 2016
ANSYS Fluent Release 16.0 (3d, dp, pbns, rke)

Contours of Static Temperature (k)

Sep 23, 2016
ANSYS Fluent Release 16.0 (3d, dp, pbns, rke)

- Nozzle diameter 304.8 mm, 0.75 m Mixing chamber

Contours of Static Pressure (pascal)

Contours of Velocity Magnitude (m/s)

Contours of Static Temperature (k)
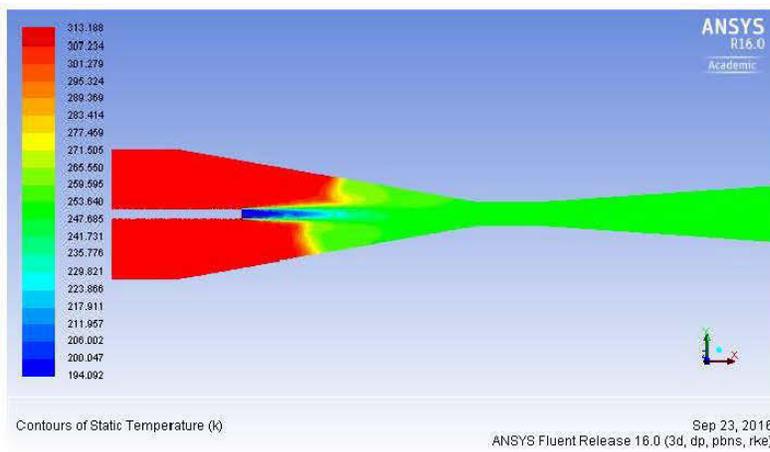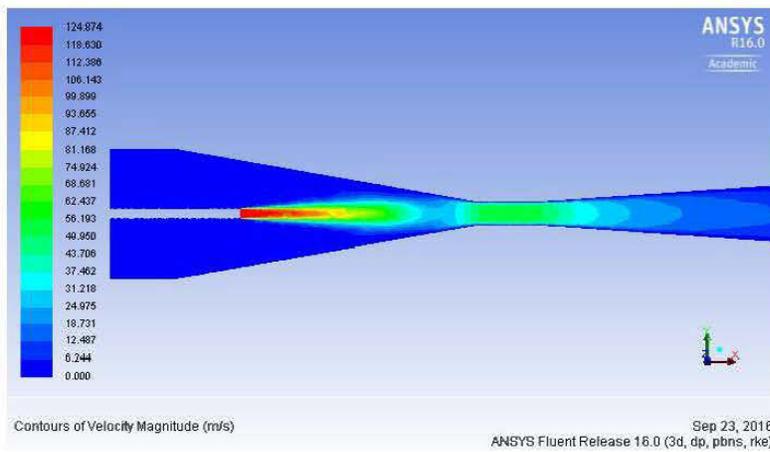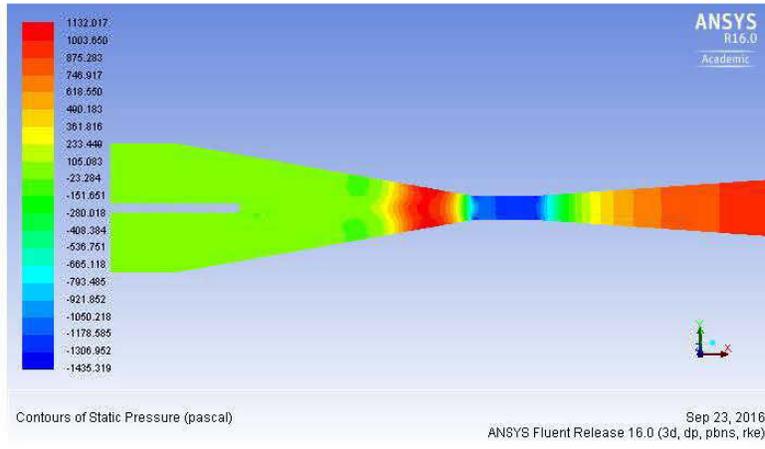
- Nozzle diameter 304.8 mm, 1 m Mixing chamber

Contours of Static Pressure (pascal)

Sep 23, 2016
ANSYS Fluent Release 16.0 (3d, dp, pbns, rke)

Contours of Velocity Magnitude (m/s)

Sep 23, 2016
ANSYS Fluent Release 16.0 (3d, dp, pbns, rke)

Contours of Static Temperature (k)

Sep 23, 2016
ANSYS Fluent Release 16.0 (3d, dp, pbns, rke)
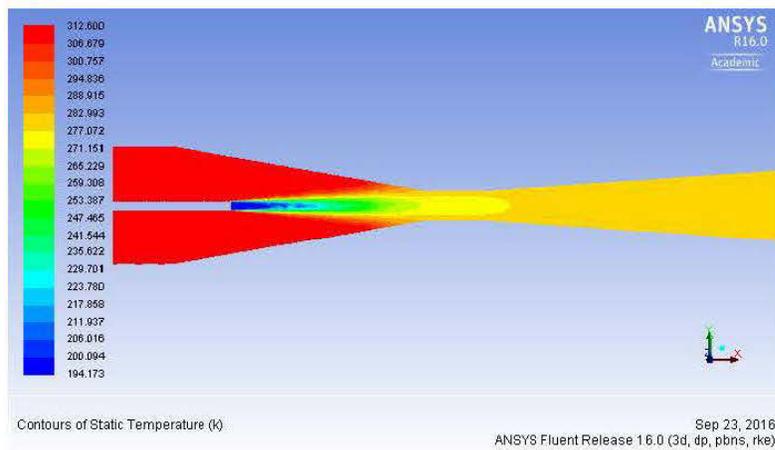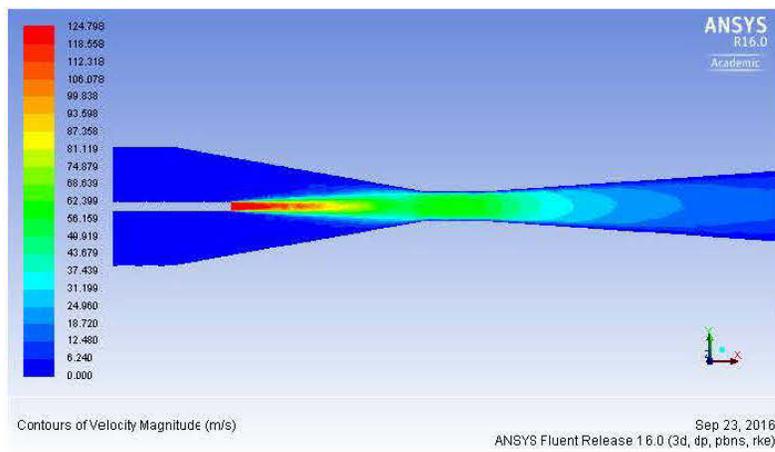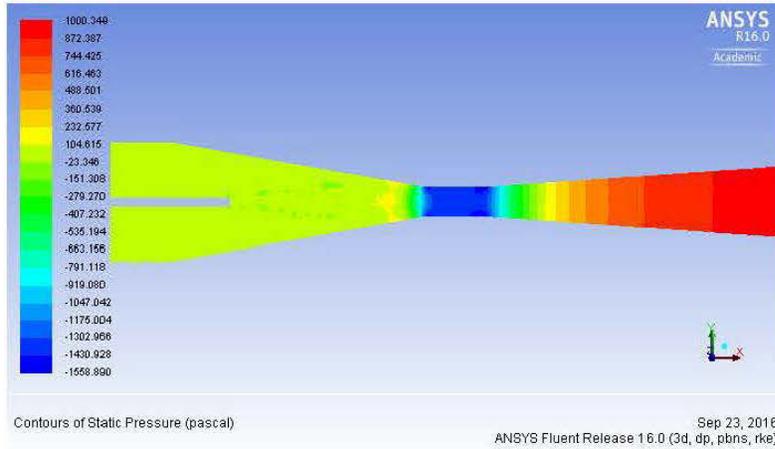
- Nozzle diameter 304.8 mm, 1.25 m Mixing chamber

Contours of Static Pressure (pascal)

Sep 23, 2016
ANSYS Fluent Release 16.0 (3d, dp, pbns, rke)

Contours of Velocity Magnitude (m/s)

Sep 23, 2016
ANSYS Fluent Release 16.0 (3c, dp, pbns, rke)

Contours of Static Temperature (k)

Sep 23, 2016
ANSYS Fluent Release 16.0 (3d, dp, pbns, rke)
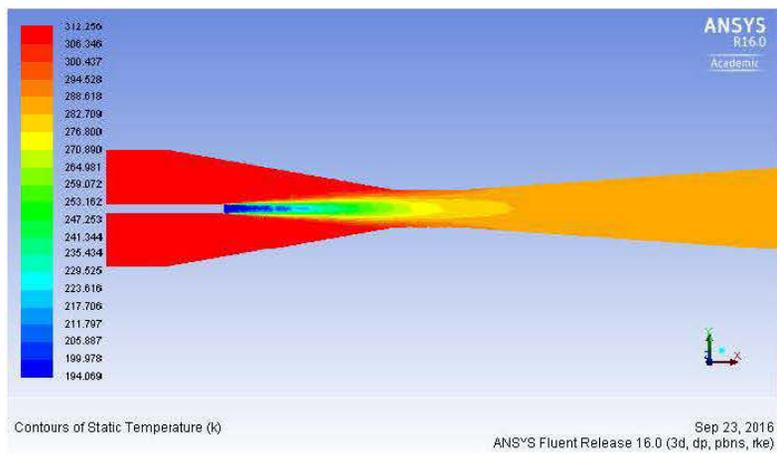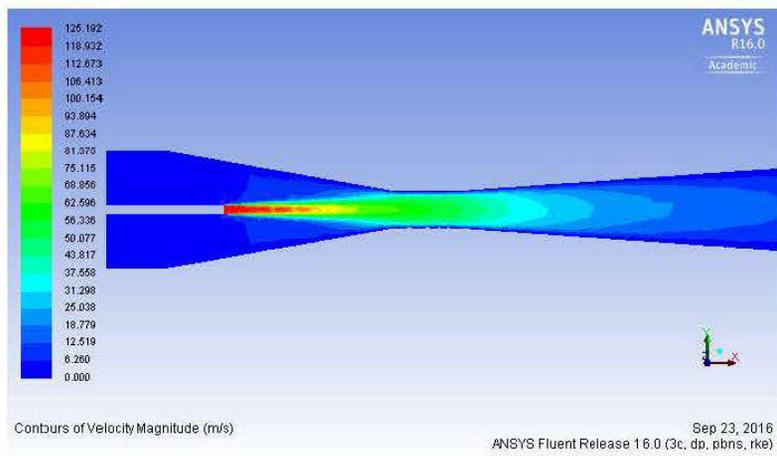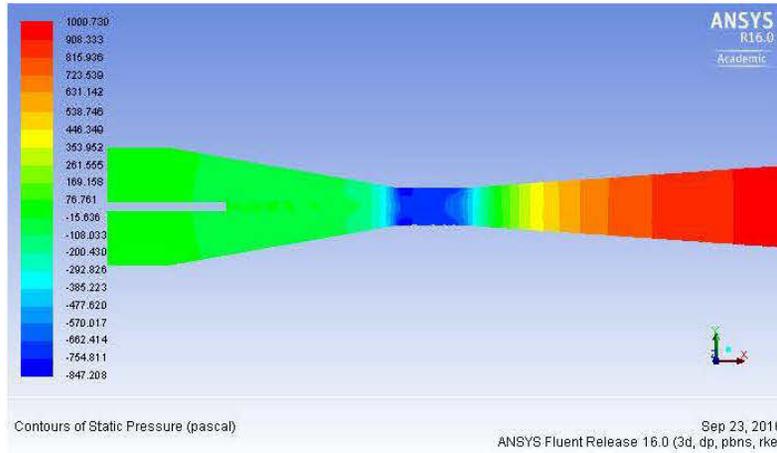
Appendix B – Fan curves, Mine scale model

- Mass flow 15.36 kg/s, 500 Pa (Pressure, velocity, temperature)

Contours of Static Pressure (pascal)

Sep 23, 2016
ANSYS Fluent Release 16.0 (3d, dp, pbns, rke)
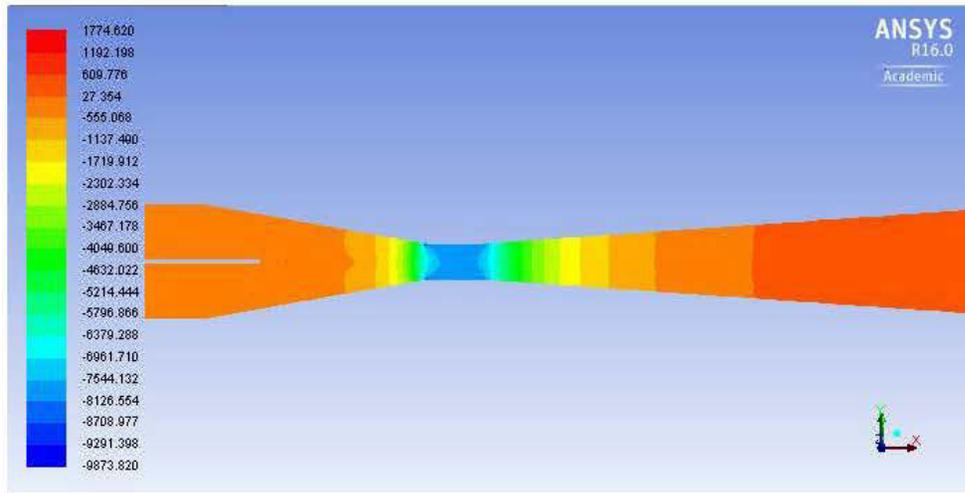
Contours of Velocity Magnitude (m/s)

Sep 23, 2016
ANSYS Fluent Release 16.0 (3d, dp, pbns, rke)
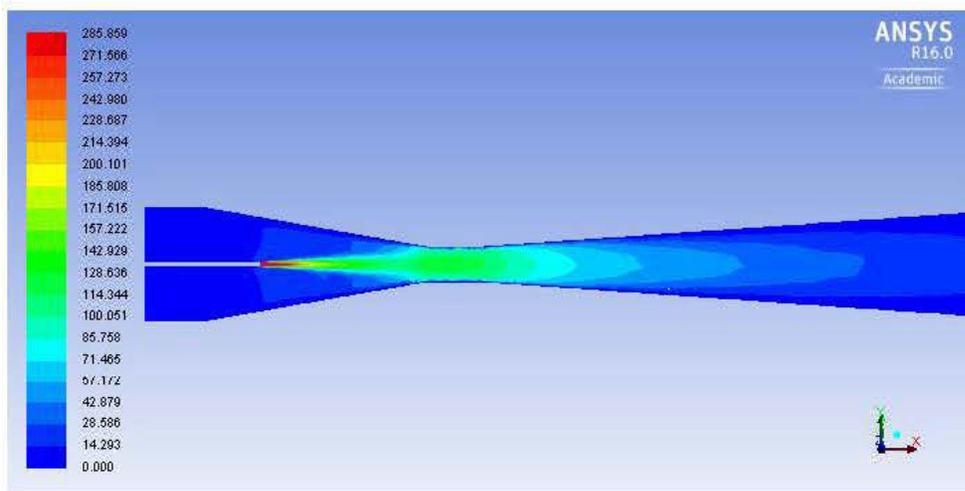
Contours of Static Temperature (k)

Sep 23, 2016
ANSYS Fluent Release 16.0 (3d, dp, pbns, rke)
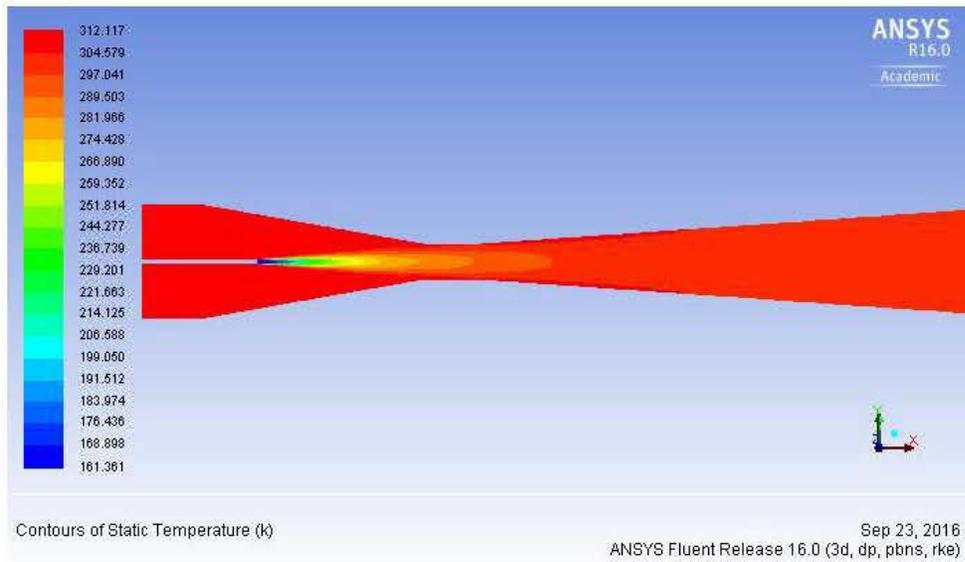
- Mass flow 15.36 kg/s, 1000 Pa (Pressure, velocity, temperature)

Contours of Static Pressure (pascal)

Sep 23, 2016
ANSYS Fluent Release 16.0 (3d, dp, pbns, rke)

Contours of Velocity Magnitude (m/s)

Sep 23, 2016
ANSYS Fluent Release 16.0 (3d, dp, pbns, rke)

Contours of Static Temperature (k)

Sep 23, 2016
ANSYS Fluent Release 16.0 (3d, dp, pbns, rke)
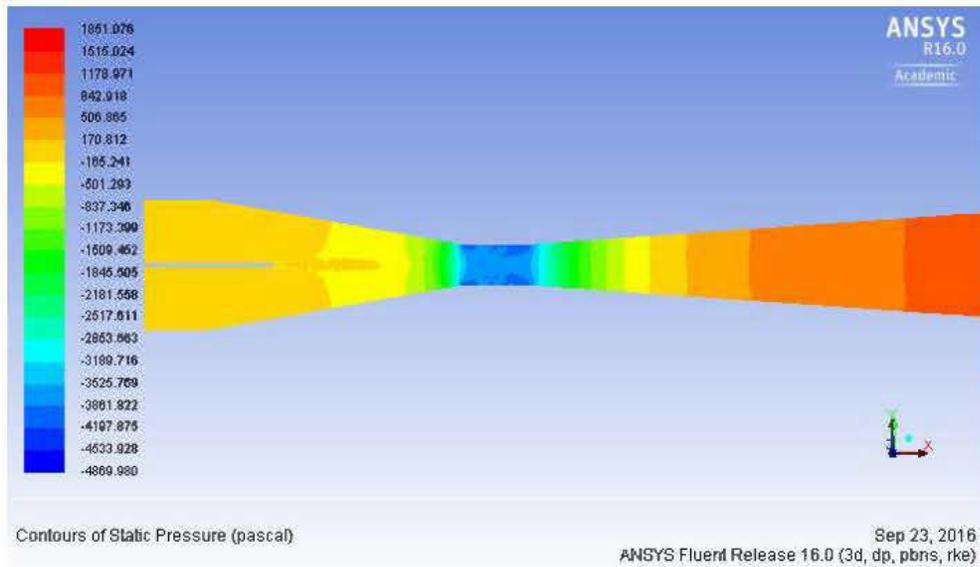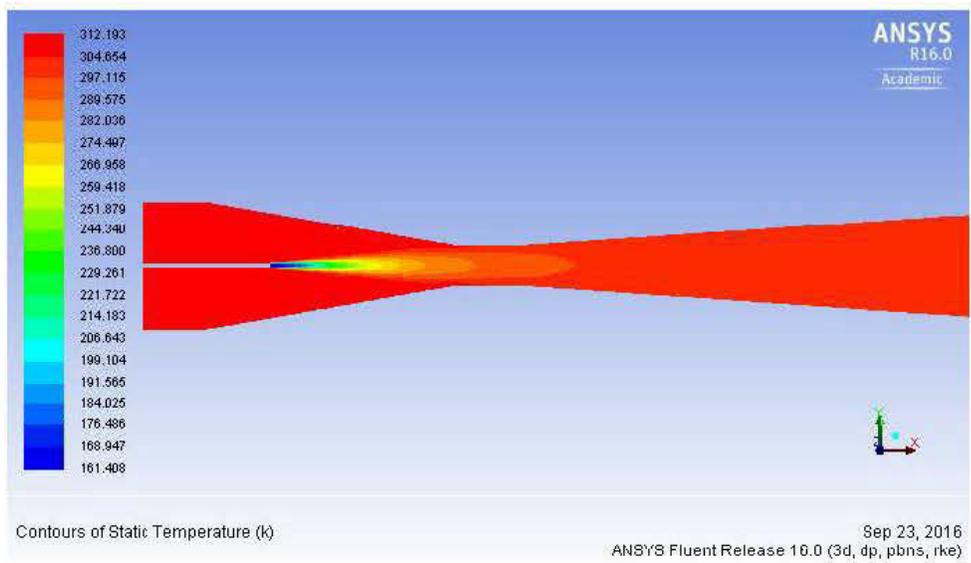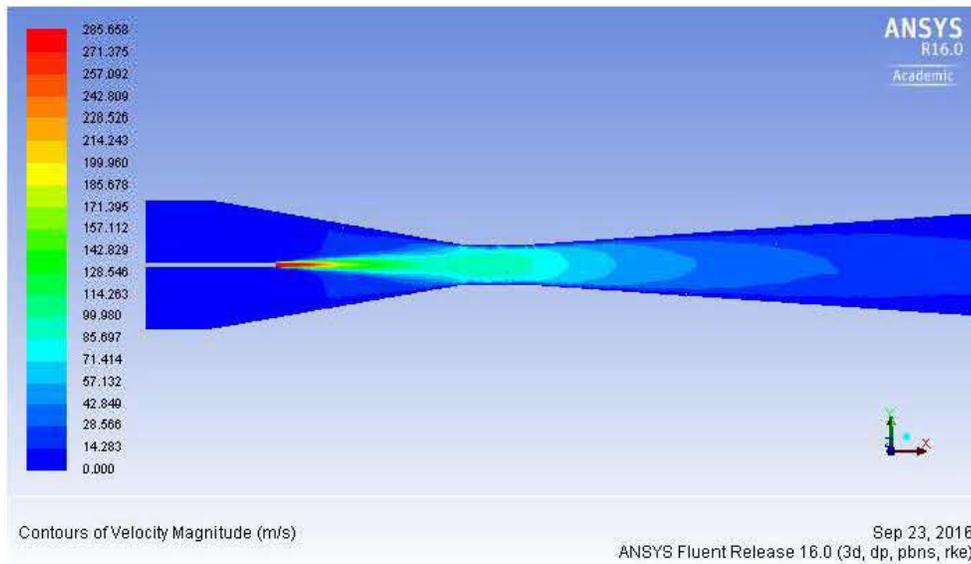
- Mass flow 15.36 kg/s, 1500 Pa (Pressure, velocity, temperature)
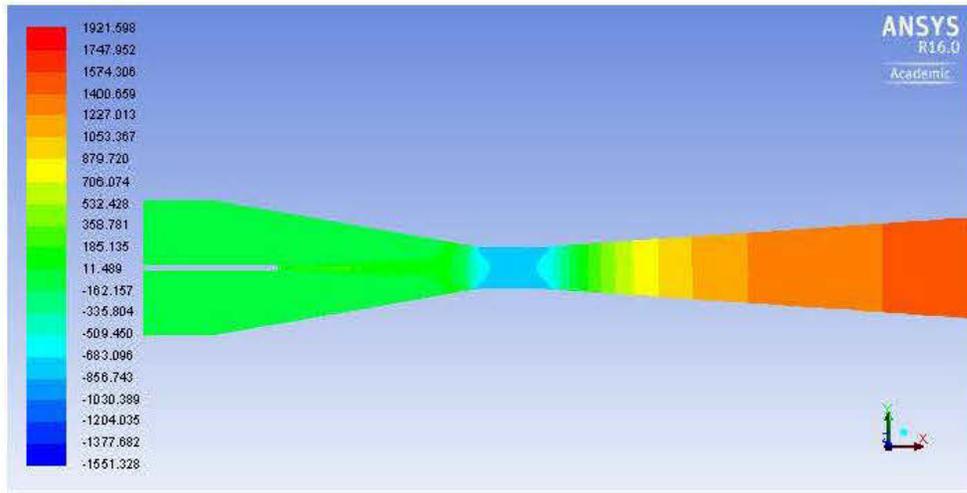
Contours of Static Pressure (pascal)

Sep 23, 2016
ANSYS Fluent Release 16.0 (3d, dp, pbns, rke)

Contours of Velocity Magnitude (m/s)

Sep 23, 2016
ANSYS Fluent Release 16.0 (3d, dp, pbns, rke)
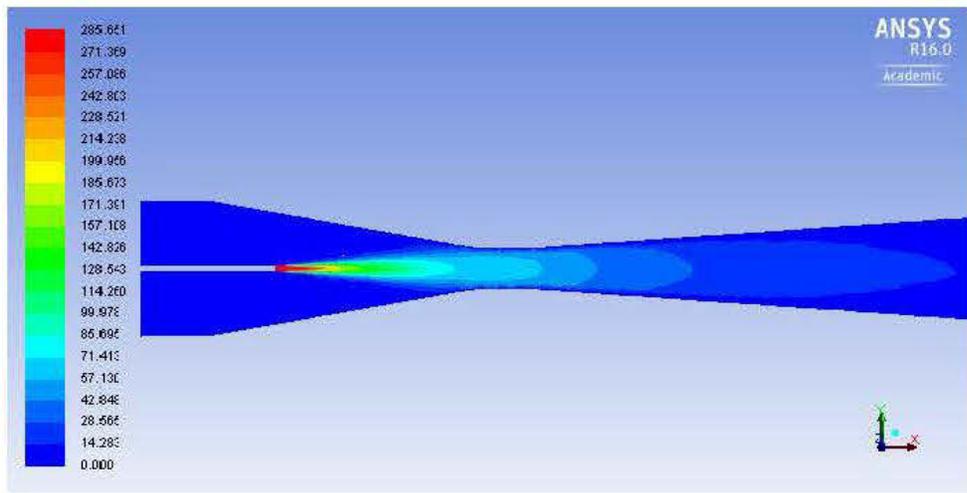
Contours of Static Temperature (k)

Sep 23, 2016
ANSYS Fluent Release 16.0 (3d, dp, pbns, rke)
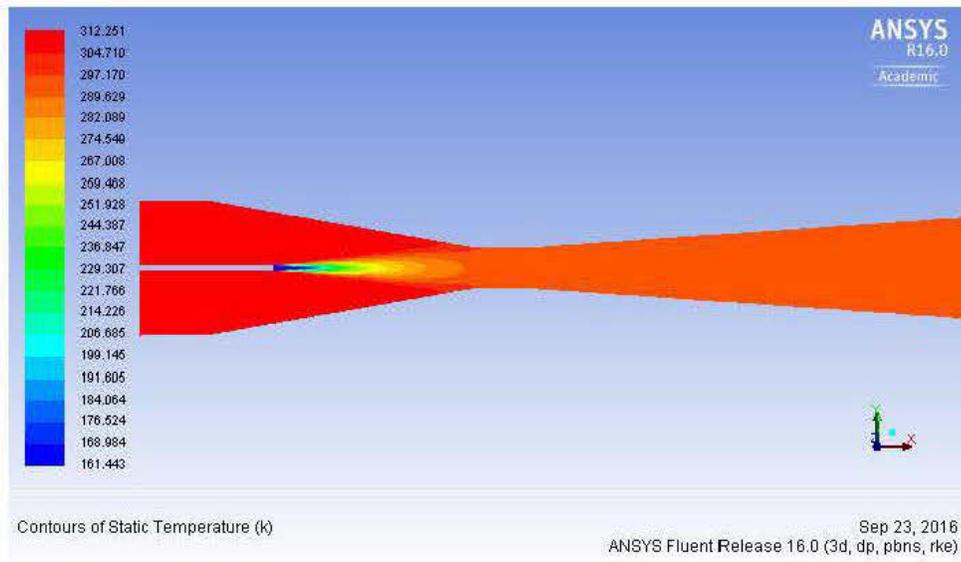
- Mass flow 15.36 kg/s, 2000 Pa (Pressure, velocity, temperature)

Contours of Static Pressure (pascal)

Sep 23, 2016
ANSYS Fluent Release 16.0 (3d, dp, pbns, rke)

Contours of Velocity Magnitude (m/s)   Sep 23, 2016
                                          ANSYS Fluent Release 16.0 (3d, dp, pbns, rke)

Contours of Static Temperature (k)   Sep 23, 2016
                                          ANSYS Fluent Release 16.0 (3d, dp, pbns, rke)
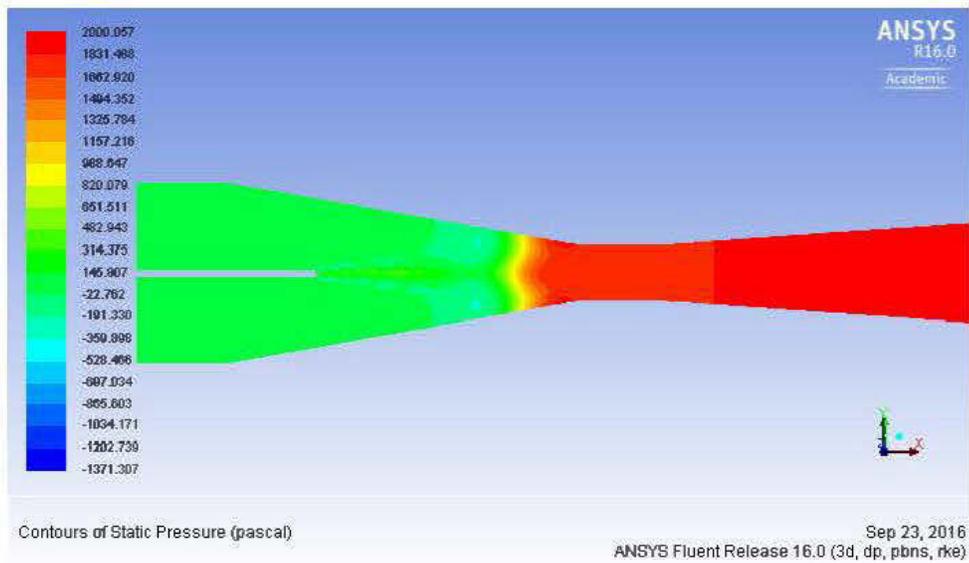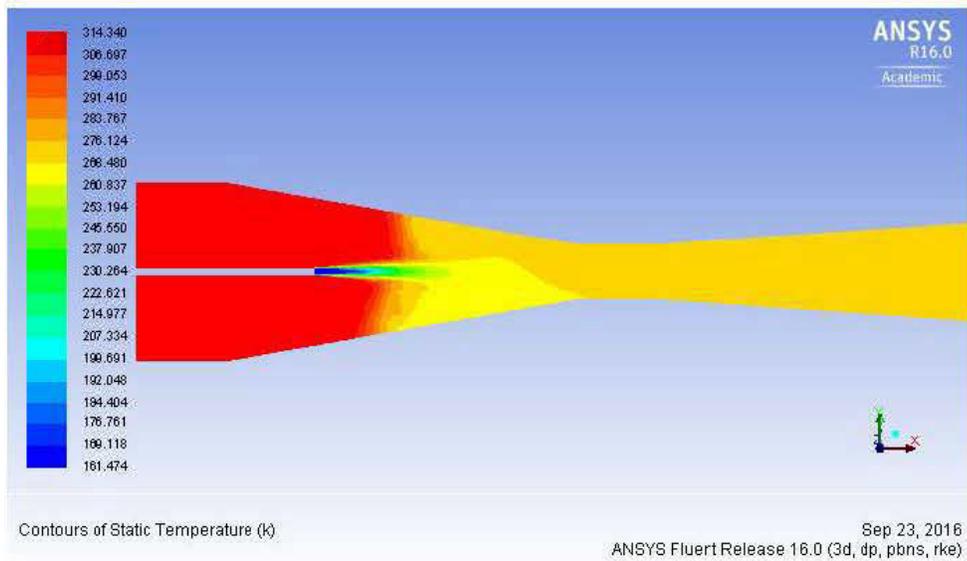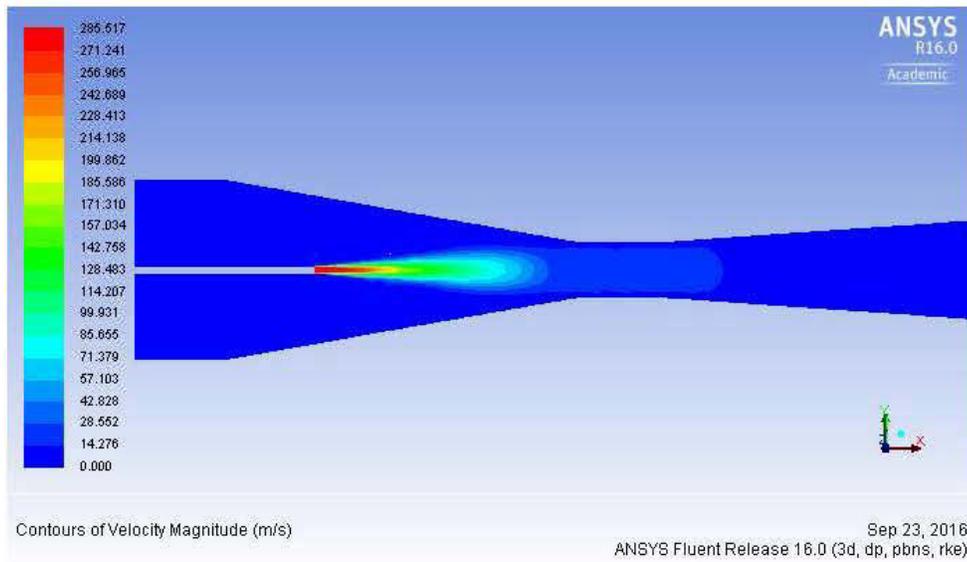
- Mass flow 22.36 kg/s, 500 Pa (Pressure, velocity, temperature)

Contours of Static Pressure (pascal)

ANSYS Fluent Release 16.0 (3d, dp, pbns, rke)

Sep 23, 2016

Contours of Velocity Magnitude (m/s)

ANSYS Fluent Release 16.0 (3d, dp, pbns, rke)

Sep 23, 2016

Contours of Static Temperature (k)

Sep 23, 2016
ANSYS Fluent Release 16.0 (3d, dp, pbns, rke)

- Mass flow 22.36 kg/s, 1000 Pa (Pressure, velocity, temperature)

Contours of Static Pressure (pascal)

Sep 23, 2016
ANSYS Fluent Release 16.0 (3d, dp, pons, rke)

Contours of Velocity Magnitude (m/s)

Contours of Static Temperature (k)
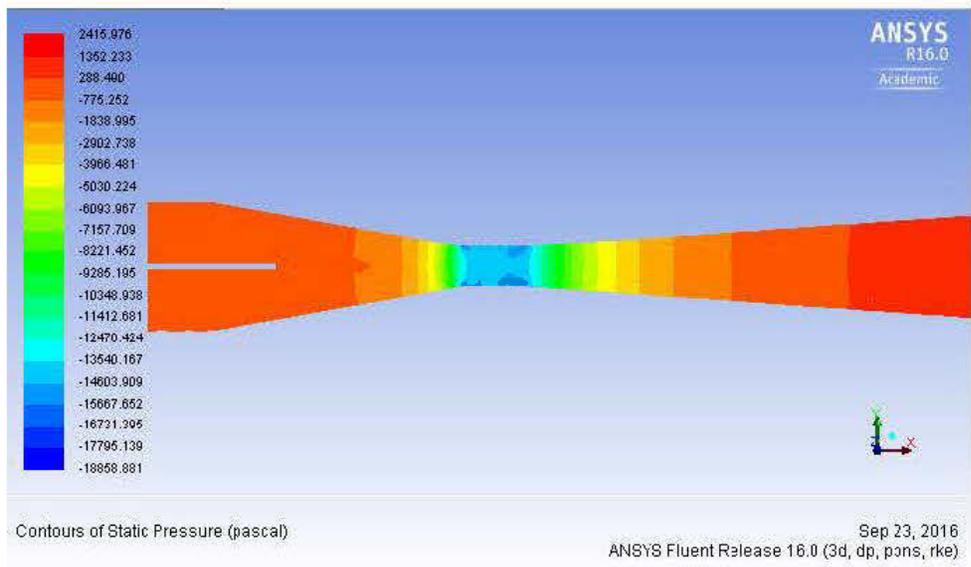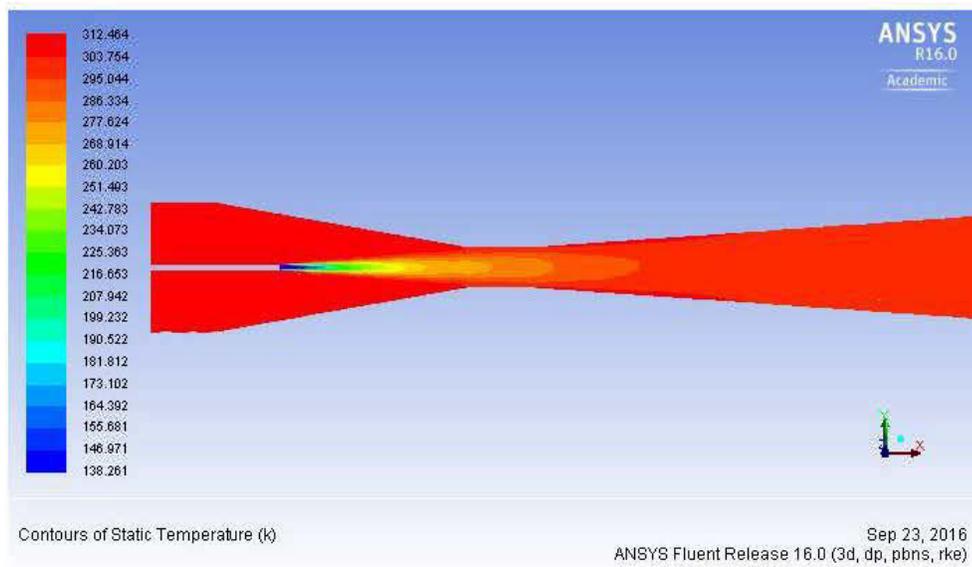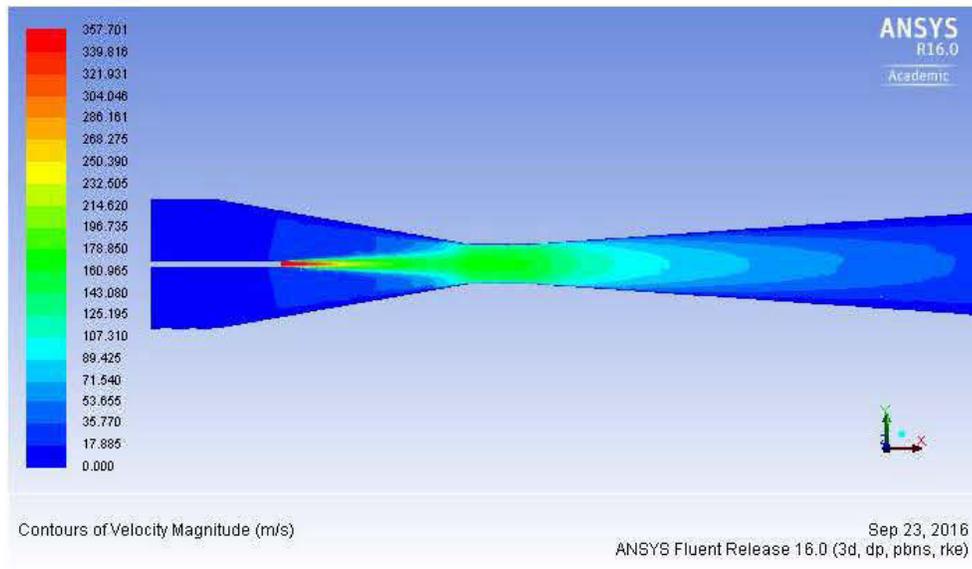
- Mass flow 22.36 kg/s, 1500 Pa (Pressure, velocity, temperature)
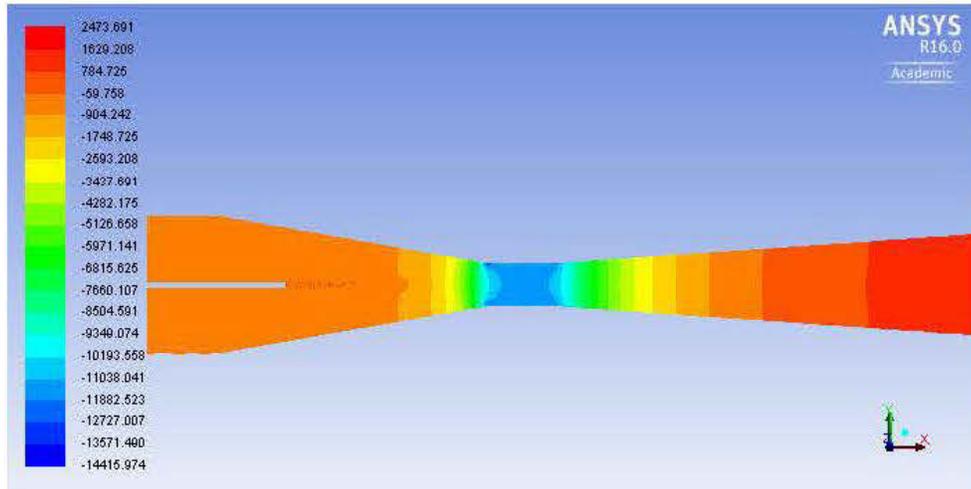
Contours of Static Pressure (pascal)

Sep 23, 2016
ANSYS Fluent Release 16.0 (3d, dp, pbns, rke)

Contours of Velocity Magnitude (m/s)

Sep 23, 2016
ANSYS Fluent Release 16.0 (3d, dp, pbns, rke)
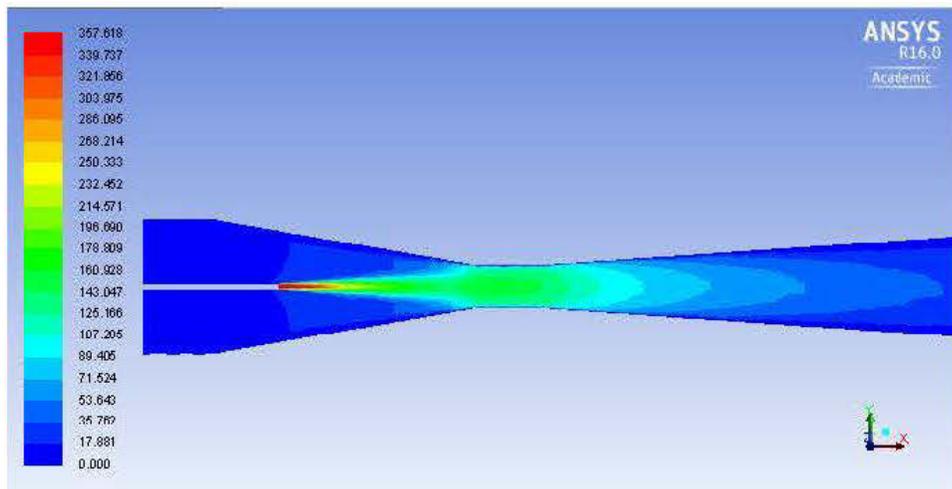
Contours of Static Temperature (k)

Sep 23, 2016
ANSYS Fluent Release 16.0 (3d, dp, pbns, rke)
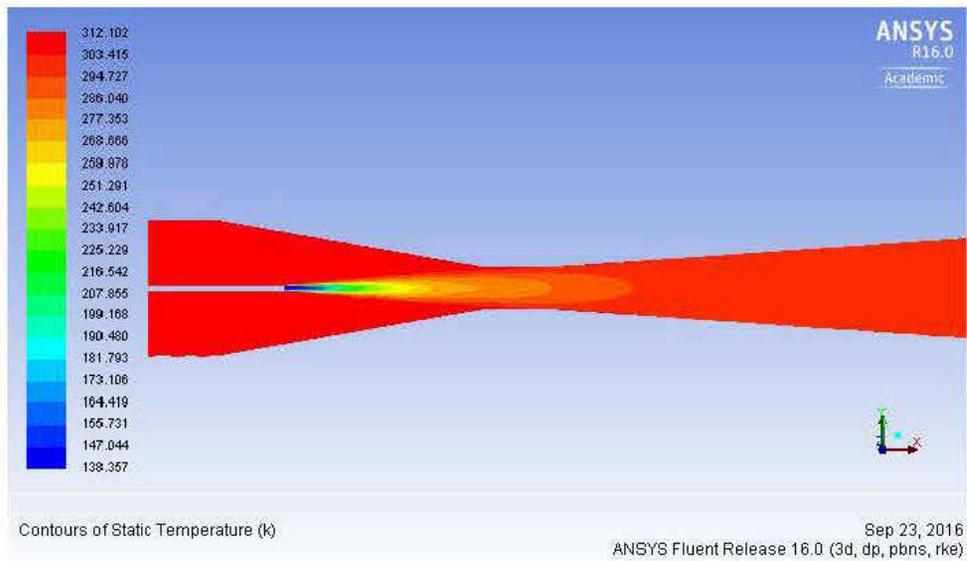
- Mass flow 22.36 kg/s, 2000 Pa (Pressure, velocity, temperature)

Contours of Static Pressure (pascal)

Sep 23, 2016
ANSYS Fluent Release 16.0 (3d, dp, pbns, rke)

Contours of Velocity Magnitude (m/s)

Contours of Static Temperature (k)
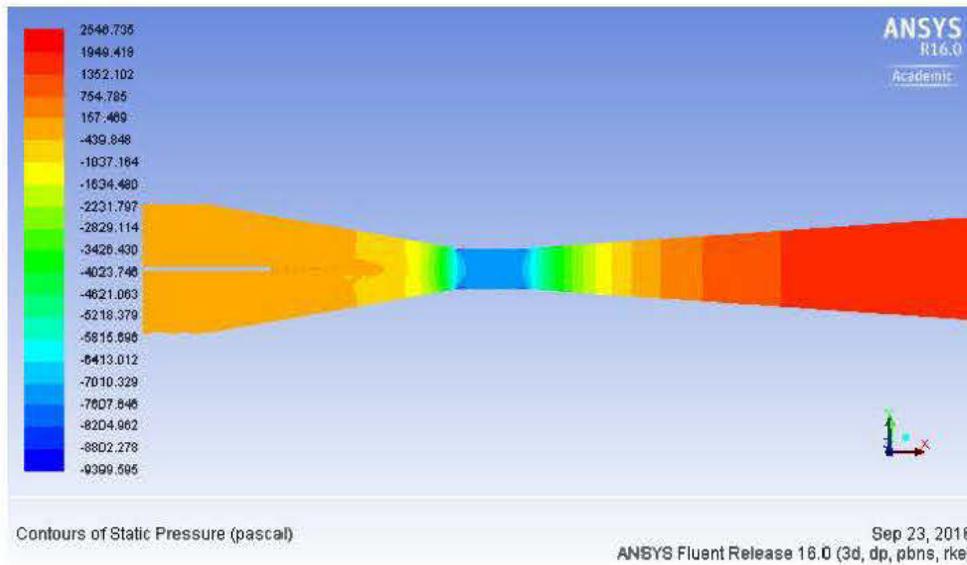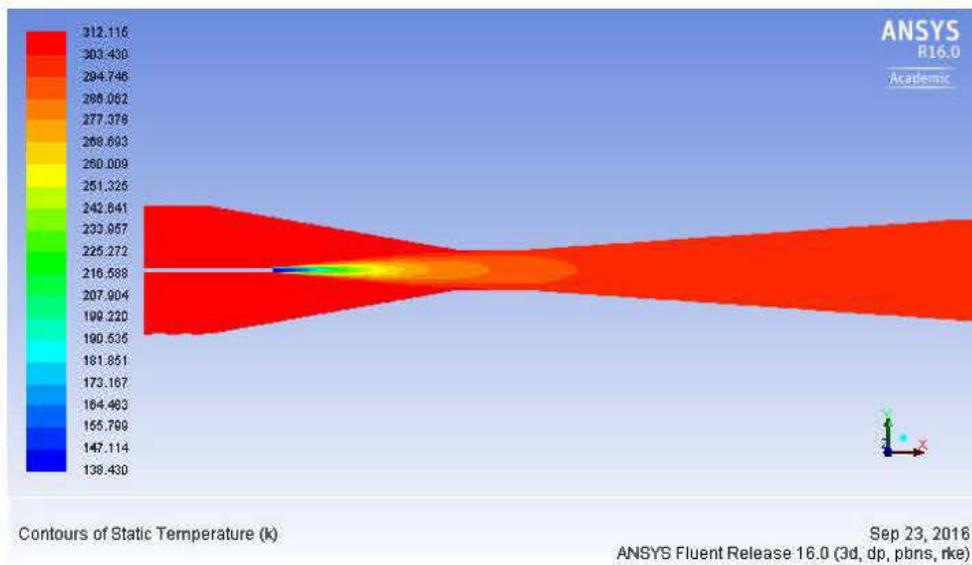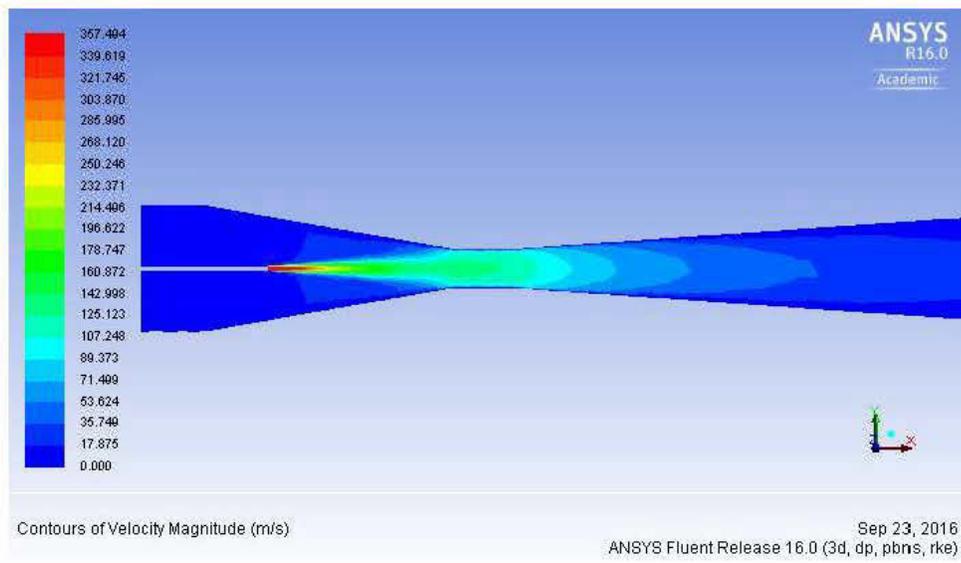
- Mass flow 29.36 kg/s, 500 Pa (Pressure, velocity, temperature)

Contours of Static Pressure (pascal)

Sep 23, 2016
ANSYS Fluent Release 16.0 (3d, dp, pbns, rke)

Contours of Velocity Magnitude (m/s)

Sep 23, 2016
ANSYS Fluent Release 16.0 (3d, dp, pbns, rke)

| 312.052 |
| 302.431 |
| 292.810 |
| 283.188 |
| 273.567 |
| 263.946 |
| 254.325 |
| 244.704 |
| 235.083 |
| 225.462 |
| 215.841 |
| 206.220 |
| 196.599 |
| 186.977 |
| 177.356 |
| 167.735 |
| 158.114 |
| 148.493 |
| 138.872 |
| 129.251 |
| 119.630 |

Contours of Static Temperature (k)

Sep 23, 2016
ANSYS Fluent Release 16.0 (3d, dp, pbns, rke)

- Mass flow 29.36 kg/s, 1000 Pa (Pressure, velocity, temperature)

| 2818.546 |
| 1021.448 |
| -775.651 |
| -2572.750 |
| -4369.848 |
| -6166.947 |
| -7964.045 |
| -9761.144 |
| -11558.242 |
| -13355.341 |
| -15152.439 |
| -16949.539 |
| -18746.637 |
| -20543.736 |
| -22340.834 |
| -24137.934 |
| -25935.031 |
| -27732.131 |
| -29529.229 |
| -31326.328 |
| -33123.426 |

Contours of Static Pressure (pascal)

Sep 23, 2016
ANSYS Fluent Release 16.0 (3d, dp, pbns, rke)

Contours of Velocity Magnitude (m/s)

Sep 23, 2016
ANSYS Fluent Release 16.0 (3d, dp, pbns, rke)

Contours of Static Temperature (k)

Sep 23, 2016
ANSYS Fluent Release 16.0 (3d, dp, pbns, rke)

- Mass flow 29.36 kg/s, 1500 Pa (Pressure, velocity, temperature)
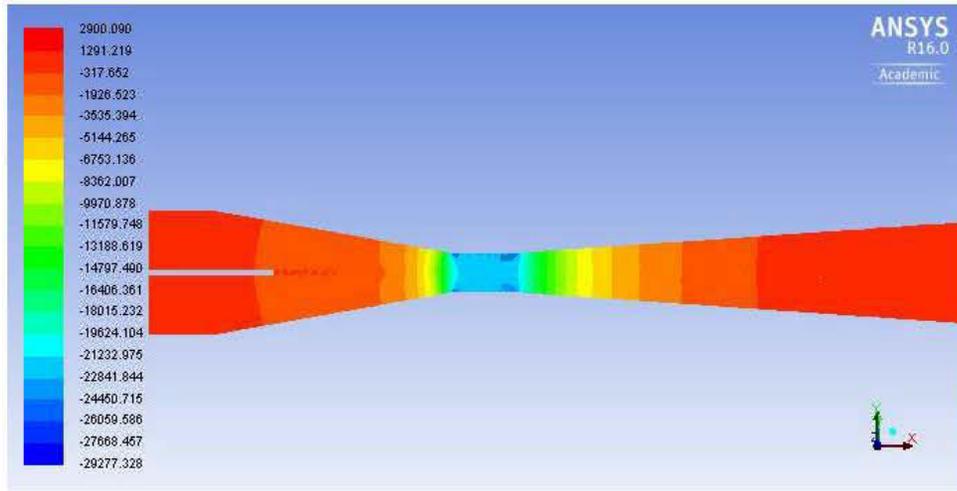
Contours of Static Pressure (pascal)

Sep 23, 2016
ANSYS Fluent Release 16.0 (3d, dp, pbns, rke)

Contours of Velocity Magnitude (m/s)

Sep 23, 2016
ANSYS Fluent Release 16.0 (3d, dp, pbns, rke)
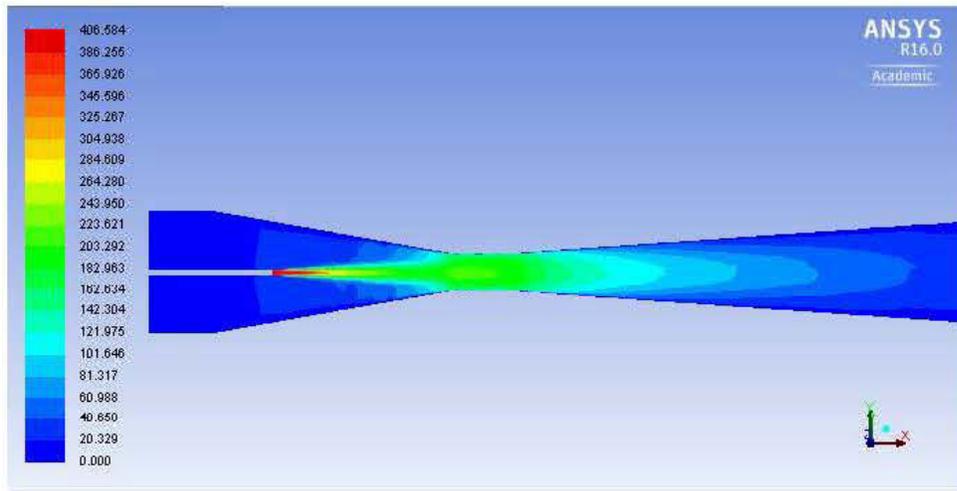
Contours of Static Temperature (k)   Sep 23, 2016
ANSYS Fluent Release 16.0 (3d, dp, pbns, rke)
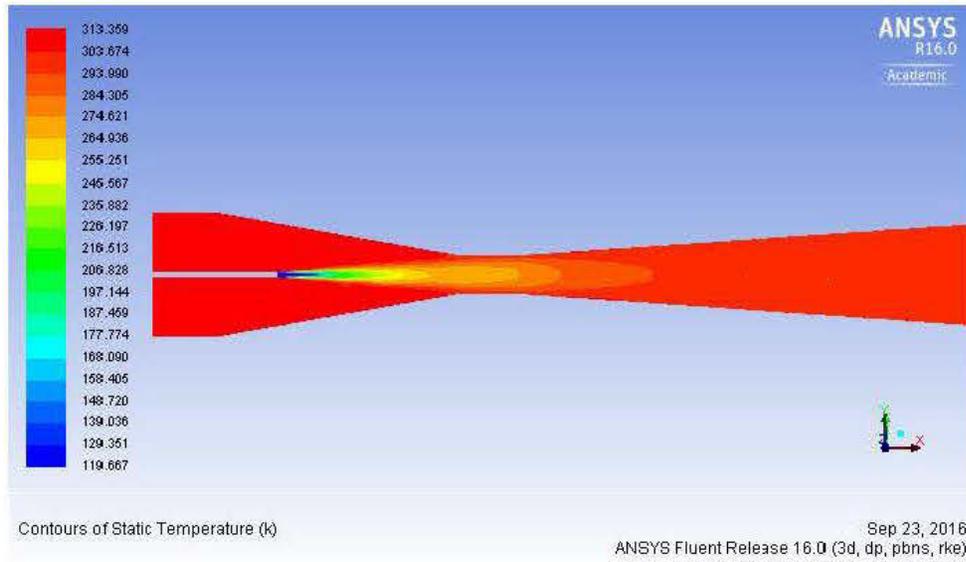
- Mass flow 29.36 kg/s, 2000 Pa (Pressure, velocity, temperature)
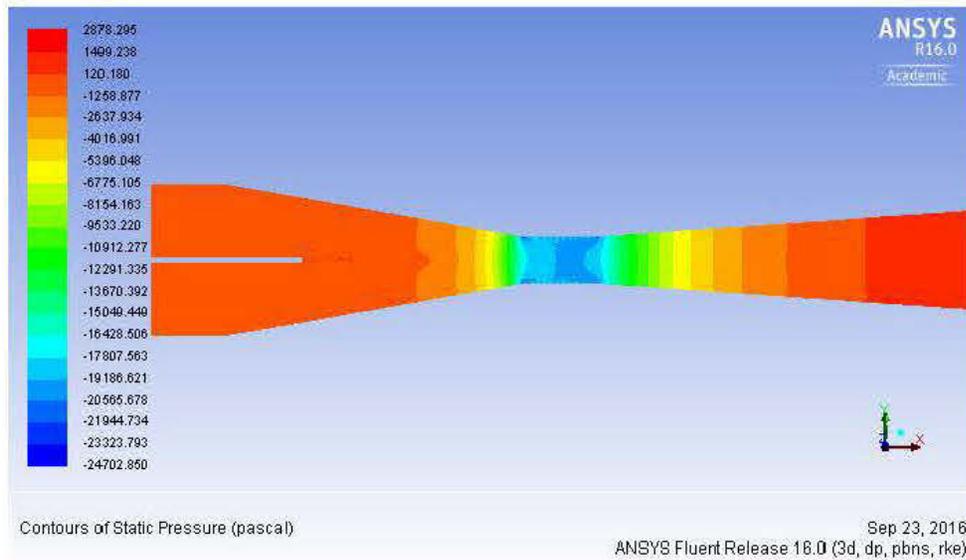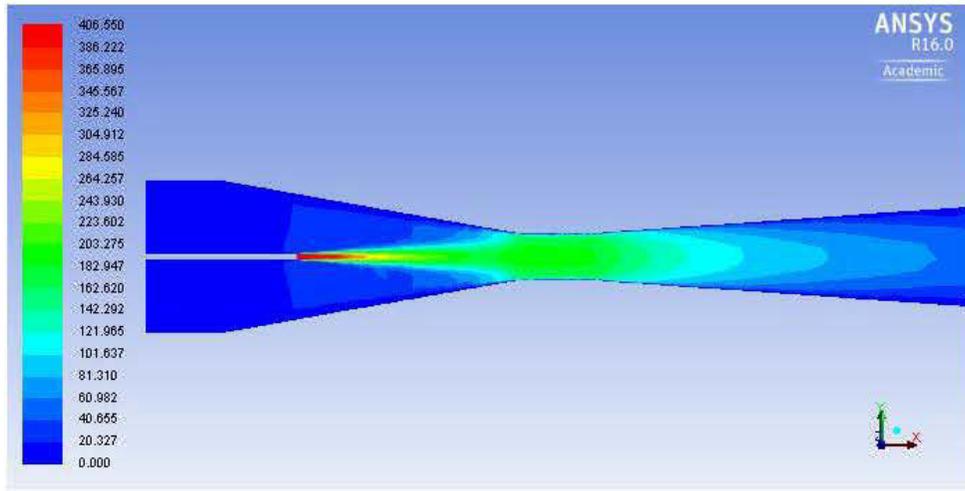
Contours of Static Pressure (pascal)   Sep 23, 2016
ANSYS Fluent Release 16.0 (3d, dp, pbns, rke)

Contours of Velocity Magnitude (m/s)

Sep 23, 2016
ANSYS Fluent Release 16.0 (3d, dp, pbns, rke)
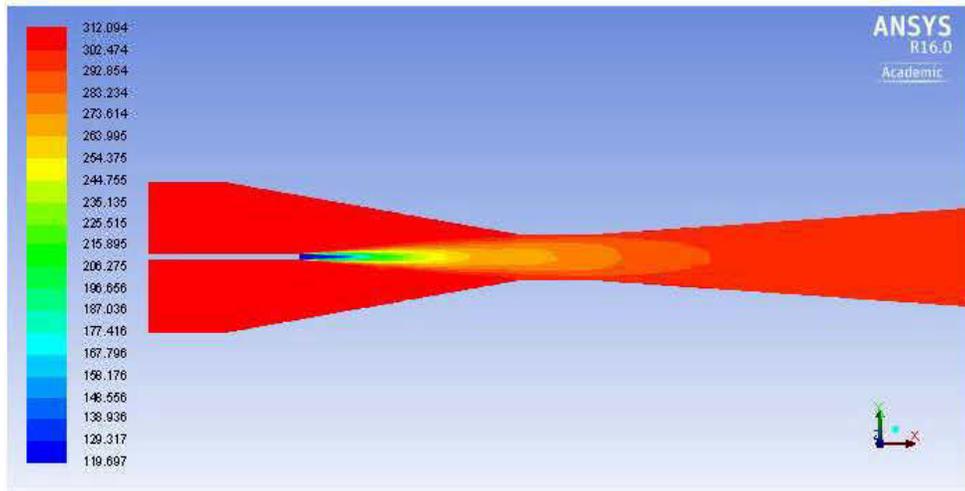
Contours of Static Temperature (k)

Sep 23, 2016
ANSYS Fluent Release 16.0 (3d, dp, pbns, rke)

Appendix C – Nozzle position, Mine scale mode

- Mass flow 22.36 kg/s, 1000 Pa, 6 m nozzle length (Pressure, velocity, temperature)

Contours of Static Pressure (pascal)

Sep 23, 2016
ANSYS Fluent Release 16.0 (3d, dp, pbns, rke)

Contours of Velocity Magnitude (m/s)

Sep 23, 2016
ANSYS Fluent Release 16.0 (3d, dp, pbns, rke)

Contours of Static Temperature (k)

Sep 23, 2016
ANSYS Fluent Release 16.0 (3d, dp, pbns, rke)
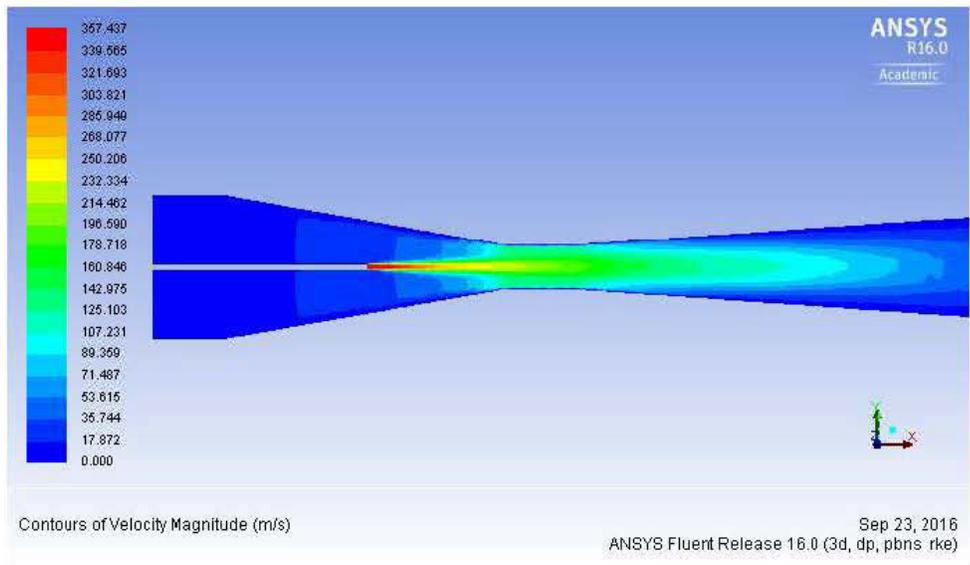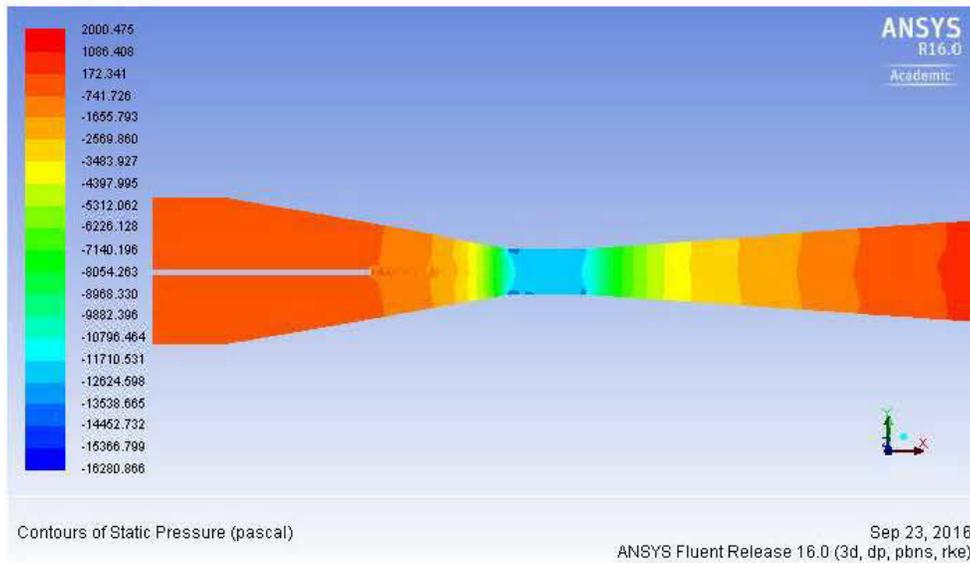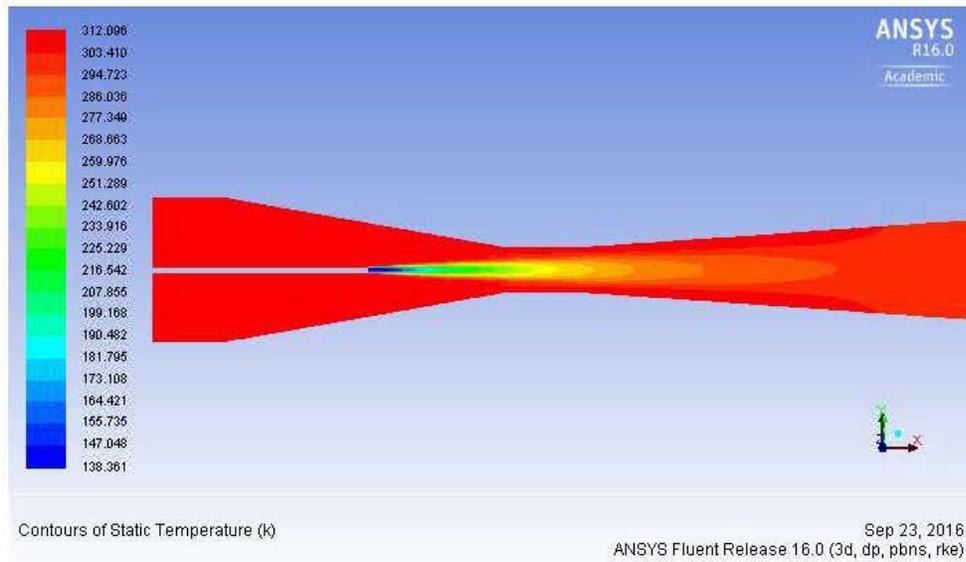
- Mass flow 22.36 kg/s, 1000 Pa, 4 m nozzle length (Pressure, velocity, temperature)

Contours of Static Pressure (pascal)

Sep 23, 2016
ANSYS Fluent Release 16.0 (3d, dp, pbns, rke)

Contours of Velocity Magnitude (m/s)
ANSYS Fluent Release 16.0 (3d, dp, pbns, rke)
Sep 23, 2016

Contours of Static Temperature (k)
ANSYS Fluent Release 16.0 (3d, dp, pbns, rke)
Sep 23, 2016
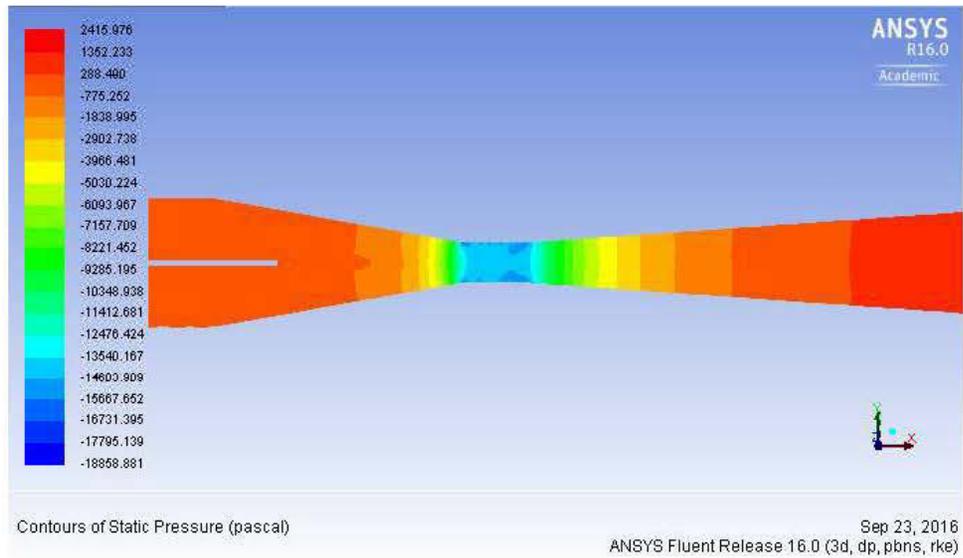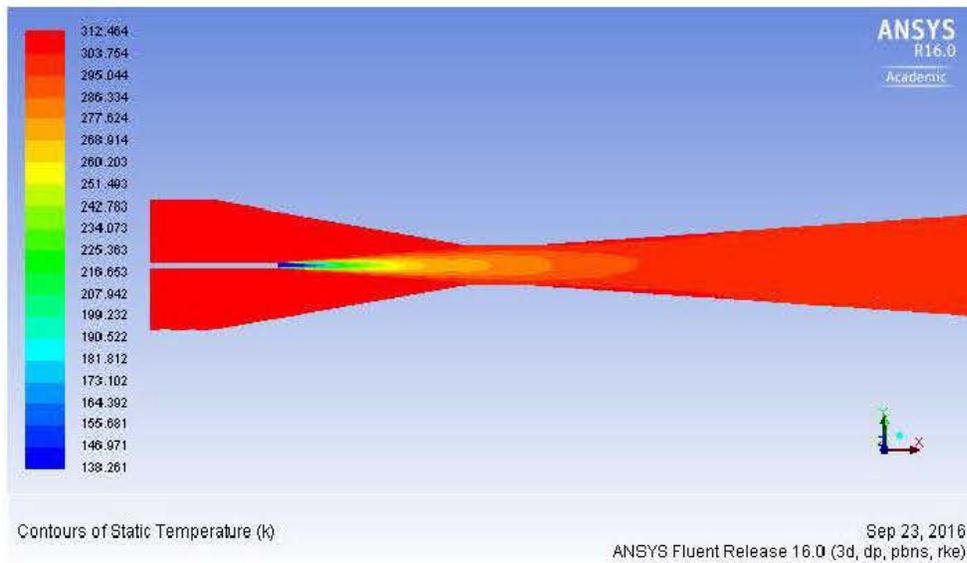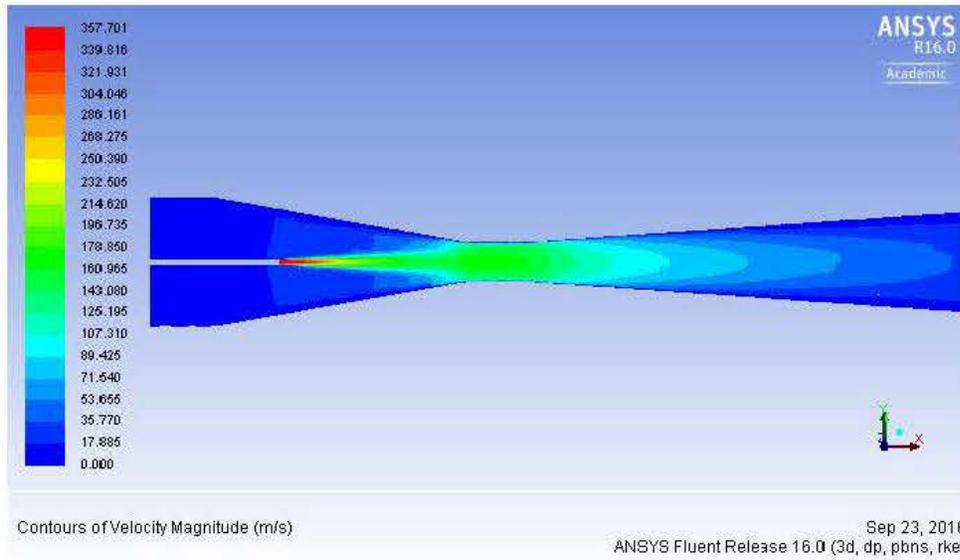
- Mass flow 22.36 kg/s, 1000 Pa, 2 m nozzle length (Pressure, velocity, temperature)
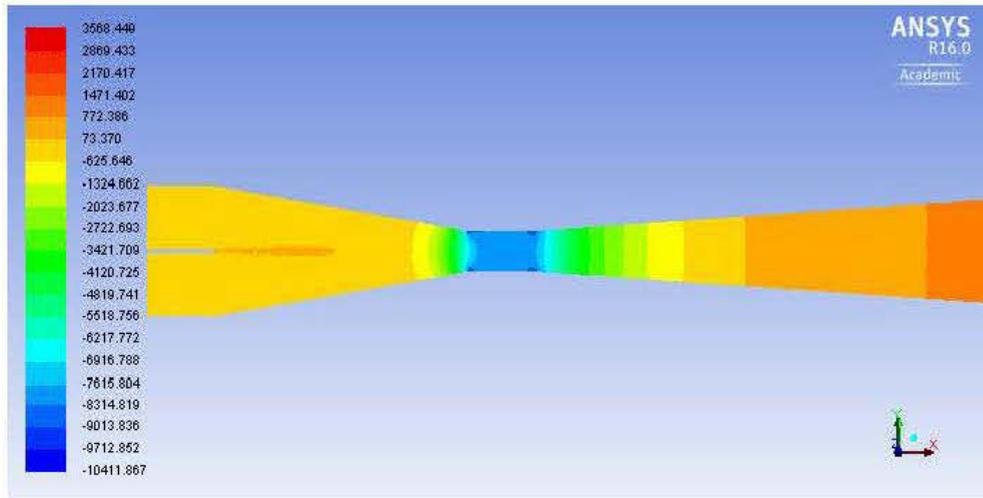
Contours of Static Pressure (pascal)

Sep 23, 2016
ANSYS Fluent Release 16.0 (3d, dp, pbns, rke)

Contours of Velocity Magnitude (m/s)

Sep 23, 2016
ANSYS Fluent Release 16.0 (3d, dp, pbns, rke)

Contours of Static Temperature (k)
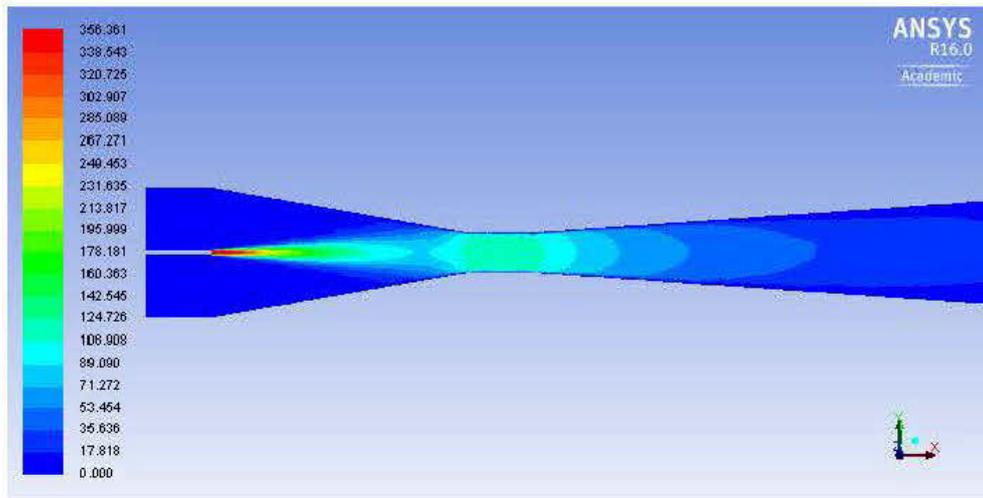
Sep 23, 2016
ANSYS Fluent Release 16.0 (3d, dp, pbns, rke)
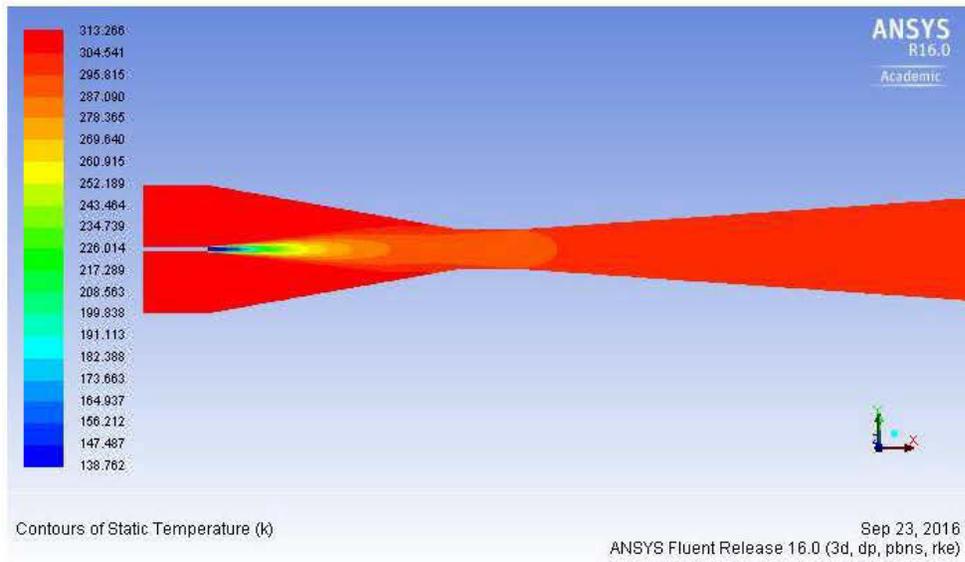
Appendix D – Instrumentation

The instrumentation used in each measuring point is explain in the following section.

- Gauge

It was placed at the exit of the compressor delivery pipe to measure the pressure delivery by the compressor at steady operating point.

- Thermistor TDC 310, 5mm series and Omega Multimeter 881c

The thermistor was placed after the gauge, at the delivery pipe to measure the temperature deliver by the compressor at steady operating point. The omega 881c multimeter was connected to the thermistor by clamps in order to register this temperature with better accuracy. The value showed by the multimeter was applied in a logarithm trendline to obtain the temperature in degree celsius.

- Thermometer Fisherbrand 14-983-10c

It was set at the inlet of the eductor to measure the temperature of the secondary flow. Range: -20 °C to +50 °C

- Micromanometer Model 8702 DP-CALC. ®

It was connected to the inlet and outlet of the ejector to measure the drop pressure. It has the following technical characteristics:
Pressure: -5 to +15 in. H2O (-1245 to 3735 Pa, -9.3 to 28.0 mm Hg)

Accuracy: 1% of reading ± 0.005 in. H2O (±1 Pa, ±0.01 mm Hg)

Resolution: 0.001 in. H2O (1 Pa, 0.01 mm Hg)

- Thermometer Brannon 75mm

It was set at the outlet of the eductor to measure the temperature of the secondary flow. Range: 0 °C to +60 °C

- Micromanometer Model 5825 DP-CALC. ®

It was placed at the restriction point to measure the drop pressure. The technical characteristics are presented here:

Pressure: -15 to +15 in. H2O (-3735 to 3735 Pa, -28 to 28.0 mm Hg)

Accuracy: 1% of reading ± 0.005 in. H2O (±1 Pa, ±0.01 mm Hg)

Resolution: 0.001 in. H2O (0.1 Pa, 0.01 mm Hg)

- VelociCalc® Air Velocity Meter 9535

It was placed at the ventilation rig exit to measure the final velocity. It has the following technical characteristics:

Velocity: 0 to 6000 ft/min (0 to 30 m/s)

Accuracy: ± 3% of reading or ± 3 ft/min (±0.015m/s), whichever is greater.

Resolution: 1 ft/min(0.01 m/s)

- Digiquartz® Pressure Instrumentation 745

It was placed two meters from the ejector to measure the room temperature and pressure. The technical characteristics are presented here:
Pressure: 19 absolute pressure ranges: 0-15 psia (0.1 MPa) to 0-40,000 psia (276 MPa);• 6 gauge pressure ranges: 0-15 psig (0.1 MPa) to 0-200 psig (1.38 MPa)

Accuracy: Better than 0.008% full scale accuracy for all ranges, except 0.08 hPa for barometric range (Model 745-16B) 0.02% full scale for 30,000 and 40,000 psi units

Resolution: Better than 0.0001% full scale

Temperature: 0 °C to +40 °C

- Hygrometer Dwyer 485

It was placed two meters from the ejector to measure the room temperature.

Temperature: -30°C to +85 °C , Accuracy: ±0.5°C , Resolution: 0.1°C

- Thermal camera Flir E50

It was used over the inlet of the delivery pipe to measure and compare the temperature deliver by the compressor at steady operating point with the thermistor.

Temperature: -20°C to +650 °C

Accuracy: ±2°C or ±2% of the reading

Thermal sensitivity: < 0.05°C